Numerical Modelling and Experimental Investigation of Hot Rolled Steels

By

Ke Niu

A thesis submitted in partial fulfillment of the requirements for the degree of

Master of Science

Department of Mechanical Engineering

University of Alberta

ABSTRACT

Hot rolled steels are steel alloys manufactured through a very efficient direct rolling process following solidification above the recrystallization temperature. Hot rolled steels have a unique microstructure with relatively high contents of bainite and martensite phases continuously dispersed in a ferrite matrix. Hot rolled steels exhibit superior strength and moderate ductility. They are considered as a group of advanced high strength steels with very promising potential application in the automotive industry. Interest of these materials has seen a great increase in recent years.

In the present work, deformation behaviors of hot-rolled, stretch flangeable steels have been investigated. Tensile tests of circularly notched steel samples of different notch geometries are conducted to mimic the deformation condition during stretch flanging. A digital image correlation system is employed to record local strain distribution during the tensile test, while finite element simulations of notched tensile tests are performed to examine the stress state variation within the notched region. The stress-strain relations are derived from load-displacement history of tensile tests and digital image correlation analysis. Multi-particle unit cell models were built to simulate the effect of the distribution of bainite/martensite phases on the deformation behavior of hot rolled steels. The actual stress states experienced within the notched region were extracted from the finite element results and applied directly to the micromechanical models.

PREFACE

Some of the research conducted for this thesis forms part of a research collaboration, led by Professor Keith Pilkey at the Queen's University, with Professor Zengtao Chen being the lead collaborator at the University of Alberta, and Professor Michael Worswick being the lead collaborator at the University of Waterloo. The material properties used for finite element simulation in Chapter 2 were provided by the research group at the University of Waterloo. All others are my original work.

Chapter 5, section 5.1 and 5.2 of this thesis has been published as K. Niu, A. Abedini, and Z.T. Chen, "The Influence of Multiple Inclusion on the Cauchy Stress of a Spherical Particle-reinforced Composite under Uniaxial Loading," ASME 2014 International Mechanical Engineering Congress & Exposition (IMECE), Montreal, Canada. I was responsible for building the finite element models, data collection and analysis. A. Abedini was responsible for the analytical model. Z.T. Chen was the supervisory author.

DEDICATION

To my parents, Hongwei Niu and Xuehua Zhang for their love and supports

ACKNOWLEDGEMENTS

I would like to express my deep gratitude to my supervisor, Dr. Zengtao Chen, for his patient guidance, enthusiastic encouragement and invaluable support during every aspect of my MSc study.

I would also like to thank the members of the thesis committee, and my peer graduate students and postdoctoral fellows with whom I enjoyed sharing and discussing the research. They are Dr. Hamid Akbarzadeh, Armin Abedini, Jiawei Fu, Yi Cui, and Dr. Keqiang Hu. Their help and intelligence enlightened many blind spots in my research.

I would also like to extend my thanks to Vince Boardman, Salvator Keith Poirier and Nicolas Losier, Mechanical Engineering Department of the University of New Brunswick, for their assistance in conducting uniaxial tensile experiments and microstructure analysis.

Finally, I gratefully acknowledge the financial support provided by the AUTO21 Network of Centers of Excellence.

Table of Contents

List of Tables

List of figures

Nomenclature

σ_{hyd} = Hydrostatic Stress

σ_{eq} = von Mises Equivalent Stress

σ_y = Yield Stress

S_{ij} = Stress Components

SiC = Silicon Carbide

Al_2O_3 = Alumina

PMCs = Polymer Matrix Composites

RSA = Random Sequentially Adsorption Algorithm

AHSS = Advanced High Strength Steels

HSLA = High Strength Low Alloy Steel

DP = Dual Phase

CP = Complex Phase

TRIP = Transformation-induced Plasticity

HR = Hot Rolled

HRSF = Hot Rolled Stretch Flangeable

HHE = High Hole Expansion

HR780SF = Hot Rolled Stretch Flangeable steel with tensile strength of 780 MPa

R2 = Notch radius is 2 mm

R4 = Notch radius is 4 mm

R6 = Notch radius is 6 mm

R8 = Notch radius is 8 mm

DIC = Digital Image Correlation

UTS = Ultimate Tensile Strength

FEM = Finite Element Method

T = Stress Triaxiality

SEM = Scan Electron Microscope

1. Hot-Rolled Stretch Flanging Steel

1.1. Introduction

Nowadays, safety, fuel efficiency and performance become more and more important in the automotive industry. New steels are required to be developed in order to meet the requirements of weight reduction, improved passive safety features, energy saving considerations and environmental protection [1-4]. As a result, the interests in advanced high strength steels (AHSS) have been rekindled since they have many attractive properties, such as extremely high strength, high strain-hardening capacity, enhanced formability and low costs. These advanced properties make AHSS a good candidate to fulfill these requirements in automotive industry. Advanced high strength steels (AHSS) have been around for many years, with additional research and development, newer generation of AHSS has been developed and been used in more applications. Hot Rolled steels are a group of AHSS manufactured in a cost-coefficient way which show a promising application in the automotive industry in recent years.

There are many types of AHSS including dual phase steels (DP), transformation-induced plasticity steels (TRIP), complex phase steels (CP), and hot rolled stretch flangeable steels (HRSF). The microstructure of dual phase steel usually consists of two phases which are ferrite and martensite. TRIP steels have a relative complex microstructure which includesferrite, martensite, bainite and some retained austensite. They are all ferrite based AHSS [2].

1.2. Hot Rolled Stretch Flanging Steel (HRSF)

Hot-Rolled Stretch Flanging steels (HRSF) steels are pickled as their last production step without cold rolling, continuous annealing or galvanizing. These steels are manufactured through hot rolling process following solidification above the recrystallization temperature. Unlike DP steels, HRSF is typically a multi-phase steel. The microstructure usually consists of ferrite, bainite and some retained austenite. It results in a soft ferrite matrix embedded with hard bainite particles/fibers and a small amount of austenite. The strength of HRSF steels increases with increasing volume fraction of bainite [5, 6]. HRSF usually have a lower amount of carbon content of 0.05% [2, 7]. A lot of research was done on the stretch flange forming of alloys. For example, both experimental and numerical FE modelling investigations were done on the strain development of stretch flange forming of aluminum alloys by Chen [8]. Chen also investigated the stretch forming of aluminum-magnesium alloys by using experiments and damage-based FE modelling [9]. This bainitic - ferrite microstructure exhibited superior formability during sheared edge stretching than commercial dual phase steels [7]. Usually, the stretch-flangeability was described by using representative volume elements and continuum damage model in the hole expansion process [1, 10].

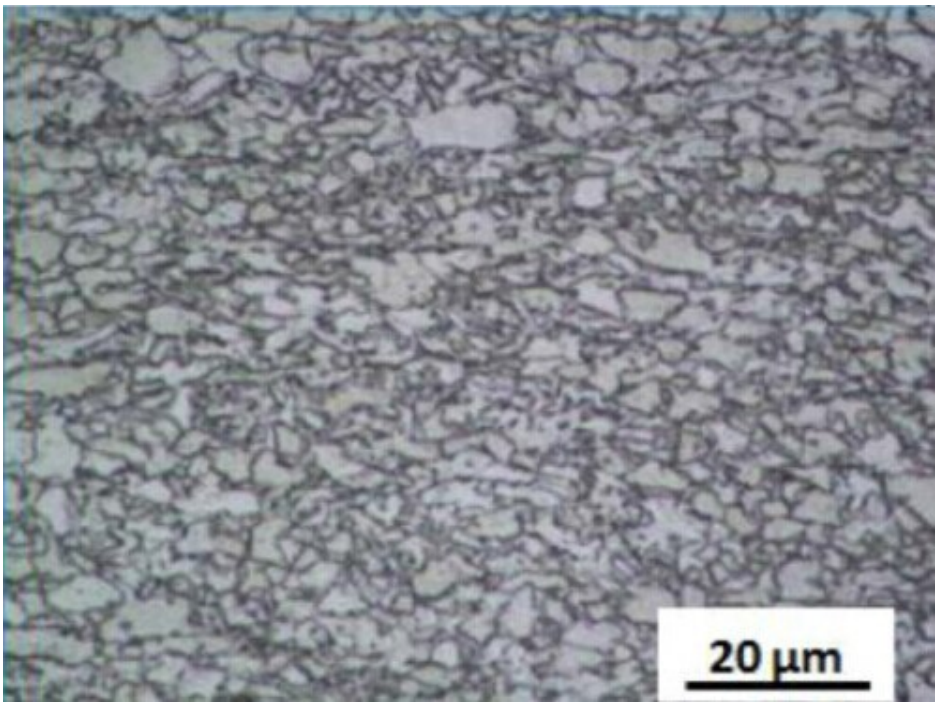

Fig. 1.1: Microstructure of HRSF [7]

The development of complex microstructures can enhance material performances of steels, such as high strength, high strain-hardening and high formability, etc. For these multi-phase steels, it was found that volume fraction and distribution of different phases significantly affect their deformation behaviors [6, 11, 12]. The effects of volume fractions of particles on stress-strain relations were also investigated by using unit cell approaches in chapter 5 of this thesis. Recently, the investigations of rolling temperature indicate that it affects mechanical properties by altering the characteristics of grain refinement and precipitation [13]. Also, the precipitation of nitrides of HR low carbon Al-killed steel was found significantly affected by its grain size [14]. A lot of research indicates that microstructure plays a crucial role on mechanical properties [15-19].

1.3. Manufacturing and Application

The normal process of manufacturing hot rolled steel is shown in Fig. 1.2. Four prototypes of Hot-Rolled Stretch Flanging grade steels with tensile strength of 780MPa (HR780SF) which were developed by ArcelorMittal Dofasco [20] were selected for the investigation in this chapter. These steels were produced with the same chemical compositions but different heat treatments, and they are numbered as A80273, A80274, A80283 and A80284. Fig. 1.3 shows the thermal path for four prototypes of HRSF steels between rolling / finishing and coiling. In order to manufacture hot rolled steels with specific or designated properties, heat treatments are crucial, and temperatures need to be precisely controlled. Nowadays, the thinnest gauge for hot rolling process is 2.5 mm. One automotive application for hot rolled stretch flangeable steels is control arms.

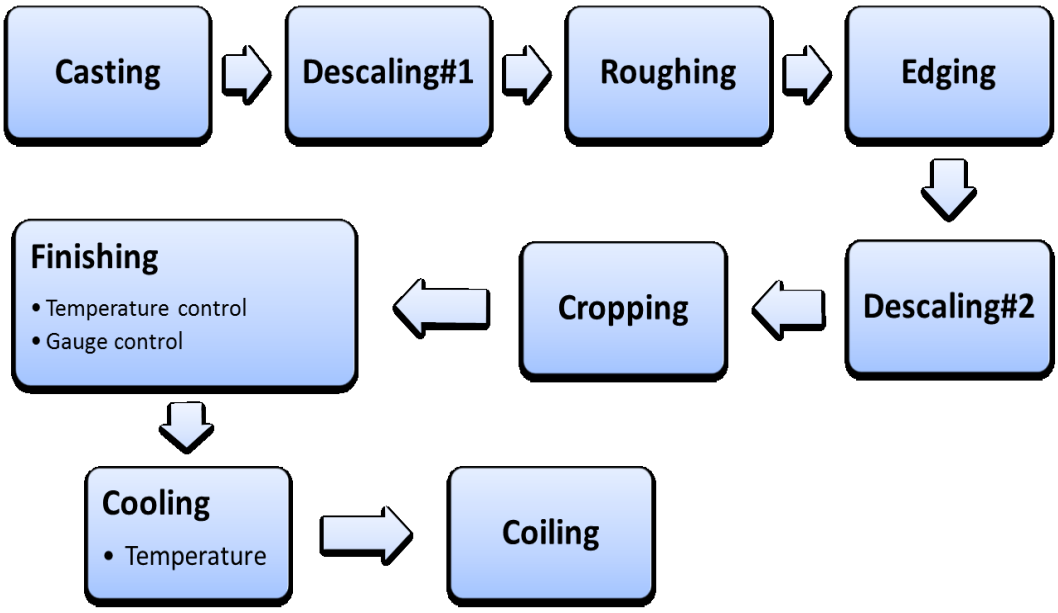

Fig. 1.2: Flowchart of manufacturing process of hot-rolled steel

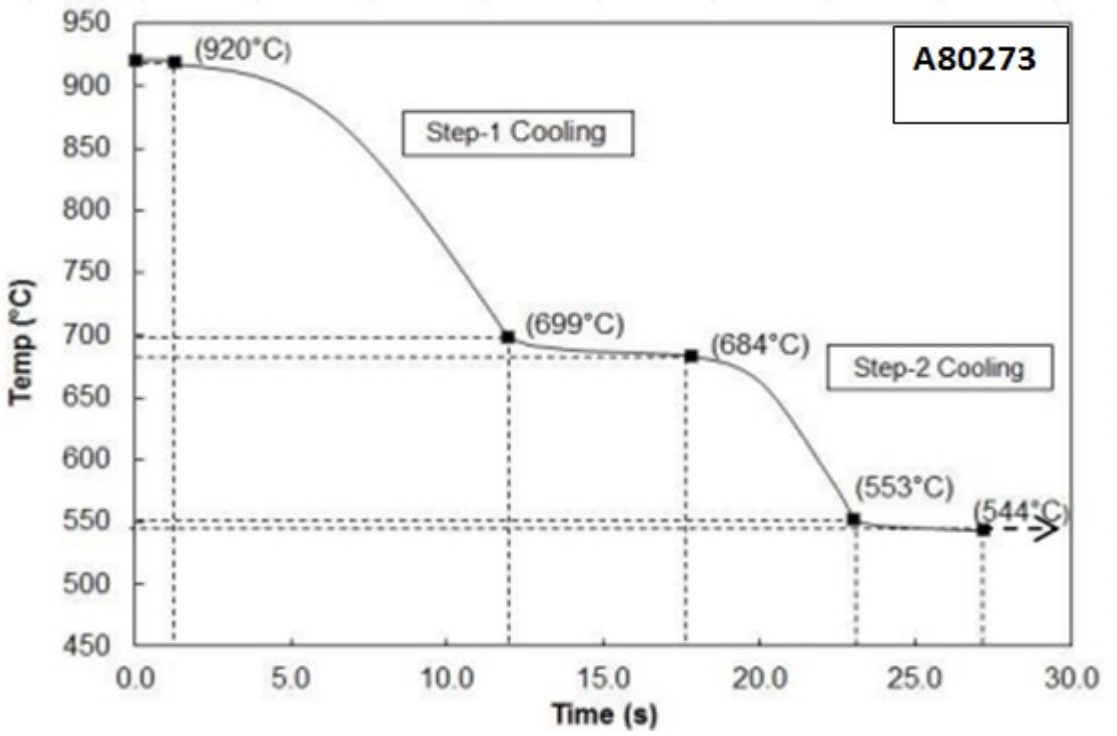

(a) A80273

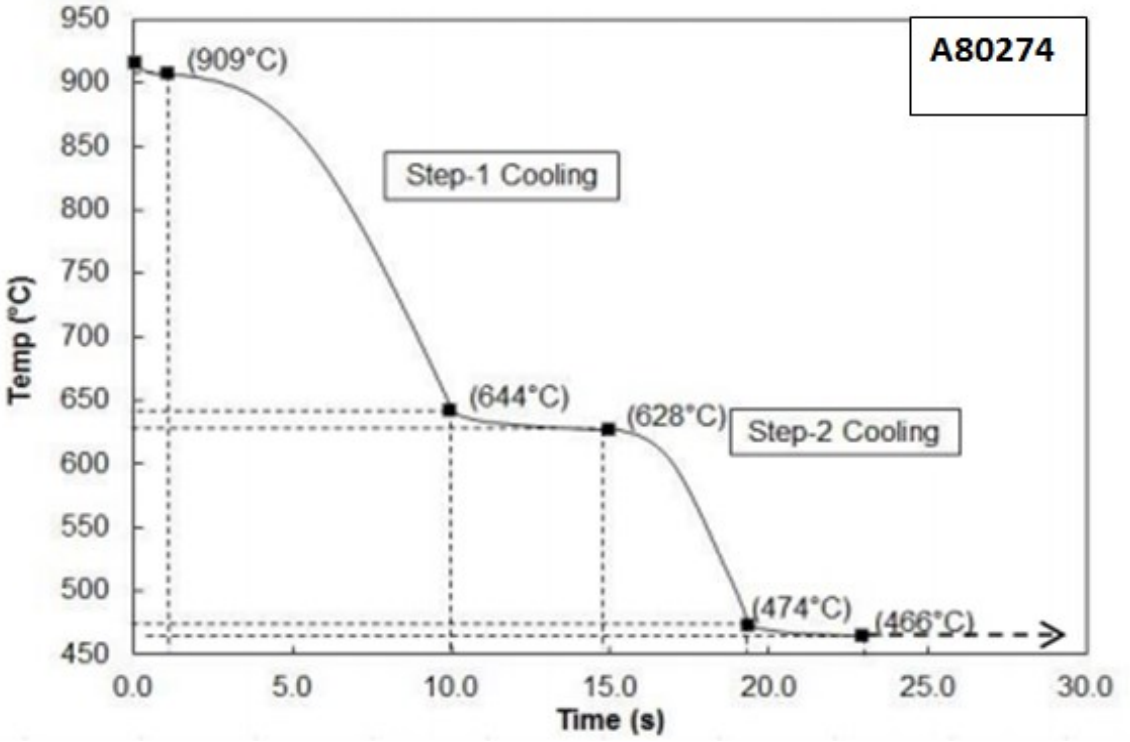

(b) A80274

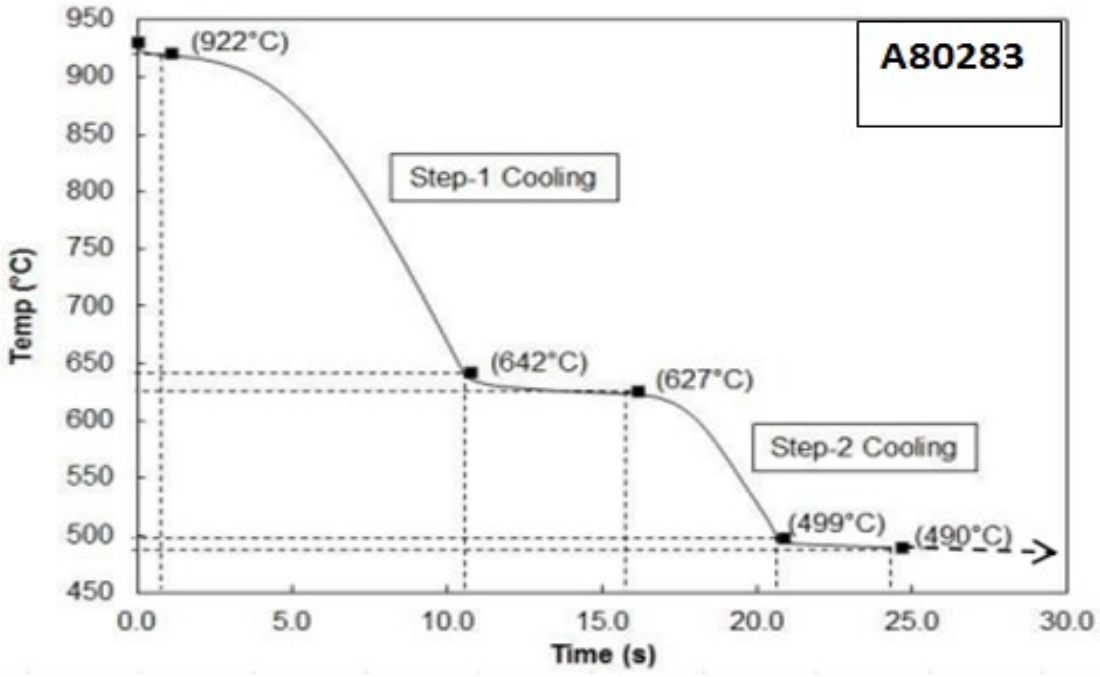

(c) A80283

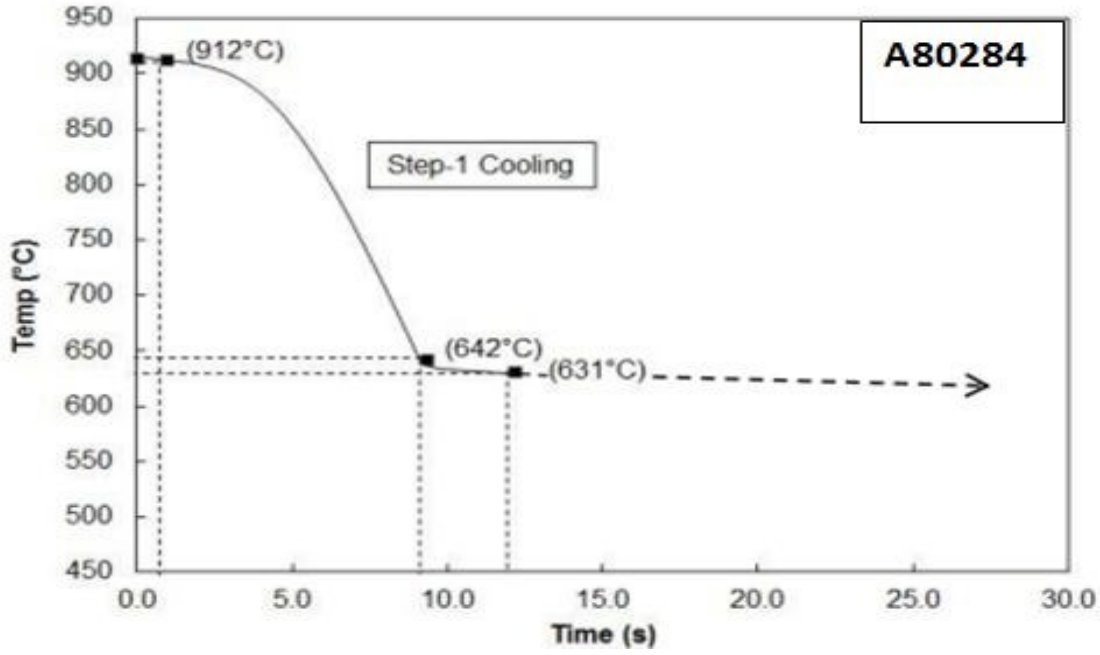

(d) A80284

Fig. 1.3: Cooling schematics showing thermal path between rolling and coiling [21]

2. Experimental Investigation of Hot Rolled Steels

2.1. Uniaxial Tensile Test

Sheet steel samples with circular notches were designed and manufactured to induce different stress states in the material. Originally, the hole expansion experiments were used to test the stretch flangeability of HR steel. Since no facilities were available to test the stretch flangeability of materials, tensile tests of circular notched samples were conducted to mimic the deformation condition of flangeable steels during stretch flanging. Circular notches of various radii were prepared in the rolling direction of the sheet samples, while the ligament size was kept constant at 4 mm. The designed geometry and dimensions of sheet steel samples with circular notches are shown in Fig. 2.1. Uniaxial tensile loading was applied to sheet steel samples with notch radii of 2 mm, 4 mm, 6 mm and 8 mm. The effects of notch geometry on stress triaxiality and stress-strain relations were investigated.

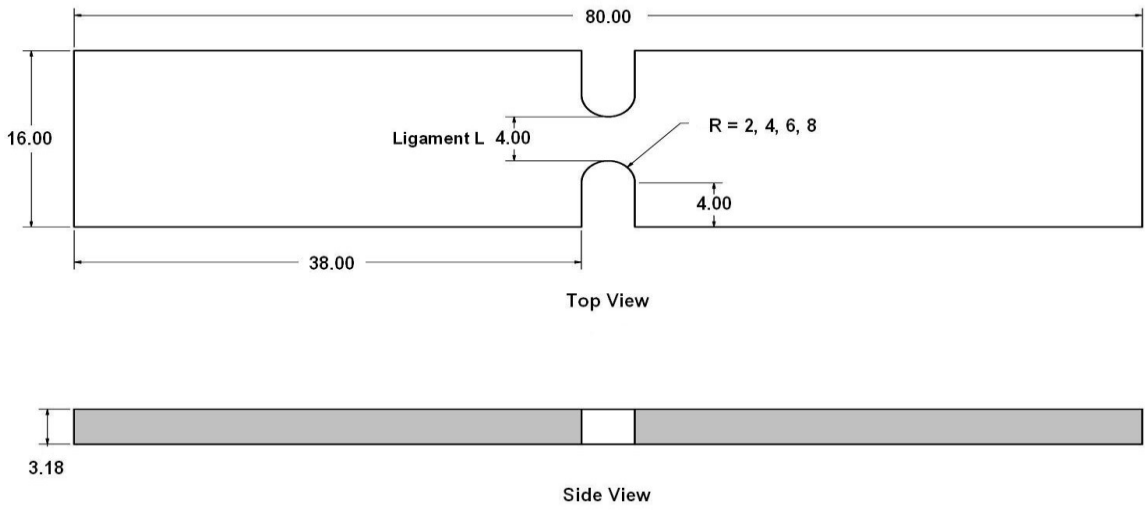

Fig. 2.1: Geometry of circular-notched sheet specimen

2.2. Digital Image Correlation Analysis (DIC)

Digital image correlation (DIC) is an optical, non-contact technique which uses a mathematical correlation analysis to examine the digital images taken in mechanical tests, such as tensile tests. Since no special paint pattern is required and no contact with the specimen, this correlation tool has a large freedom and broad area of applications [22]. It can provide us a full-field measurement of displacement and strain. Because of the development of sophisticated digital cameras and image processing software, the new non-contact DIC measurement technology came into our eyes.

The DIC system typically consists of a high resolution digital camera and a computer with *MATLAB* program. A series of high resolution images of deformed samples are captured during the experiment, e.g. tensile test. The change in surface characteristics is evaluated by examining consecutive images [23-27]. The *MATLAB* codes which were developed at Johns Hopkins University by Eberl et al. [28] were used to analyze these high resolution images. A numerical cross-correlation algorithm, which is built into the *MATLAB* image processing toolbox [29] is used to perform comparison of greyscale values of these high resolution images. The ability to provide a full-field measurement of strain and displacement is the main advantage of DIC technology. Compared to the traditional tensile test where only one strain is provided by the extensometer between two specific points, the DIC technique can provide a local strain distribution for any specific area of interest.

The DIC technique was used to capture the deformation of hot-rolled sheet steel samples during uniaxial tensile tests. Some preparations needed to be done before performing the DIC technique. Firstly, the notched samples needed to be polished by a sand paper; secondly, the samples were cleaned subsequently with water and alcohol; finally, the samples were first sprayed with white background to increase the contrast; then they were sprayed with black speckles. It was noticed that it was better to let the droplets fall onto the surface of samples instead of spraying directly onto the surface of samples. A group of prepared samples are shown in Fig. 2.2. The *INSTRON 1332* servo-hydraulic universal testing machine and the *Nikon D300s* digital camera were used in the experiment. This experiment was performed at room temperature with a humidity of 50%. The tensile testing machine was set to be position controlled with a low ramp speed to minimize the effects of displacements rate on material behavior. The displacement rate was set to be 0.5 mm/min. Since most of the changes in strain occur in the middle of the notch area, the notch area is the location of interest. In order to obtain high quality images, two *PL-253202/#60503* lights were used to supply enough illumination. Fig. 2.3 shows the completed setup of the experiment. The images of the testing sample during the deformation were captured every 6s until experiments completed.

After tensile tests were completed, all images were post-processed by the *MATLAB* program. As shown in Fig. 2.4, grids are generated for the cross-correlation algorithm to analyze the movements of each pixel and its associated grey-scale intensity. The interested locations of steels samples during DIC analysis are shown in Fig. 2.5. Fig. 2.6 shows the sheet samples after tensile tests.

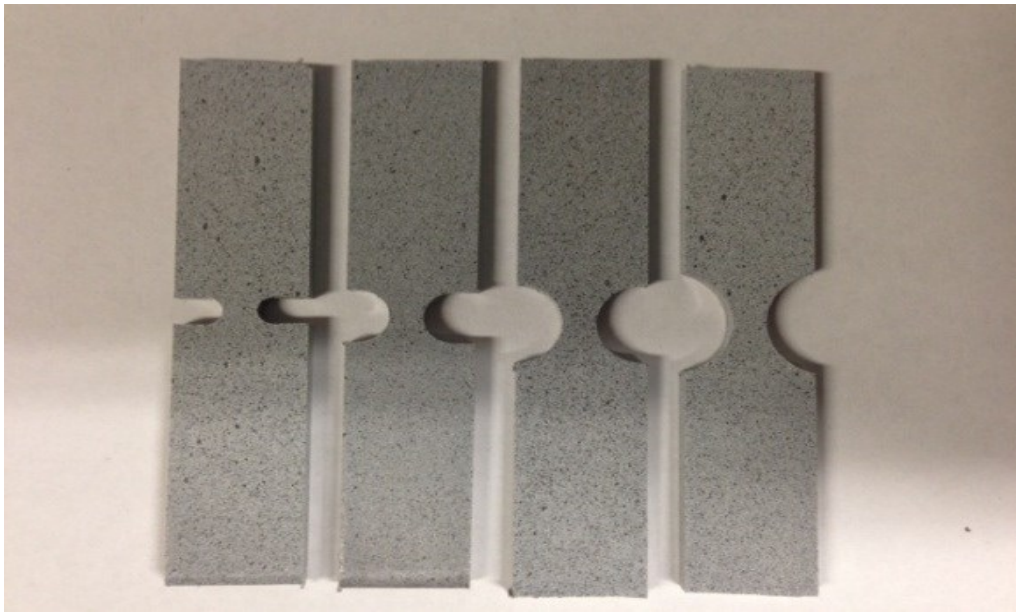

Fig. 2.2: Painted steel samples with different sizes of notches

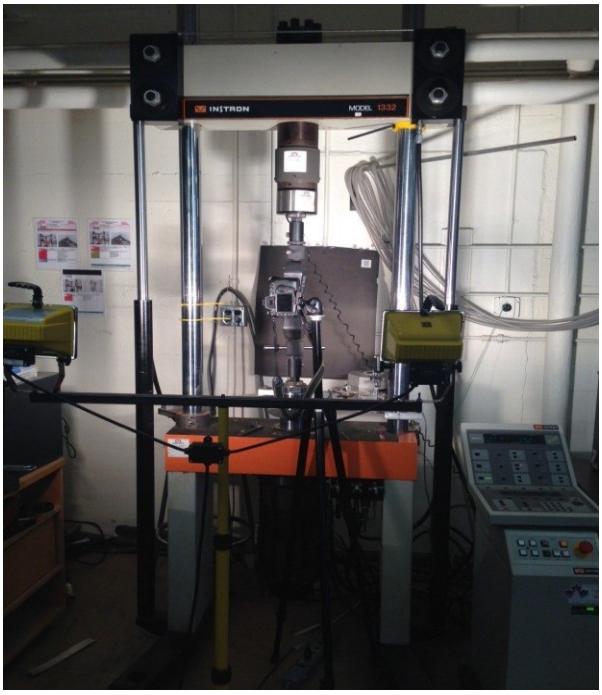

Fig. 2.3: INSTRON 1332 servo-hydraulic universal testing machine and Nikon D300s digital camera

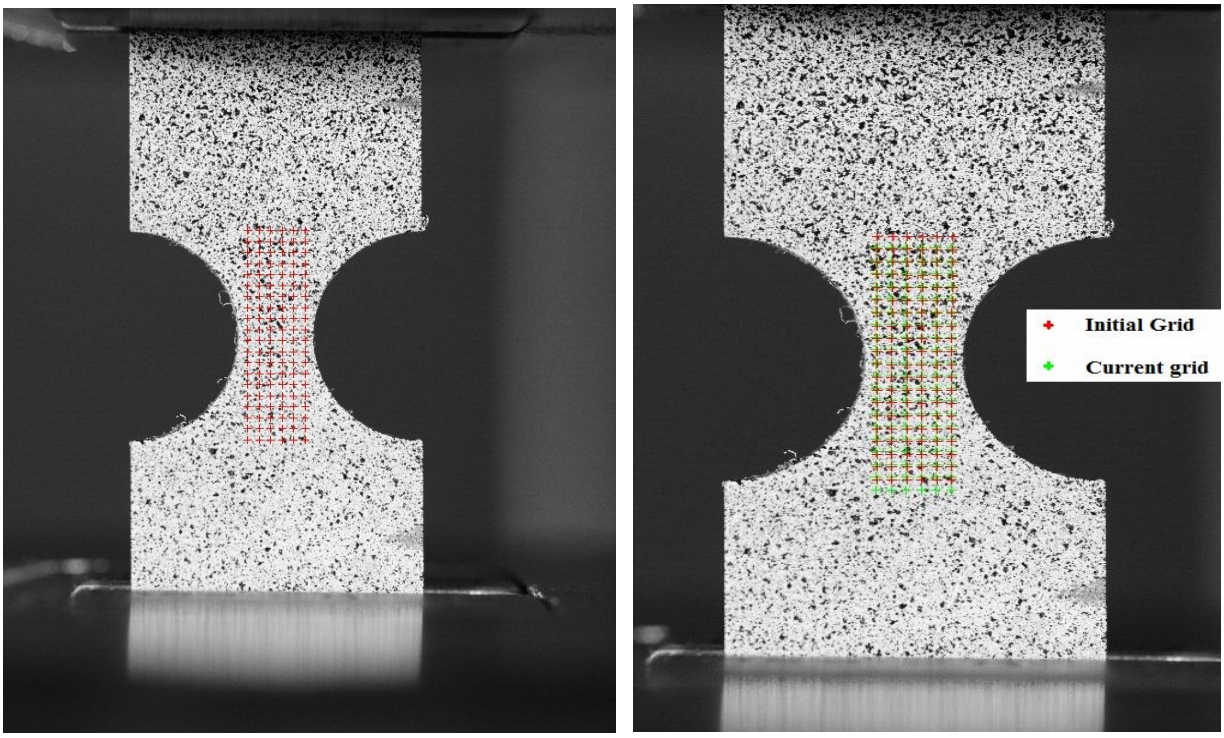

Fig. 2.4: Digital image correlation process (grid)

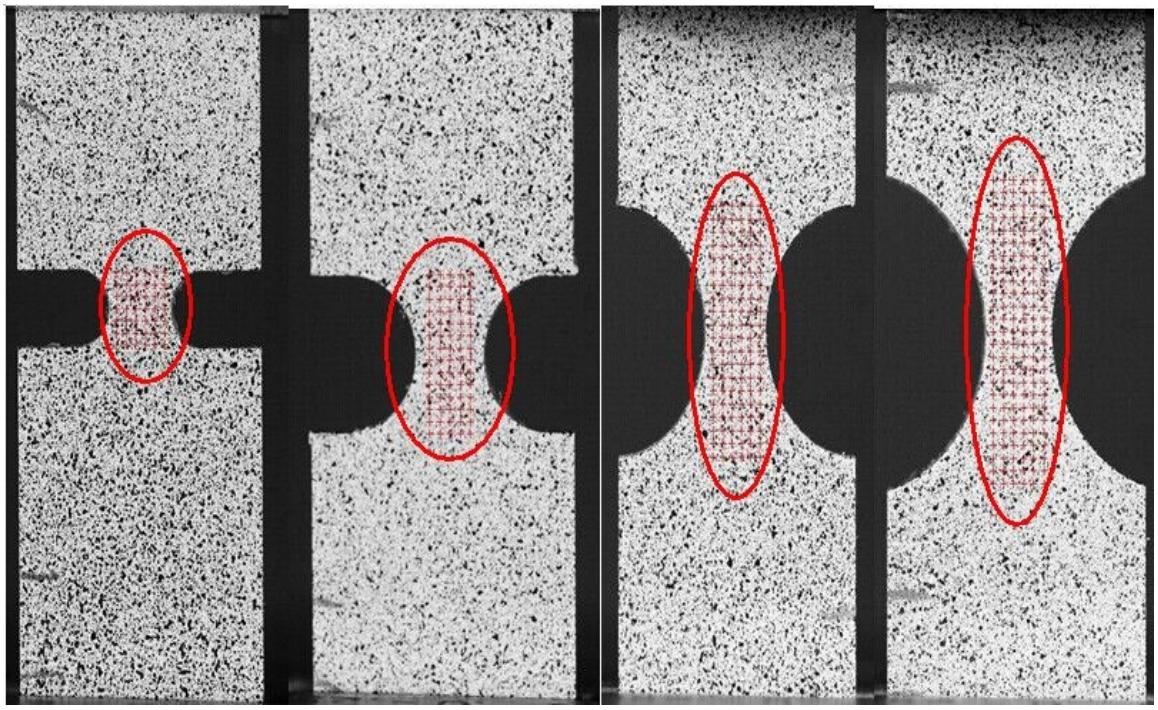

Fig. 2.5: Interested locations of HRSF steel samples

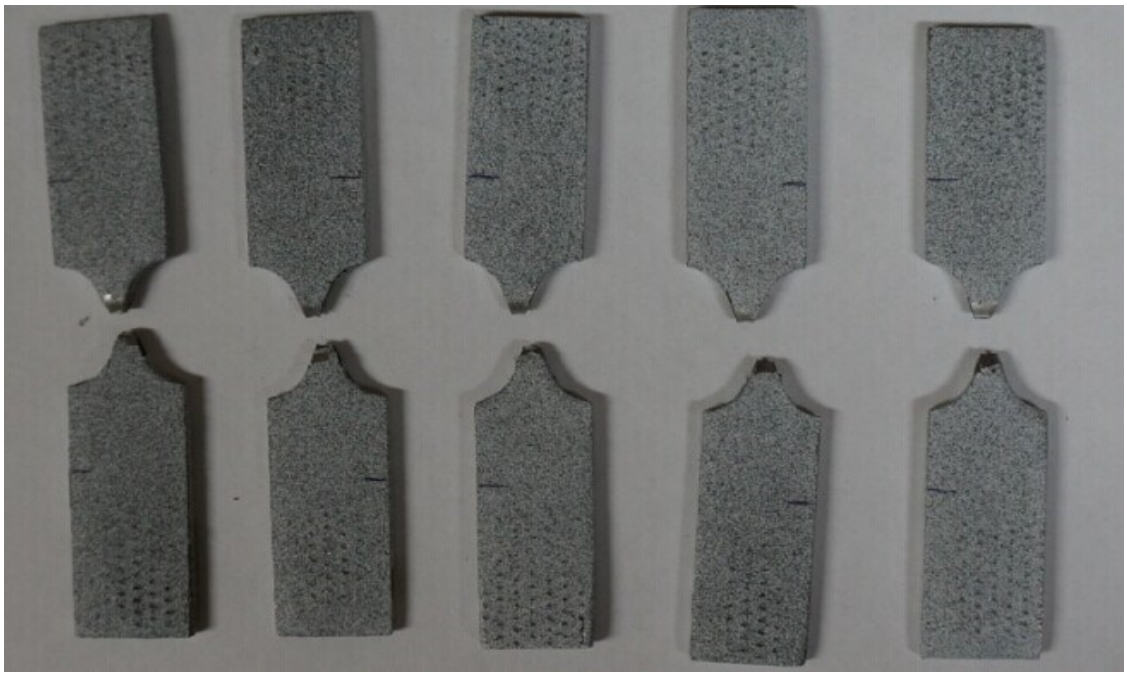

Fig. 2.6: Sheet steel samples after tensile tests

2.3. Results and Discussion

The experimental data of tensile tests were recorded by and exported from the *INSTRON* 1332 servo-hydraulic universal testing machine. For each prototype of HR steels, an average number of four samples were tested. Two data points of displacement and load were captured per second. Averaged experimental data of the maximum load are shown in Table 2.1. A histogram is shown in Fig. 2.7 to provide a visual comparison of material behavior of sheet steel samples. Fig. 2.7 clearly shows that A80274 steel samples exhibit the strongest response while A80283 steel samples exhibit the softest response. The only exception is that a large increase in stress behavior is observed for A80283 steel samples with the largest notches (8 mm in notch radius). All values shown in Fig. 2.7 are averaged results of four samples.

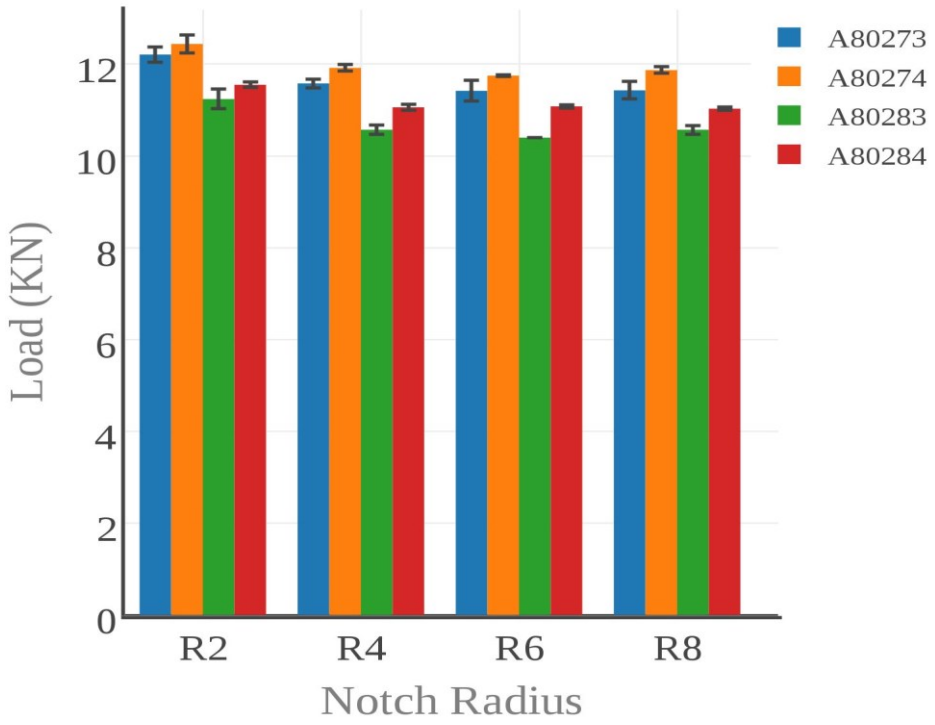

Fig. 2.7: Maximum load versus notch radius for different sheet steel samples

Table 2.1: Averaged experimental results of sheet steel samples

Steel	Notch radius (mm)	Maximum Displacement (mm)	Maximum Load (KN)	Time (s)
A80273	2	2.97	12.21	367
	4	3.08	11.58	364
	6	3.24	11.42	386
	8	3.3	11.43	389
A80274	2	2.84	12.44	340.3
	4	3.05	11.92	376.6

	6	3.19	11.75	384.6
	8	3.23	11.87	387.6
A80283	2	2.57	11.24	305.6
	4	2.65	10.57	316.6
	6	2.77	10.4	332.3
	8	2.86	10.57	336.8
A80284	2	2.63	11.55	313.3
	4	2.71	11.06	318.1
	6	2.85	11.08	333.8
	8	3.03	11.03	362.3

The comparison of stress-strain relations for each grade HR steels of different notch radii are shown in Fig. 2.8. The results of engineering stress were derived by using the recorded loads (from Instron machine) divided by the cross-sectional area of the ligament. And then, the results of true stress were converted from corresponding engineering stresses. The results of true strain were derived by analyzing high resolution images with DIC technology within the interested areas as shown in Fig. 2.5. After that, the engineering strain can be obtained from the true strain. The location of interest for DIC strain measurement is the notch area. Approximately 60 data points of true strain were from DIC method, while about 700 data points were obtained from tensile test for each sheet steel sample. Therefore, for data point of true strain, corresponding true stress were found and plotted in Fig. 2.8.

As shown in Fig. 2.8, for each grade steel (A80273, A80274, A80283, and A80284), sheet steel sample with the smallest notch (R2) exhibits the strongest response, while sample with the largest notch (R8) exhibits the softest response. Moreover, sheet steel samples with the smallest notch exhibit the largest change in strain. This change in strain decreases with increasing notch size. In other words, it takes more time for samples that have the smallest notch reach the fracture point. However, in the case of samples that have the largest notch, the fracture occurs in a short time after they reach the ultimate tensile strength (UTS). For example, it can be observed that fracture occurs at true strain of 0.15 for A80273 R2, while fracture occurs at true strain of 0.03 for A80273 R8 in Fig. 2.8 (a). Similar behavior can be observed for other groups of sheet steel samples (A80274, A80283, and A80284) in Fig. 2.9 (b), (c) and (d). The maximum true stresses for A80273, A80274, A80283 and A80284 were found to be 981.8 MPa, 1005 MPa, 887.9 MPa, and 917.9 MPa, respectively. Sheet steel sample A80274 R2 exhibits the largest true stress while sheet sample A80283 R2 exhibits the smallest true stress.

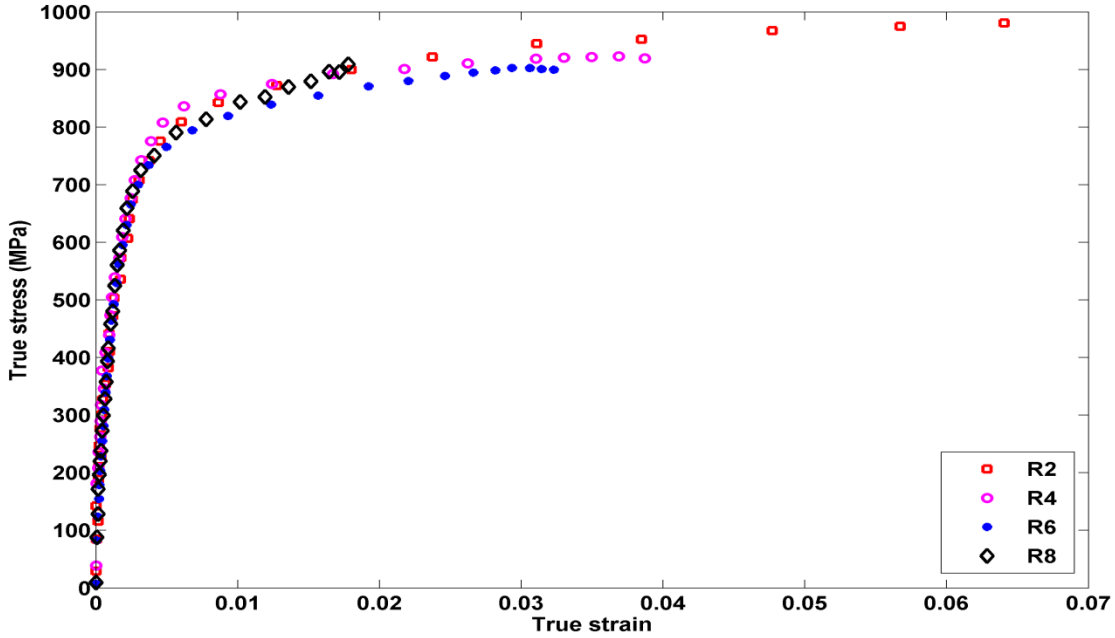

(a) A80273

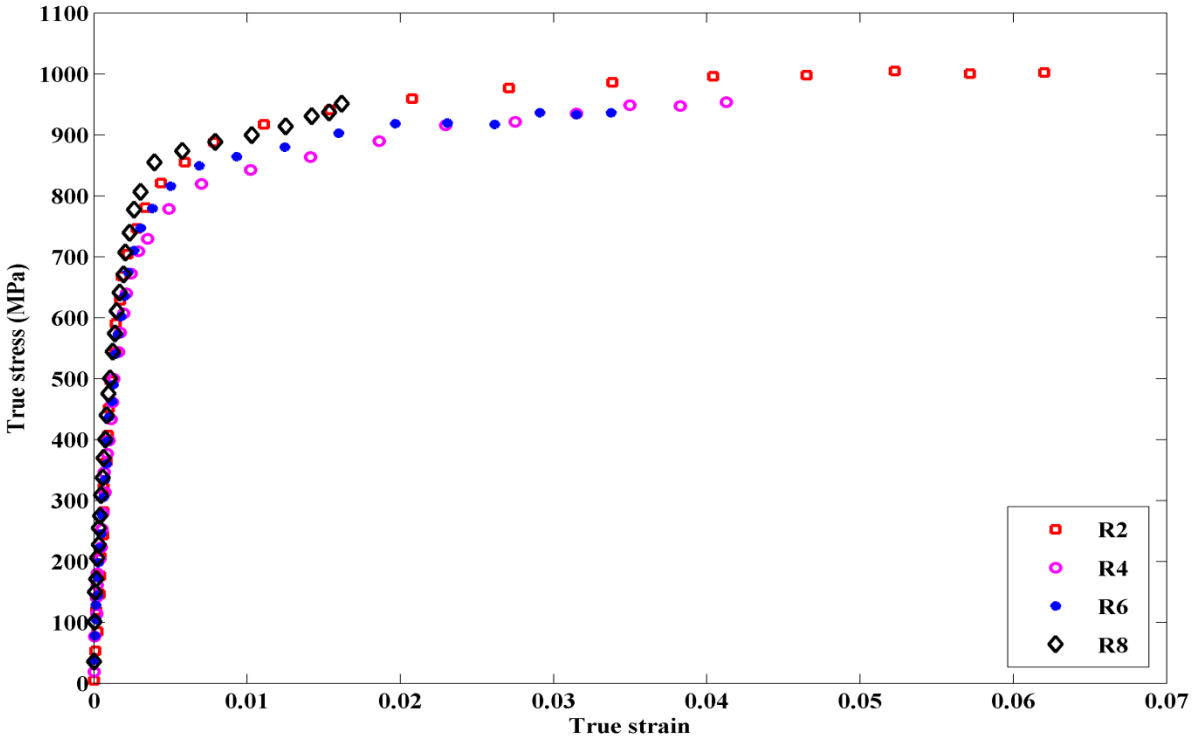

(b) A80274

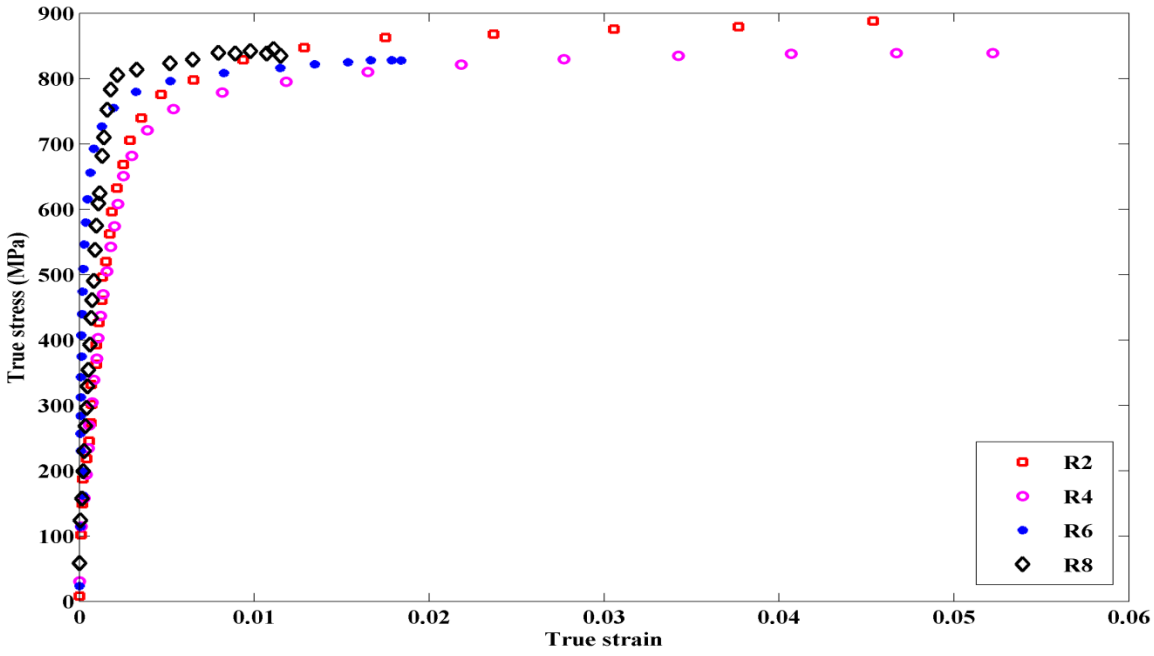

(c) A80283

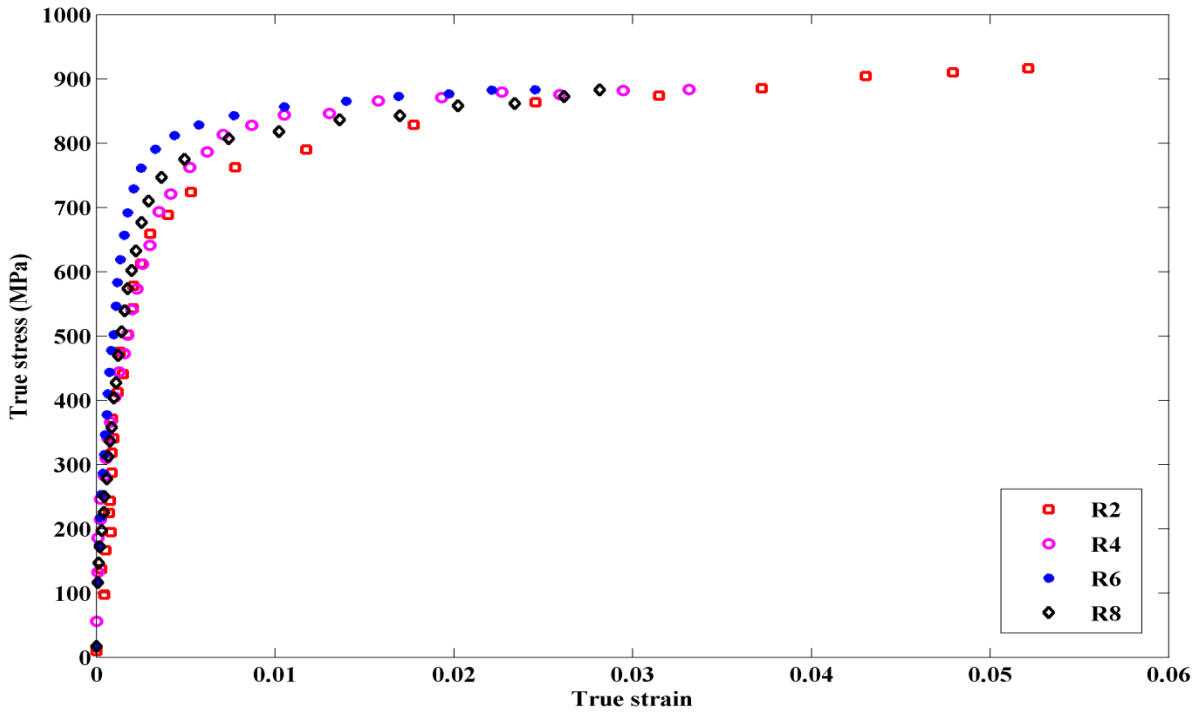

(d) A80284

Fig. 2.8: Experimental results of HR780SF steel samples with different notches

Fig. 2.9 shows the comparison of engineering stress-strain relations for sheet steel samples with the same notch radii of 2 mm and 8 mm, respectively. For samples with a notch radius of 2 mm, steel A80273 provide the largest range of strain and it failed at a strain around 0.17, while steels A80283 and A80284 failed at a strain around 0.013. However, for samples with a notch radius of 8 mm, steel A80284 is observed to have the largest range of strain while A80283 has the shortest range of strain. Failure happens at a strain around 0.03 for samples A80273 and A80274. For overall behavior, steel sample A80274 exhibits the largest true stress while sample A80283 exhibits the smallest true stress. The range of strain decreases with increasing notch size.

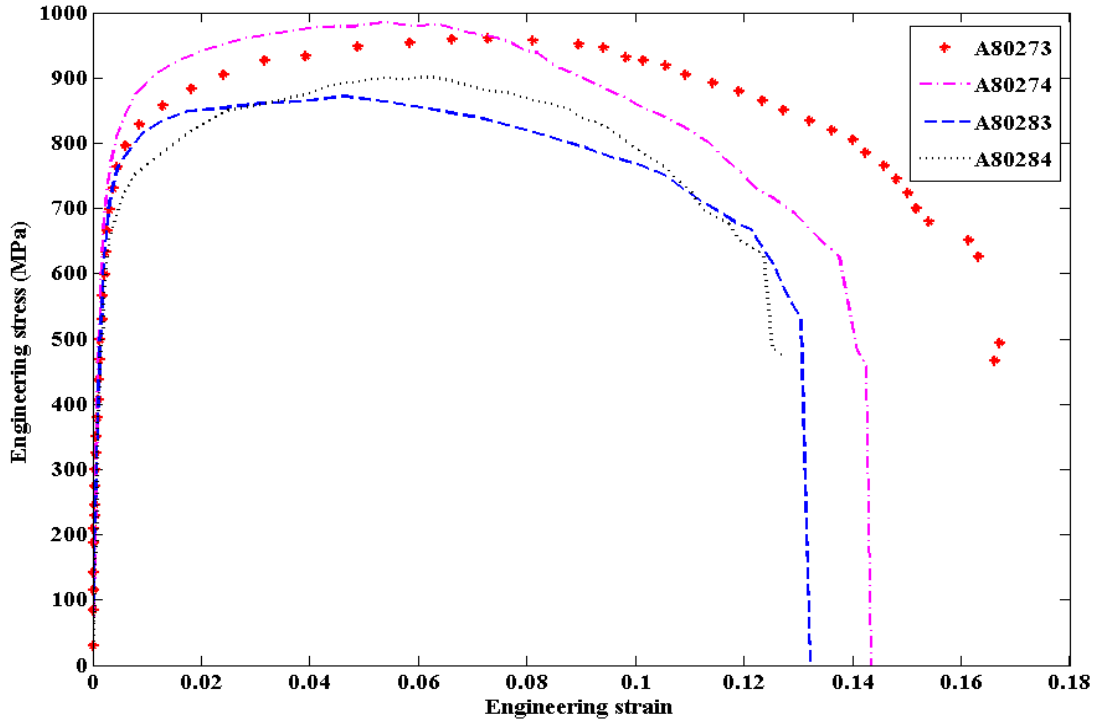

(a) R2

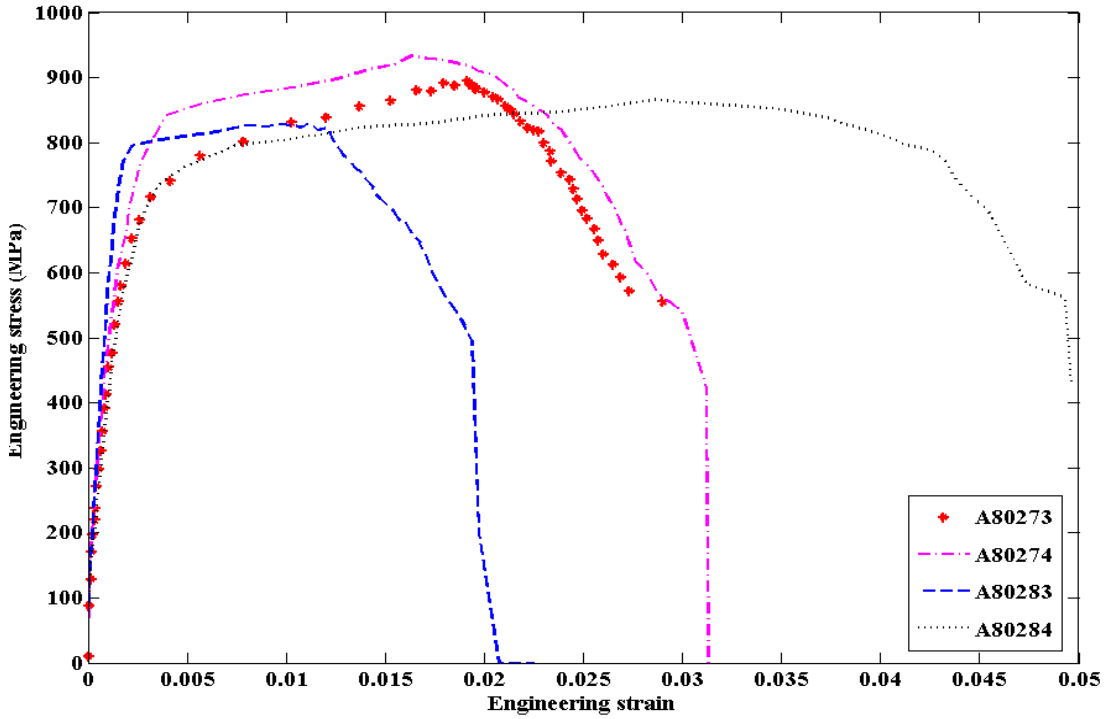

(b) R8

Fig. 2.9: Comparison of engineering stress-strain relations of sheet samples with the same notch

2.4. Microstructure

A preliminary investigation of microstructure of HRSF steel samples was performed. Two pieces of material from different locations of the steel samples were cut and mounted in epoxy resin. Fig. 2.10 shows the positions that were investigated. Since most of changes occurred at the neck area (ligament), the microstructure of the neck was compared with the microstructure of the base. Two procedures were applied to prepare samples for optical microscopy. Firstly, the samples were polished to a three micron surface finish; secondly, a 2% Nital acid solution was used to etch the sample for 1 minute. The purpose of this etching process is to reveal the grain boundaries. Microstructure at the base and the neck for samples A80273, A80274, and A80284 are shown in Fig. 2.11, 2.12, and 2.13. Only microstructure for samples with R2 and R8 is shown in these figures. It can be observed that the microstructure at the base is not affected by tensile tests. However, microstructures at neck are significantly affected. Ferrite, bainite and a small fraction of martensite are main phases in the microstructure of HRSF steels. However, it is hard to distinguish martensite and bainite by using optical microscope. Scan electron microscope (SEM) and additional etching methods can be used to accurately distinguish different phases.

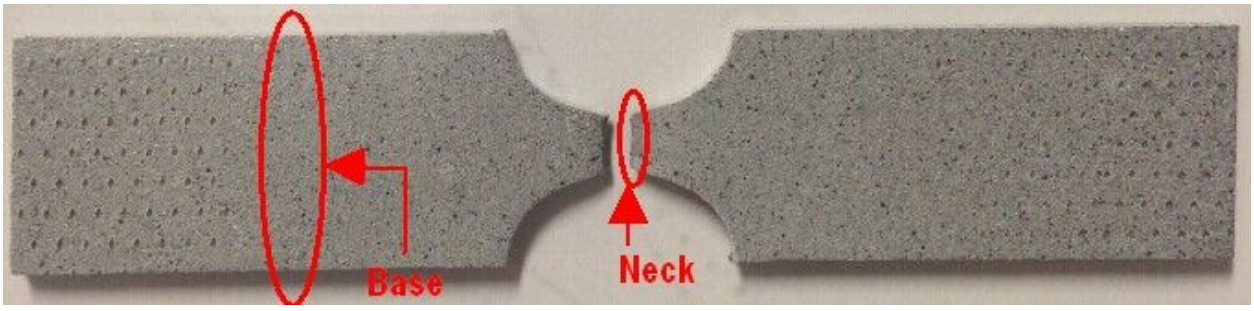

Fig. 2.10: Selected positions of base and neck of the steel sample

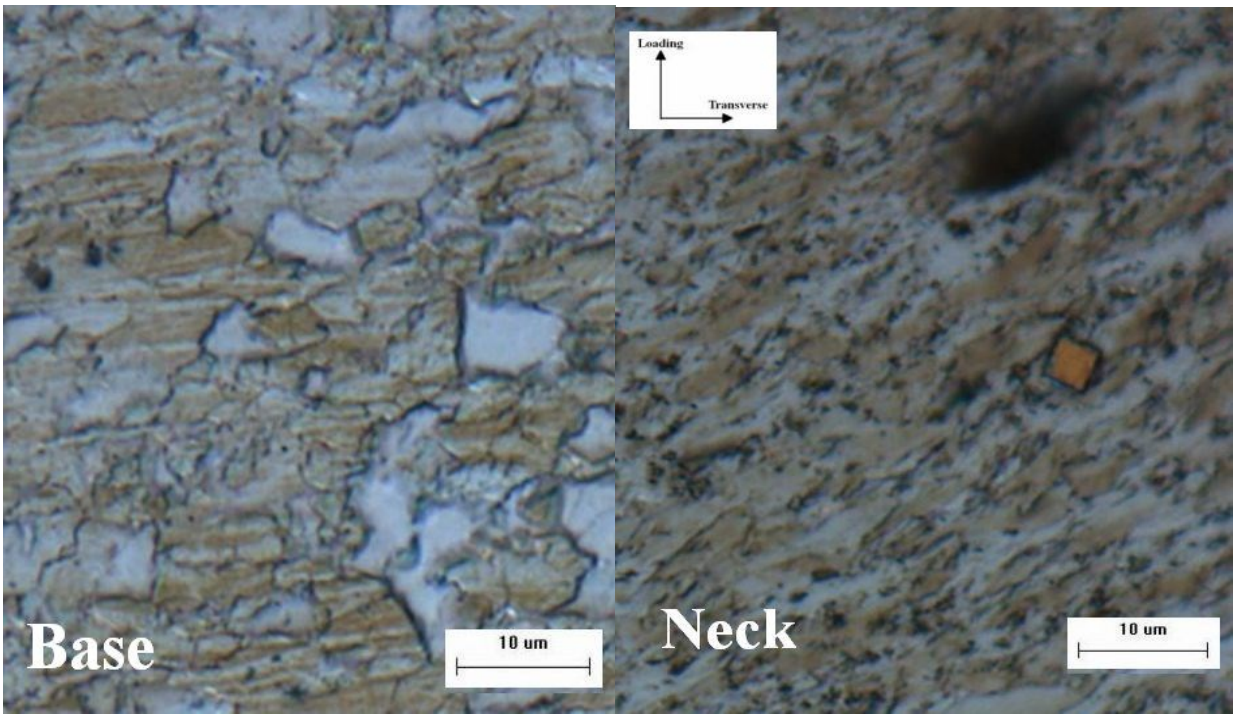

(a) R2

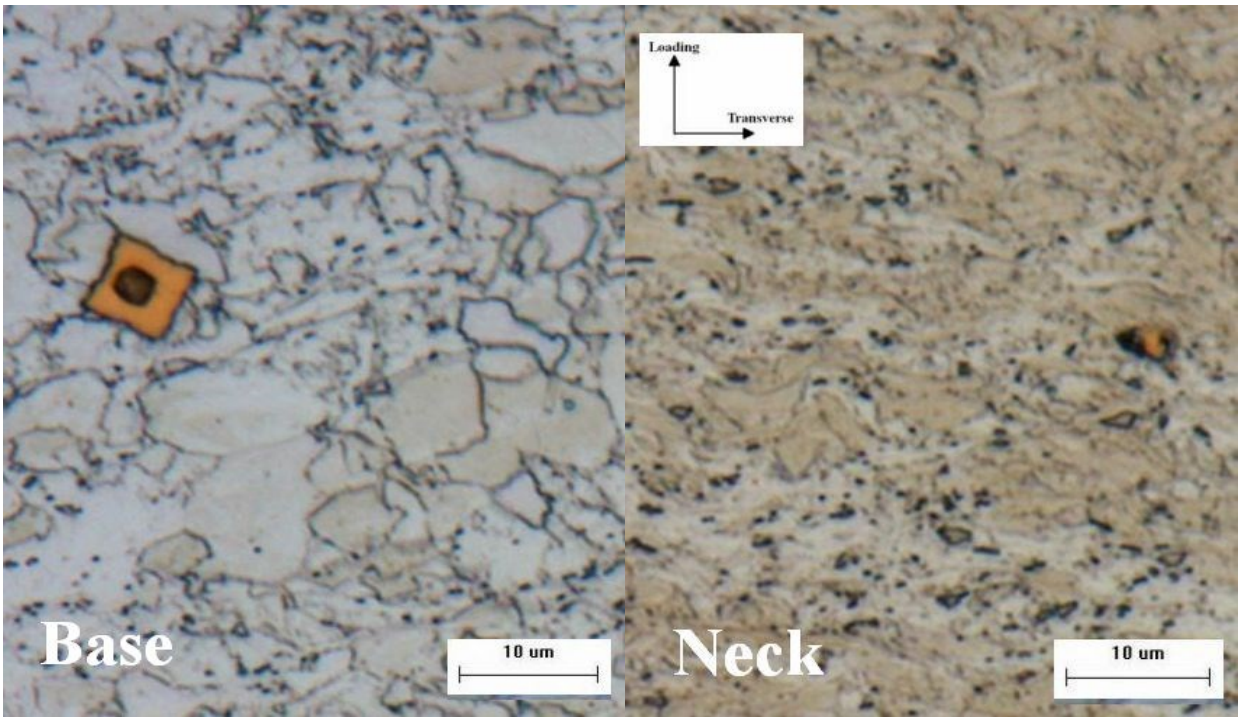

(b) R8

Fig. 2.11: Microstructures at base and neck for samples A80273 R2 and R8

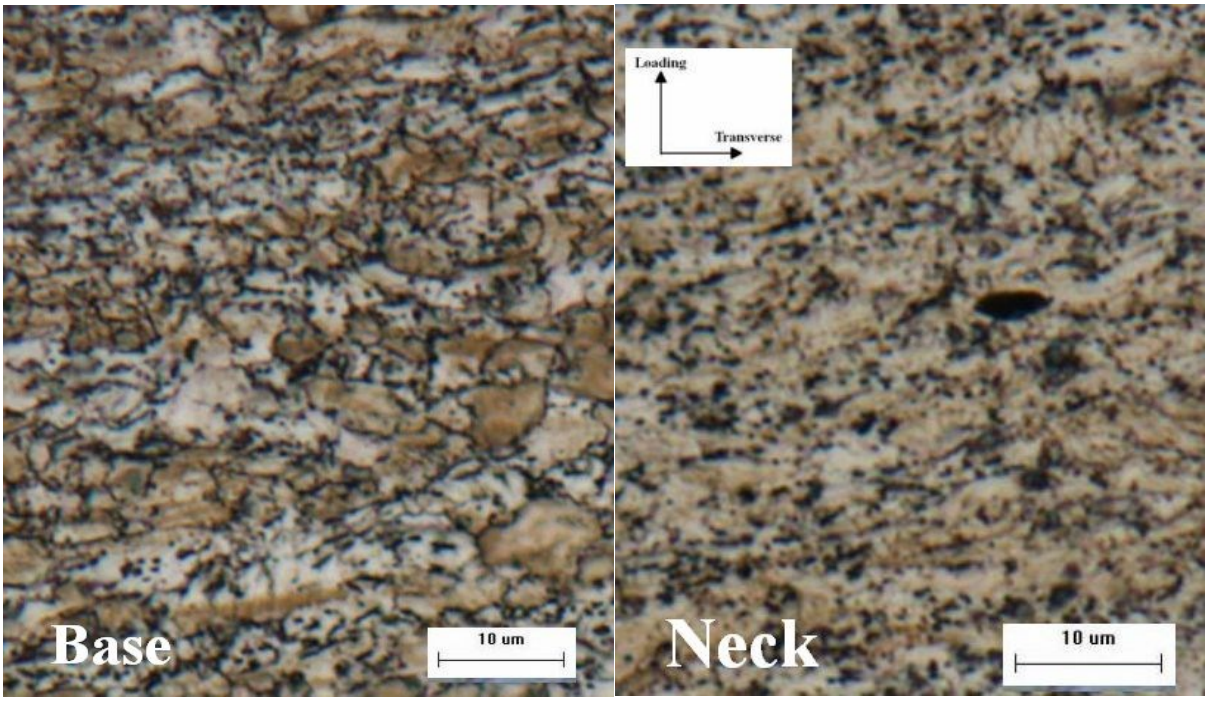

(a) R2

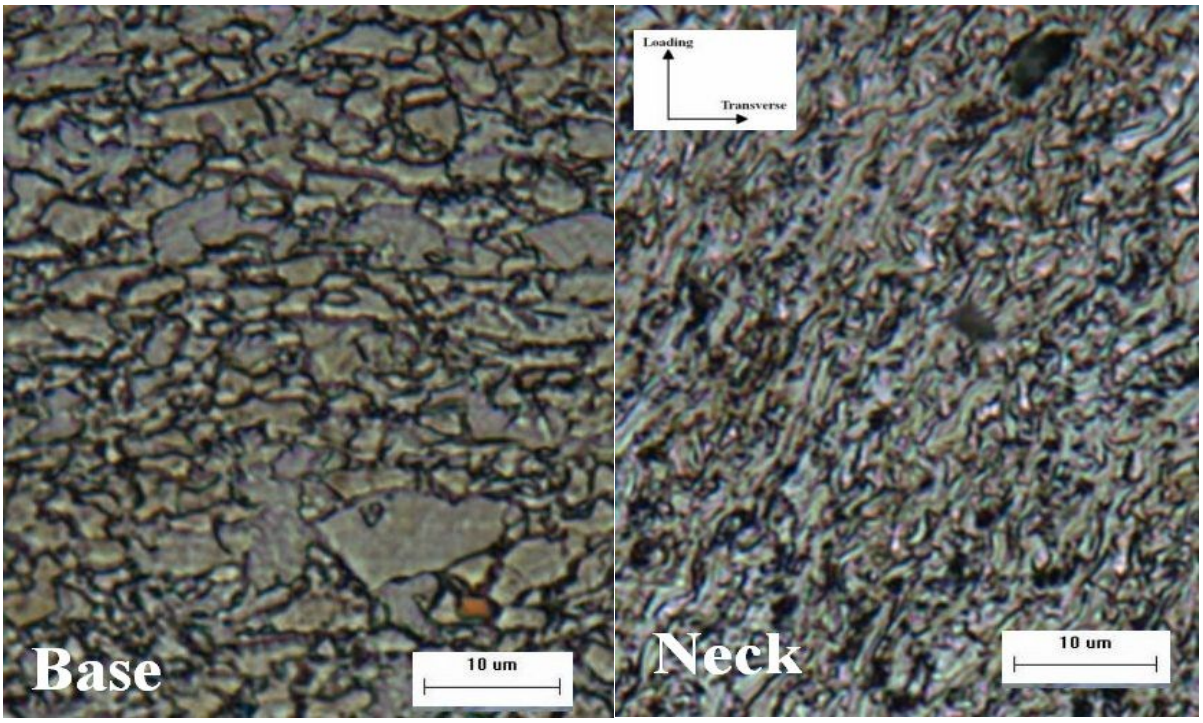

(b) R8

Fig. 2.12: Microstructures at base and neck for samples A80274 R2 and R8

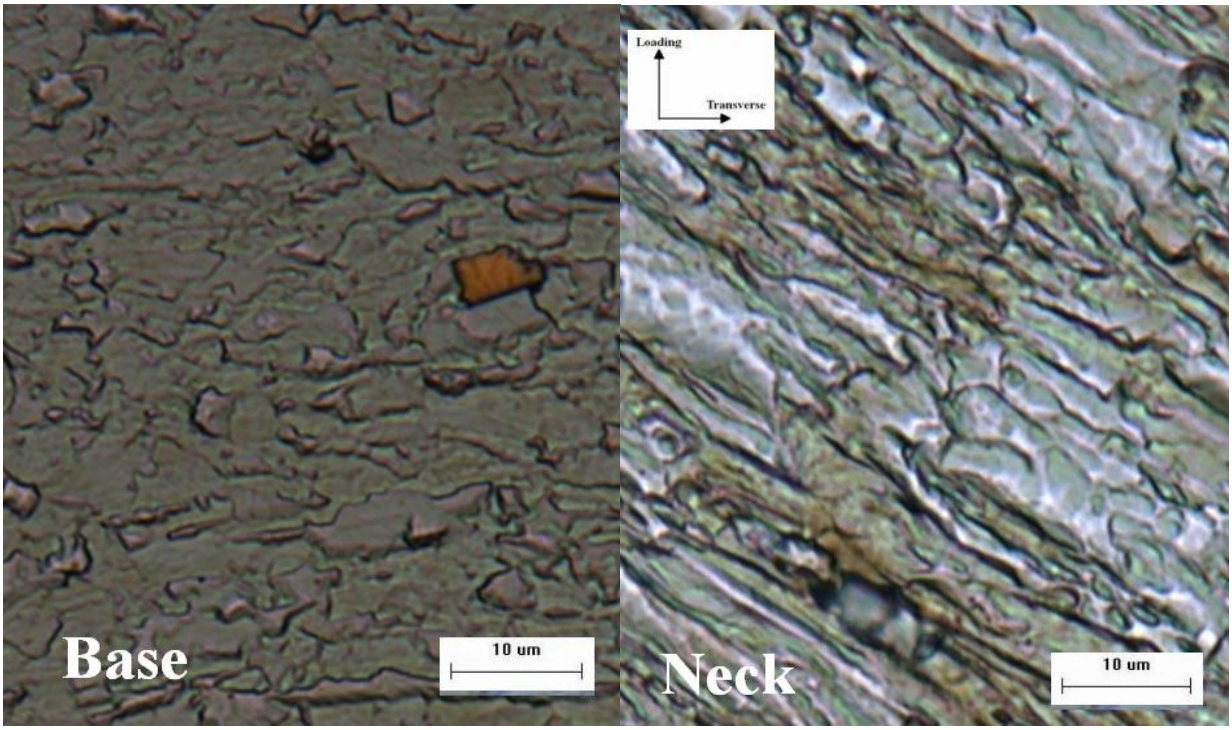

Fig. 2.13: Microstructures at base and neck for sample A80284 R8

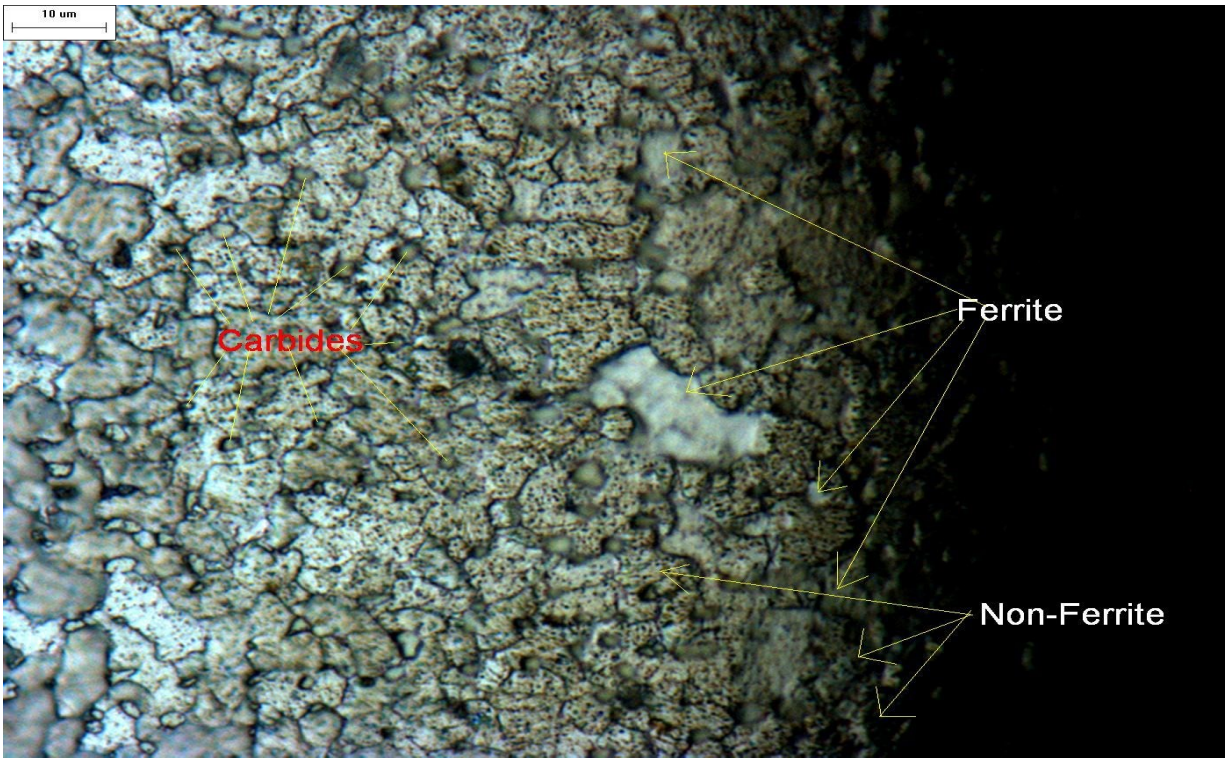

Fig. 2.14: Different phases of the microstructure for HRSF steels

Figures 2.11, 2.12 and 2.13 showed that the grains were elongated in the direction of maximum shear stress, which also indicated the slip direction. It is very clear from figures 2.12 and 2.13 that the slip direction of the material was deviated from the 45^{o} direction with respect to the loading direction of the test. This indicates that the material was experiencing a triaxial stress state other than uniaxial stress state within the notched region. The actual maximum shear stress is therefore deviated from the 45^{o} direction with respect to the loading direction. Micro-voids were observed in the microstructures of neck areas. As shown in Fig. 2.14, small black dots are carbides. Lower or lighter areas are ferrite, while higher or darker areas are bainite or a combination of bainite and martensite.

3. Finite Element Simulation of the Notched Tensile Test of Hot Rolled Steels

3.1. Uniaxial Tensile Test

The HR steels are considered to be isotropic, elasto-plastic solids and the plasticity model used for the sheet steel specimens is the J_2-flow theory. The sheet steel follows the flow rule of Hollomon's equation [30]

$$\sigma = K' p^n \tag{3.1}$$

where p is the accumulated plastic strain, and K' and n refer to hardening modulus and hardening exponent, respectively. Material properties for the sheet steel samples are shown in Table 3.1, where E and υ refer to Young's modulus and Poisson's ratio, respectively. These data were provided by the research group at University of Waterloo. All simulations in this thesis are done by using *ABAQUS/Standard* [31].

Table 3.1: Averaged material properties of sheet steel samples used in the finite element simulation [21]

Material	**E(MPa)**	**ν**	K'	**n**
A80273	194503	0.28	1122	0.0843
A80274	190000	0.28	1100	0.0856
A80283	186000	0.28	1085	0.0817
A80284	185000	0.28	1180	0.095

Since the geometry of sheet steel sample is not complex, the finite element model was meshed with 8-node linear brick elements (C3D8R) with reduced integration and hourglass control. The number of elements for each model was approximately 10,000. Special care was taken to avoid or minimize the number of distorted elements during meshing. Each mesh was checked for mesh sensitivity which was found negligible for a sufficiently refined mesh. A finer meshed model with approximately 70,000 elements was used to check the fineness of the finite element mesh. The percentage difference of maximum force was 0.21%. The effect of element type (linear element and quadratic element) was also checked and the percentage difference of maximum reaction force was 0.54%. Therefore, linear element and standard mesh were chosen to be used in all finite element simulations to save computational resources without affecting the accuracy of results. A typical finite element model with standard mesh and finer mesh were shown in Fig. 3.1 and Fig. 3.2, respectively. In order to resemble a uniaxial tensile test, a small displacement was applied on the right end of the sample in the x-direction. The other end of the sample was held fixed. Rotations in all directions were constrained.

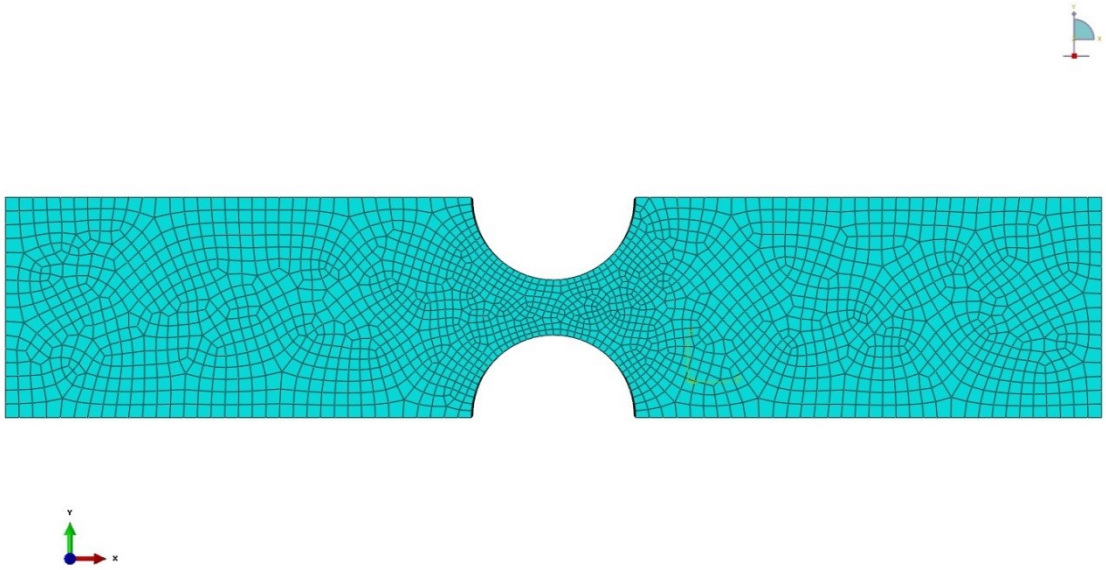

Fig. 3.1: Finite element model of a circular-notched sheet sample with 6 mm notch radius and ligament size of 4 mm

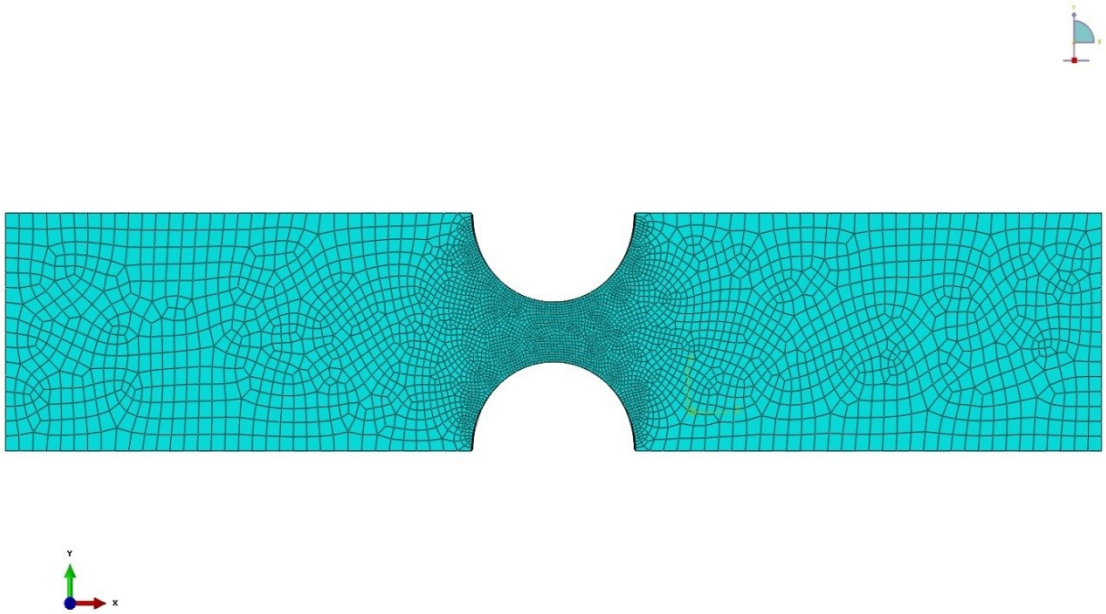

Fig. 3.2: Finite element model (finer mesh) of a circular-notched sheet sample with 2 mm notch radius and ligament size of 4 mm

3.2. Results and Discussion

Three different methods are applied to obtain the true stress for HR steel samples. The stress-strain curves for sample A80273 with notch radius of 4 mm are shown in Fig. 3.3. For the dark curve, the true stresses are directly converted from engineering stresses which are obtained through dividing reaction force by the nominal cross-sectional area; for the blue curve, the true stresses are the average of the direct output of the normal stresses in the loading direction of multiple elements at the center of the ligament; for the red curve, the true stresses are the output normal stresses in the loading direction of a single element located at the center of the ligament. In this research, the first method is used to obtain the true stress.

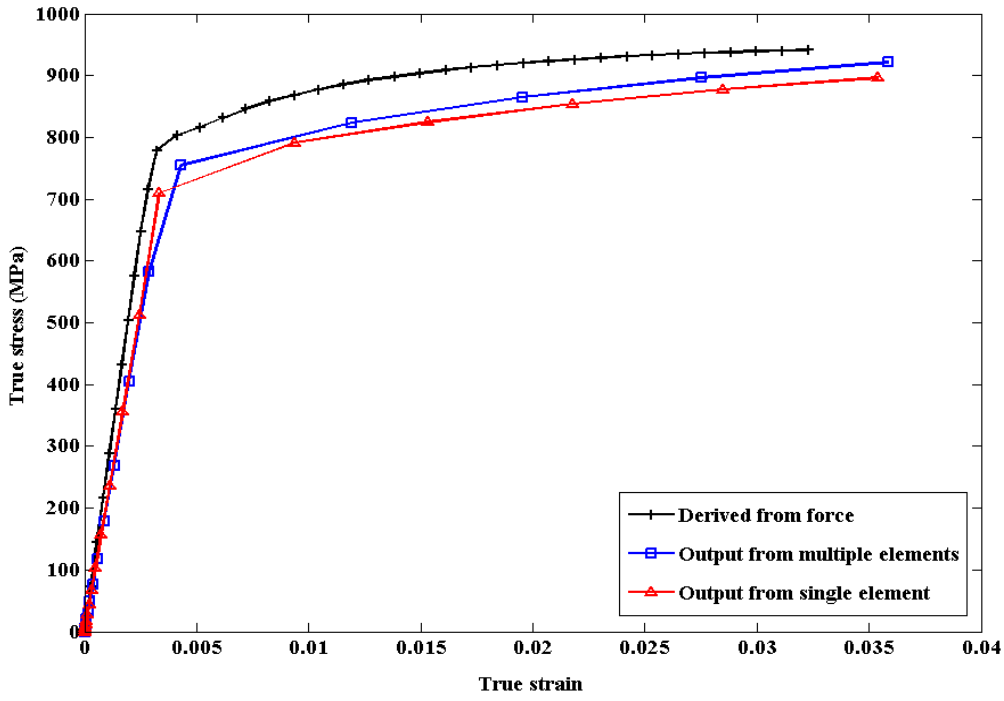

Fig. 3.3: Stress-strain curves using different methods (Sample A80273 R4)

The results of finite element simulations for each grade HR steel samples are shown in Fig. 3.4. In finite element simulations, the true stresses are obtained by converting engineering stresses. The true strains are obtained from the nodes of the ligament area of HR steel samples. It can be observed that samples with the smallest notch exhibit the strongest stress-strain behavior while samples with the largest notch predict the softest stress-strain behavior. However, these stress-strain curves are all clustered at the beginning of yielding. The stress-strain curves start to differentiate as plastic deformation proceeds, which is in agreement with the experimental results.

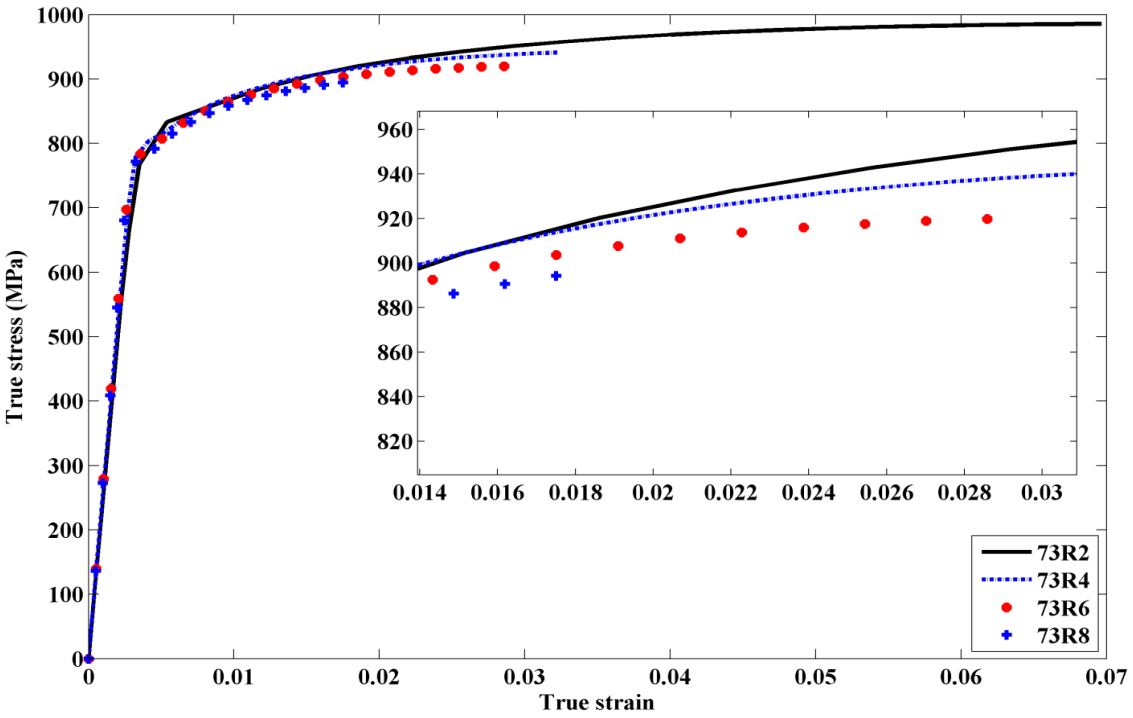

(a) A80273

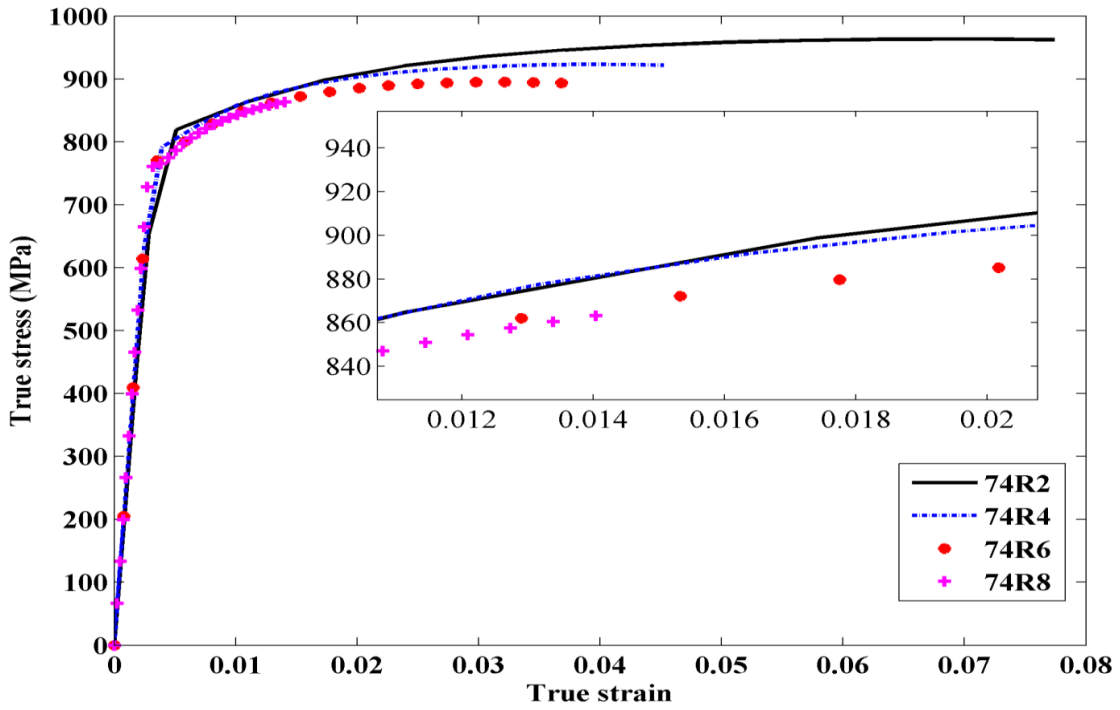

(b) A80274

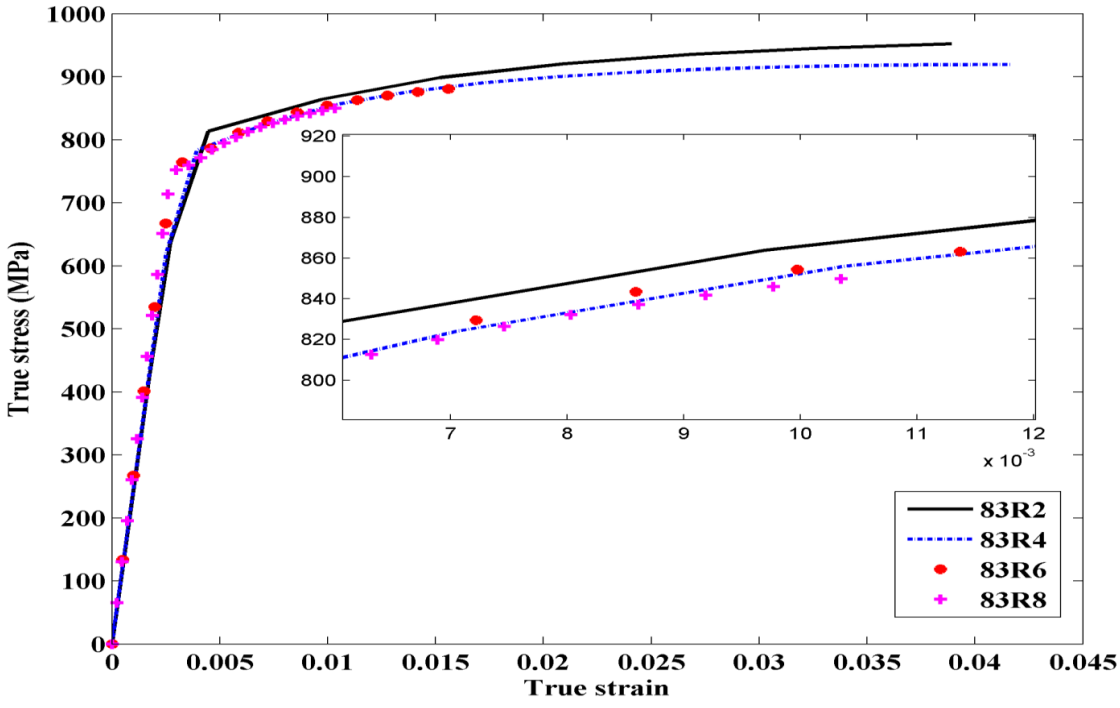

(c) A80283

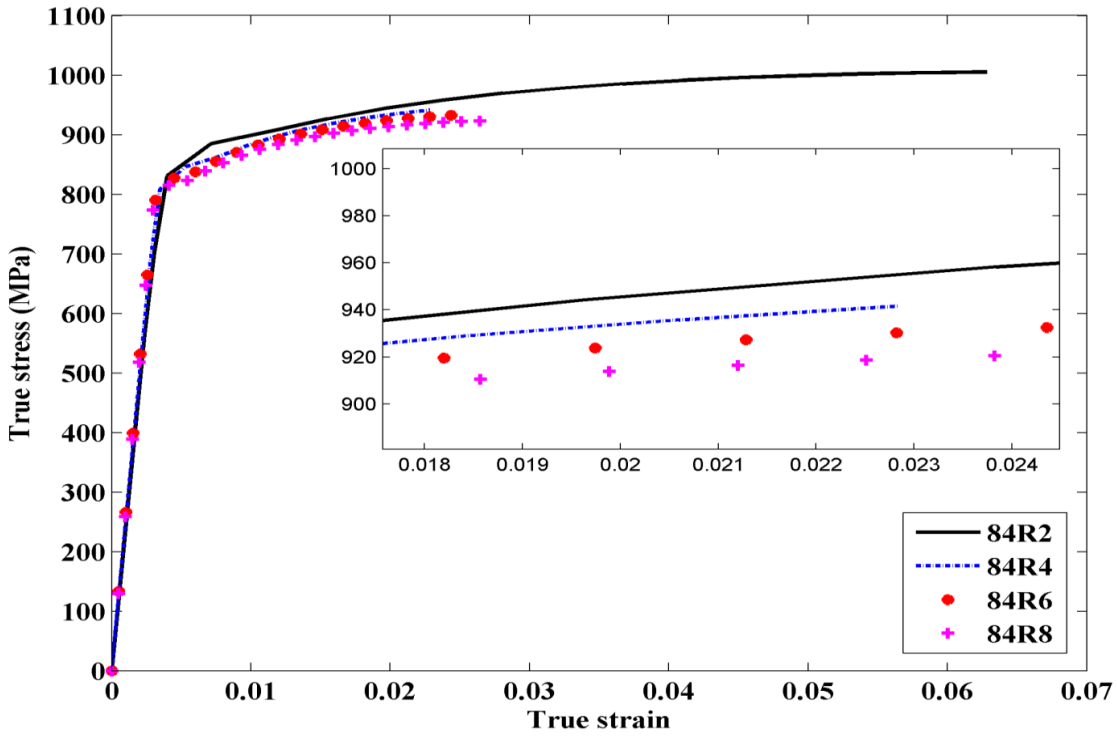

(d) A80284

Fig. 3.4 Stress-strain relations for HR780SF sheet steel samples

3.3. Stress Triaxiality

Steel samples with different notch geometries can induce different stress states in the sheet material, and stress triaxiality is one measurement of stress states. By comparing stress triaxialities, the effects of notch geometry on the stress state can be observed. Two elements A and B, which are located at the edge and center of the ligament, were selected to study the effects of notch geometry on the stress triaxiality [32, 33]. A model of one-eighth of the circular-notched sheet steel sample was shown in Fig. 3.5, where elements A and B were highlighted. The changes in stress triaxiality of a local element were captured during the deformation. The

effects of notch geometry on stress triaxiality at different locations of the notched area were also investigated. The stress triaxiality is defined as [34, 35].

$$T = \frac{\sigma_{hyd}}{\sigma_{eq}} \tag{3.2}$$

where σ_{hyd} and σ_{eq} are the hydrostatic stress and von Mises equivalent stress, respectively. They are expressed as

$$\sigma_{hyd} = \frac{\sigma_1+\sigma_2+\sigma_3}{3} \tag{3.3}$$

$$\sigma_{eq} = \sqrt{\frac{1}{2}[(\sigma_1 - \sigma_2)^2 + (\sigma_2 - \sigma_3)^2 + (\sigma_3 - \sigma_1)^2]} \tag{3.4}$$

where σ_1, σ_2 and σ_3 are principal stresses.

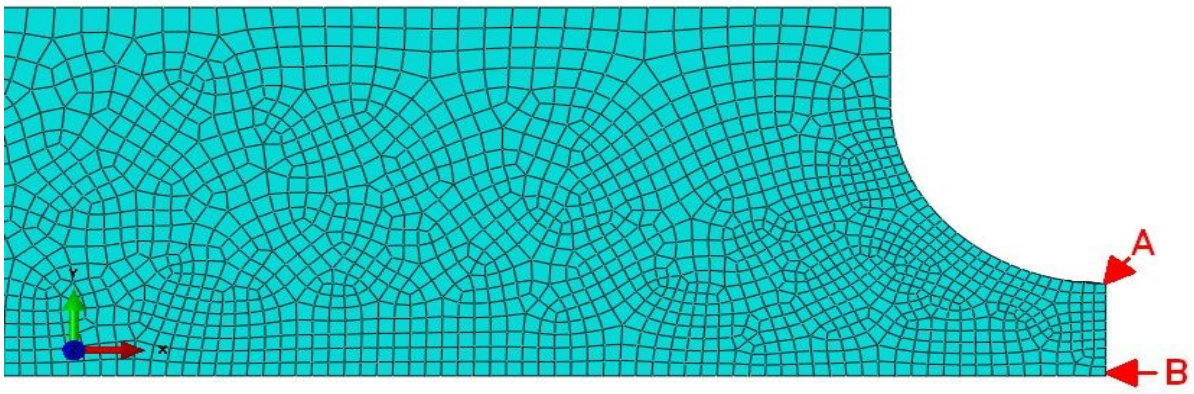

Fig. 3.5: Elements selected for stress triaxiality analysis

Loadings are the same as before, but appropriate boundary conditions need to be applied since it is only one-eighth of the whole model. The results of hydrostatic stress and equivalent stress

were extracted from *ABAQUS/Standard* [31], and the stress triaxialities were obtained by using Eq. (3.2). Thus, the stress triaxiality can be plotted as a function of equivalent plastic strain. Fig. 3.6 shows the numerical predictions of stress triaxilities for the four notch radii of the HR steels. For element B which is located at the center of the ligament, samples with the smallest notch (R2) exhibits the largest stress triaxiality levels while samples with the largest notch (R8) provide the lowest stress triaxiality levels. Similar behaviors can be observed for element A which is located at the edge of the ligament. However, unlike element B, the stress traxialities for samples with 6 mm and 8 mm of notch radius are clustered, which indicates that the effects of notch geometry are limited at the edge of the ligament. The changes in stress triaxiality levels become smaller and exhibit the tendency to stability as notch radius increases. Note that the size of ligament was fixed at a value of 4 mm.

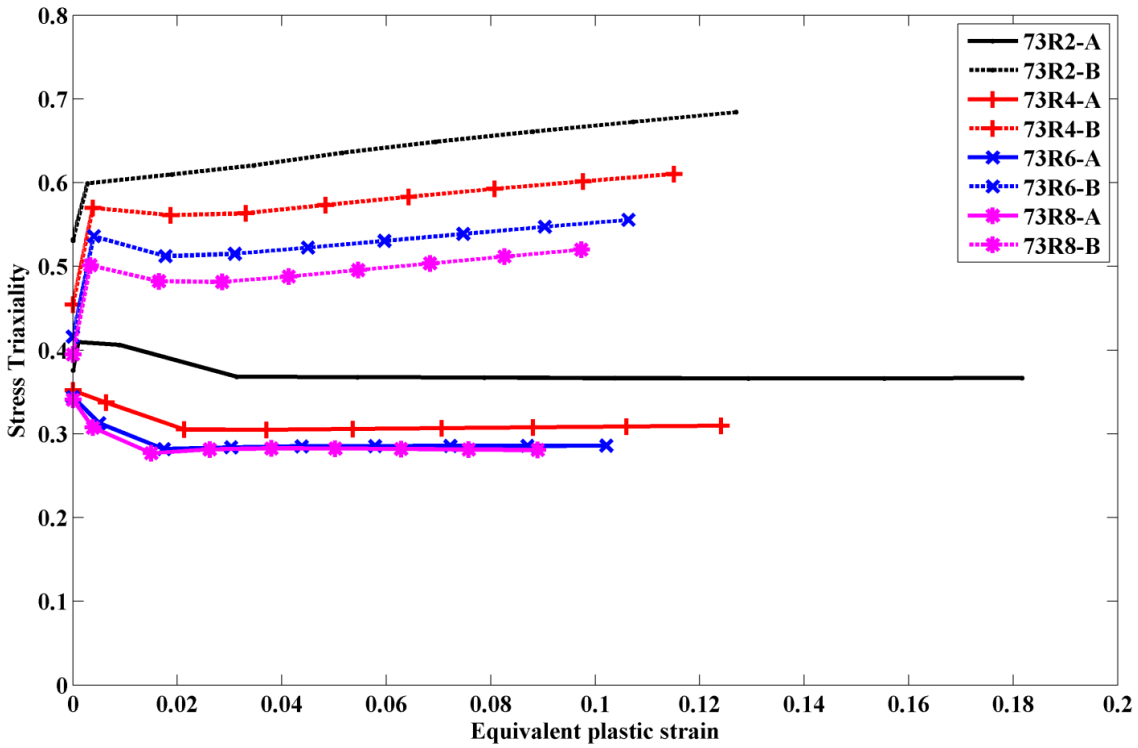

(a) A80273

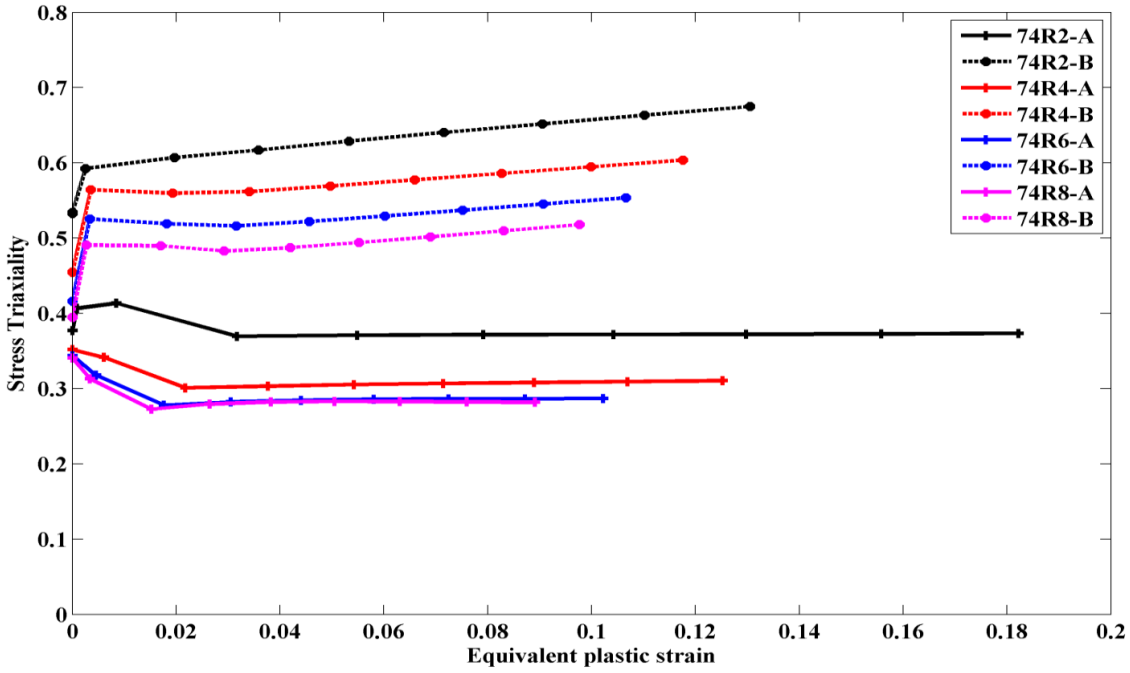

(b) A80274

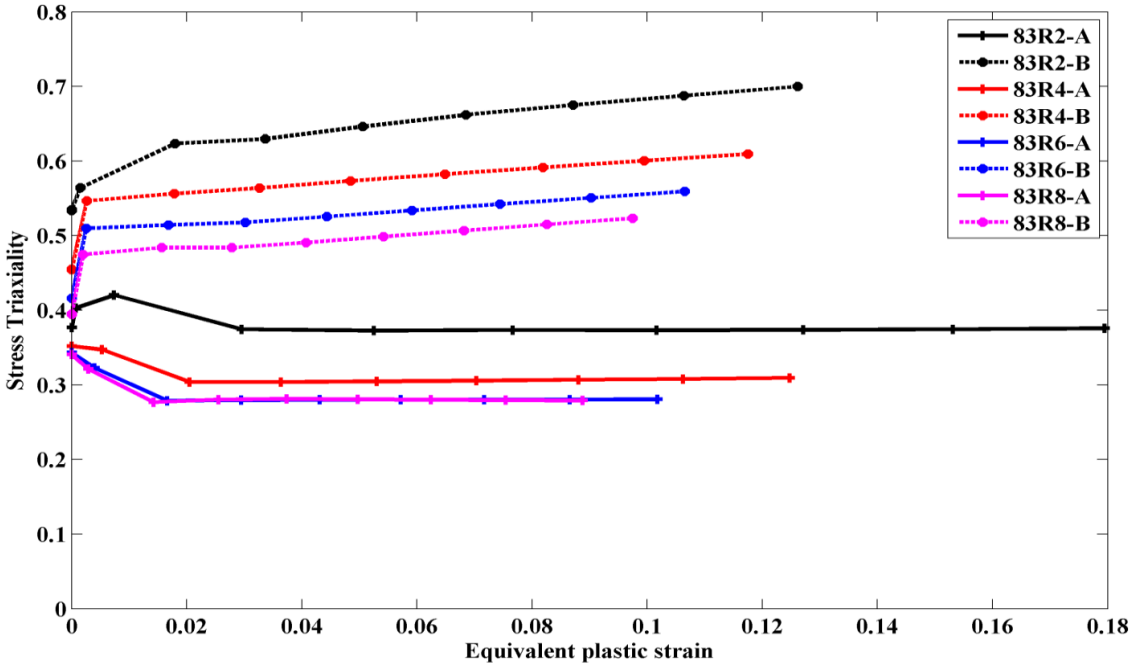

(c) A80283

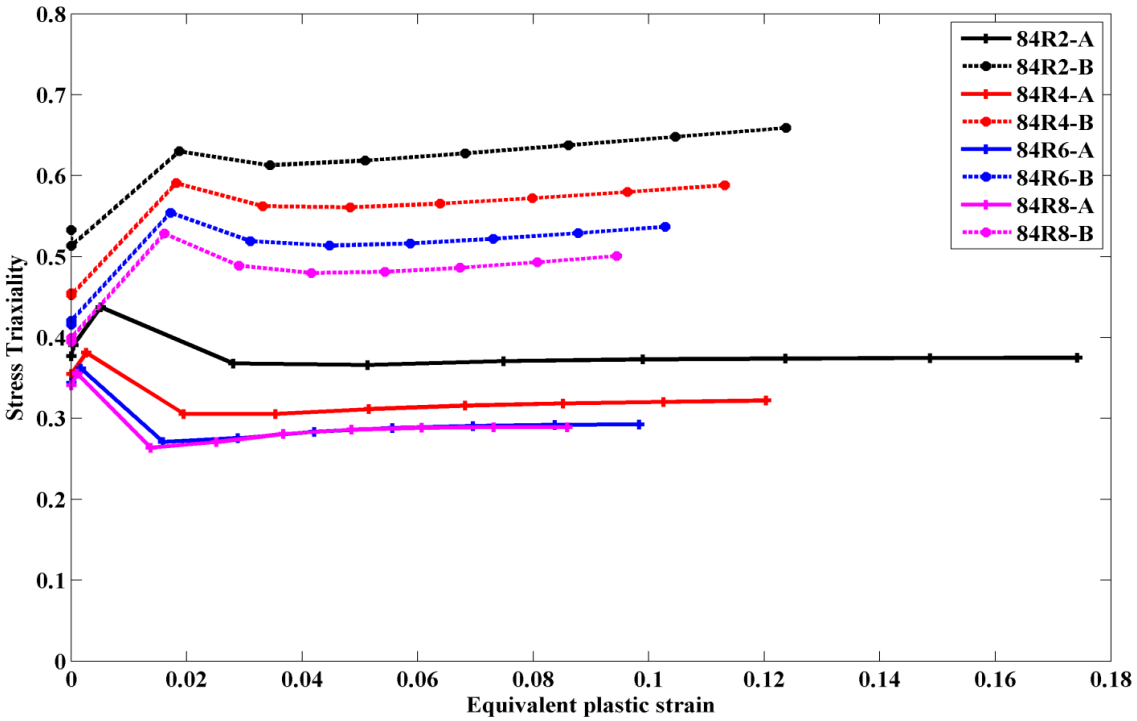

(d) A80284

Fig. 3.6: Comparison of stress triaxiality of element A and B

Fig. 3.7 shows the stress triaxiality of element A and B for different steel samples with the same notch. It clearly shows that stress triaxiality at the center of the ligament (element B) starts to increase as equivalent plastic strain increases. However, for element A, stress triaxiality starts to increase at first, and then decrease and become stable at last. This explains that the localized yielding occurs at the center of the ligament (element B) first. The localized yielding leads to the increase in stress triaxiality. Then, local stresses are redistributed and the stress concentration effect of notch geometry is reduced. This leads to a decrease in stress triaxiality levels. After the entire cross section of the ligament yields, stress triaxiality starts to increase again as strain increases [6, 36]. For element A, it can be seen that the stress triaxiality starts at a range of 0.35

to 0.4, and then reaches the stability at values around 0.35, 0.3, 0.28 and 0.28 for notch radius of 2 mm, 4 mm, 6 mm and 8 mm, respectively. It decreases as notch radius increases. For element B, it starts at a range of 0.4 to 0.55, then increase as equivalent plastic strain increases. The largest values of stress triaxiality levels of element A are found to be 0.7, 0.61, 0.56, and 0.52 for notch radius of 2 mm, 4 mm, 6 mm and 8 mm, respectively. Steel sample A80283 exhibits the largest stress triaxiality levels for element B while sample A80284 exhibits the smallest levels.

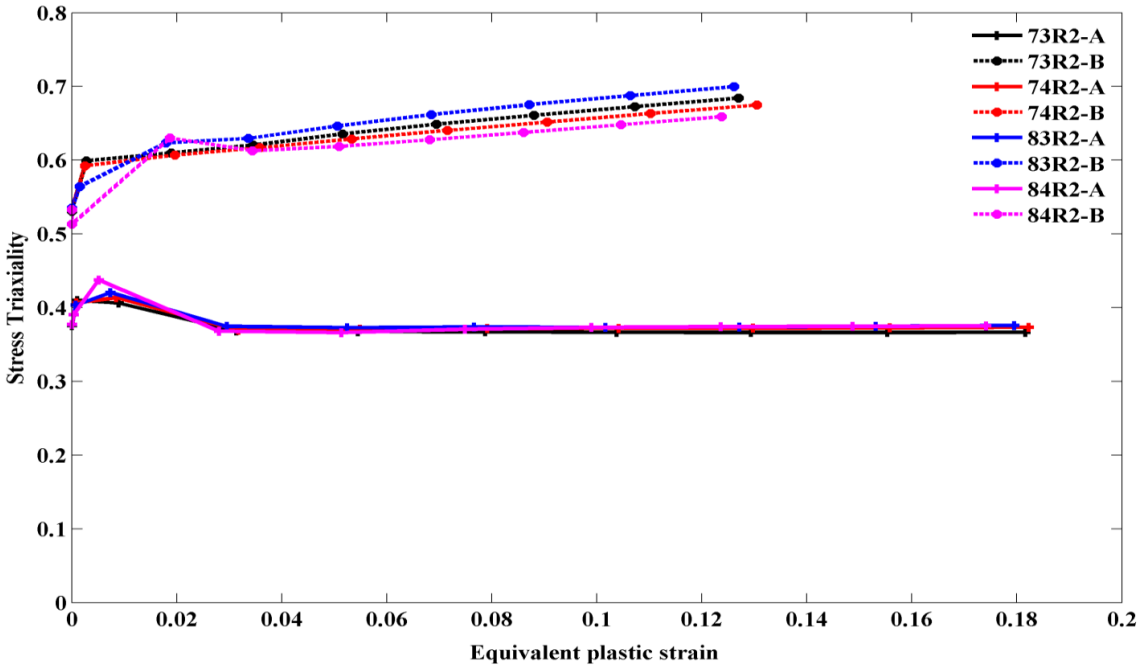

(a) R2

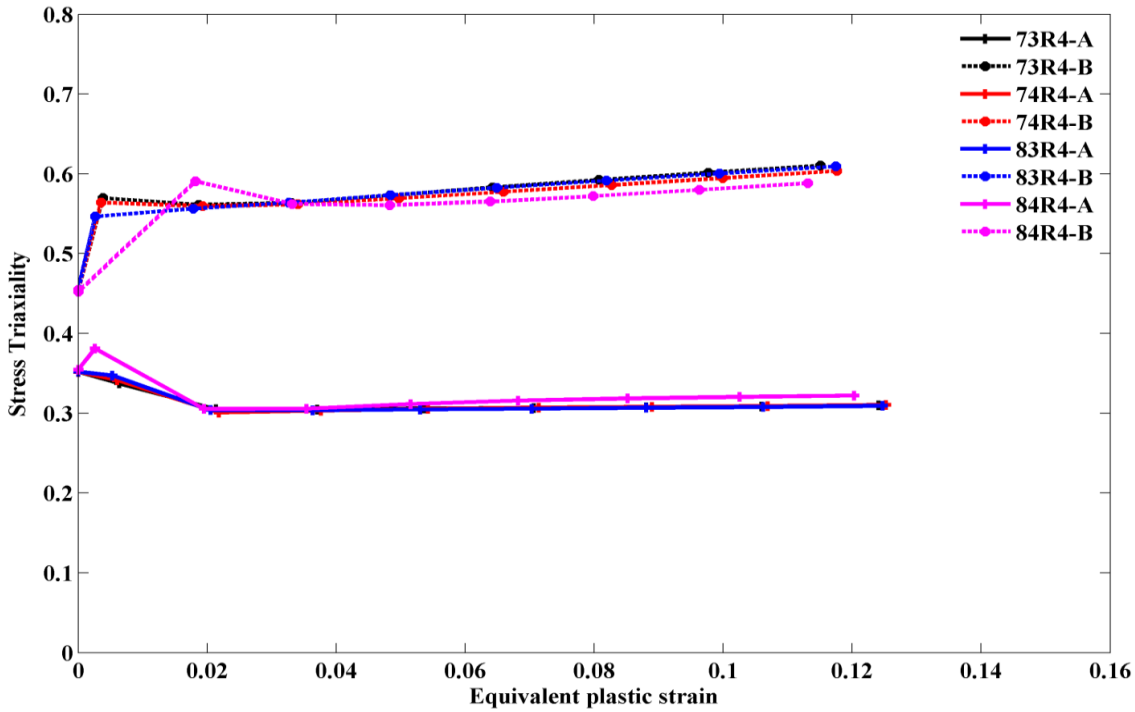
Stress Triaxiality
Equivalent plastic strain
0
0.1
0.2
0.3
0.4
0.5
0.6
0.7
0.8
0.02
0.04
0.06
0.08
0.1
0.12
0.14
0.16
73R4-A
73R4-B
74R4-A
74R4-B
83R4-A
83R4-B
84R4-A
84R4-B

(b) R4

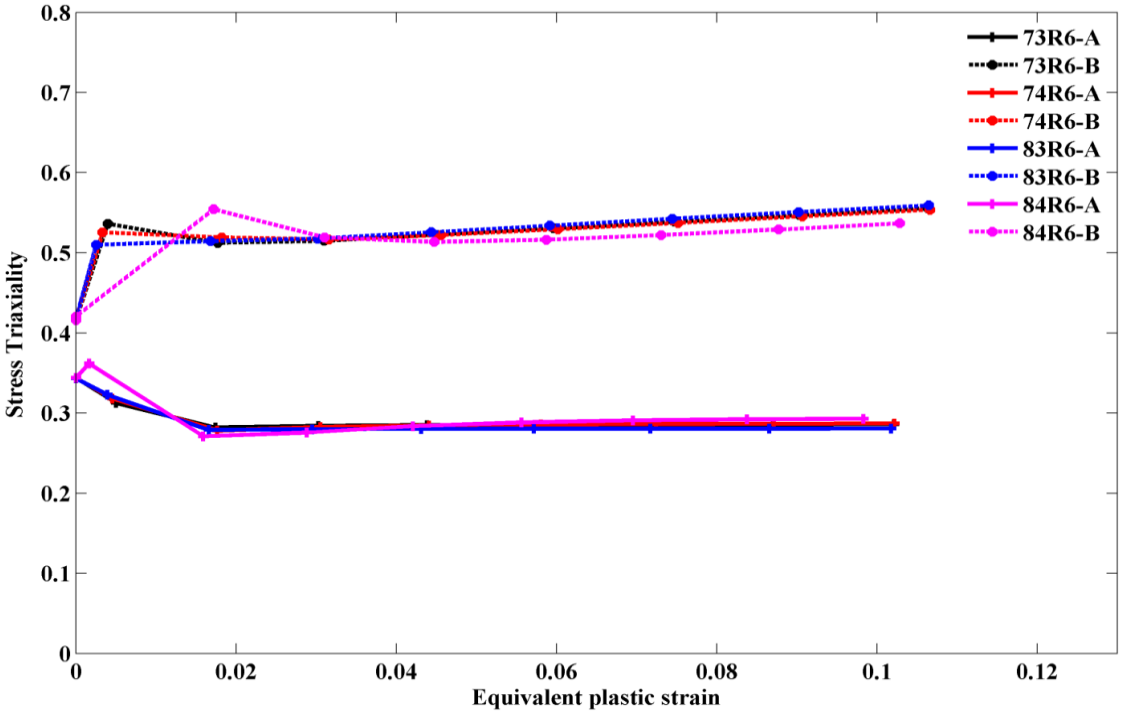
Stress Triaxiality
Equivalent plastic strain
0
0.1
0.2
0.3
0.4
0.5
0.6
0.7
0.8
0.02
0.04
0.06
0.08
0.1
0.12
73R6-A
73R6-B
74R6-A
74R6-B
83R6-A
83R6-B
84R6-A
84R6-B

(c) R6

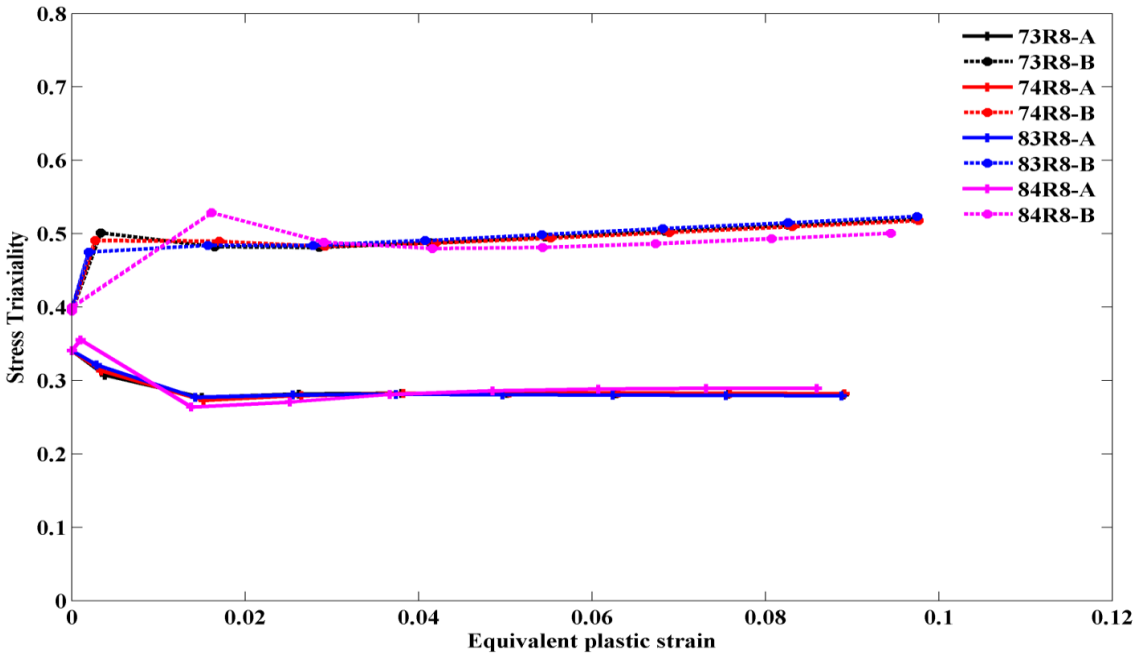

(d) R8

Fig. 3.7: Comparison of stress triaxiality of element A and B for different steel samples with the same notch

One point worth mentioning is that, generally, the stress triaxiality of element A for the sample with the smallest notch (R2) starts to increase and then decreases and reaches its stability while stress triaxiality levels of samples with other notch radii directly decrease and reach their stabilities. Steel samples A80284 are the exceptions. Stress triaxiality levels start to increase at first and then decrease and reach the stabilities are observed for all samples of steel A80284, no matter what the notch geometry is.

In order to find out the reason why stress triaxiality behaves like this, the normal stresses in the z-direction (out of the paper) of element A are extracted and plotted in Fig. 3.8. In Fig. 3.8 (a),

(b) and (c), the normal stress of element A in the z-direction of samples with R2 starts to increase at the beginning of deformation and then decreases and reach stability while the normal stress in z-direction of sample with R4, R6, and R8 directly decrease and then reach the stability. The behavior of normal stress σ_{33} is same as stress triaxiality, which indicates that the evolution of normal stress σ_{33} plays a dominate role in the variation of the stress triaxiality.

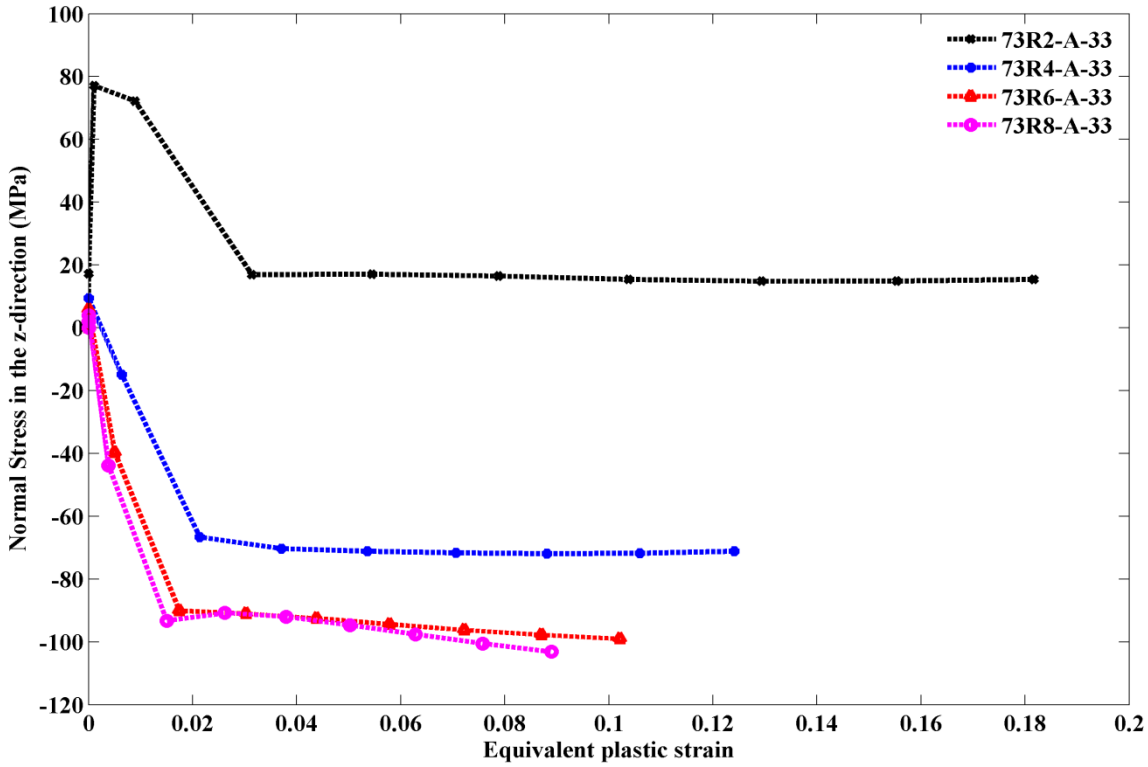

(a) A80273

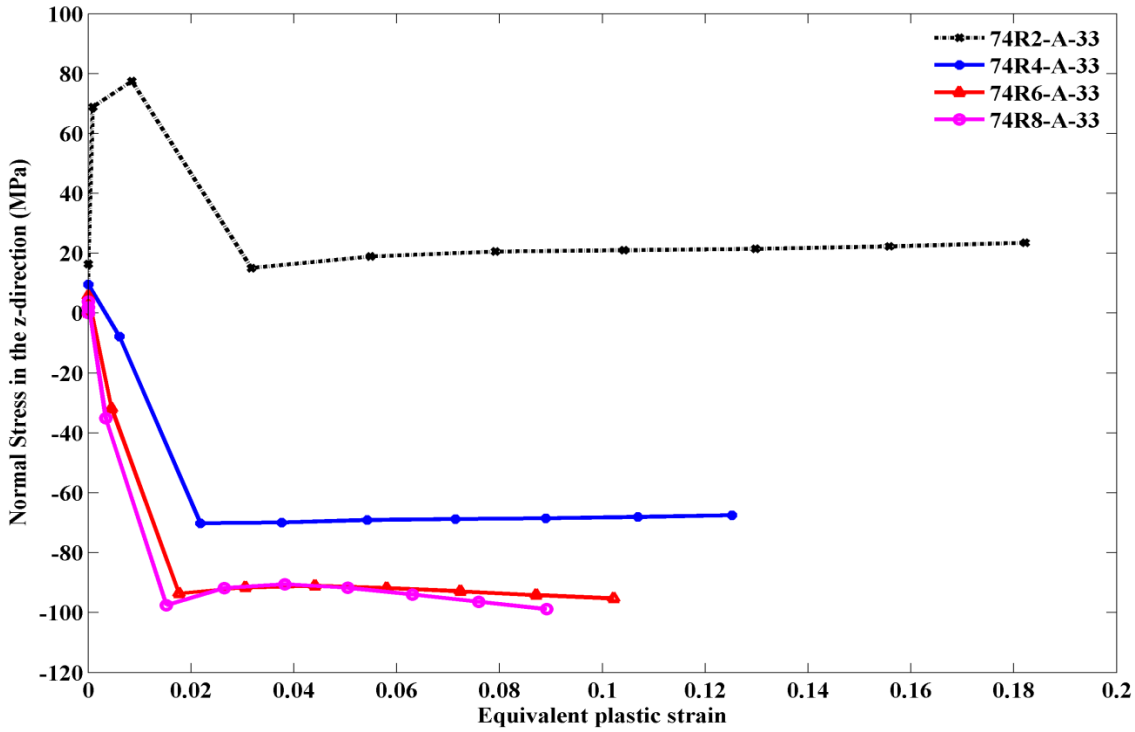

(b) A80274

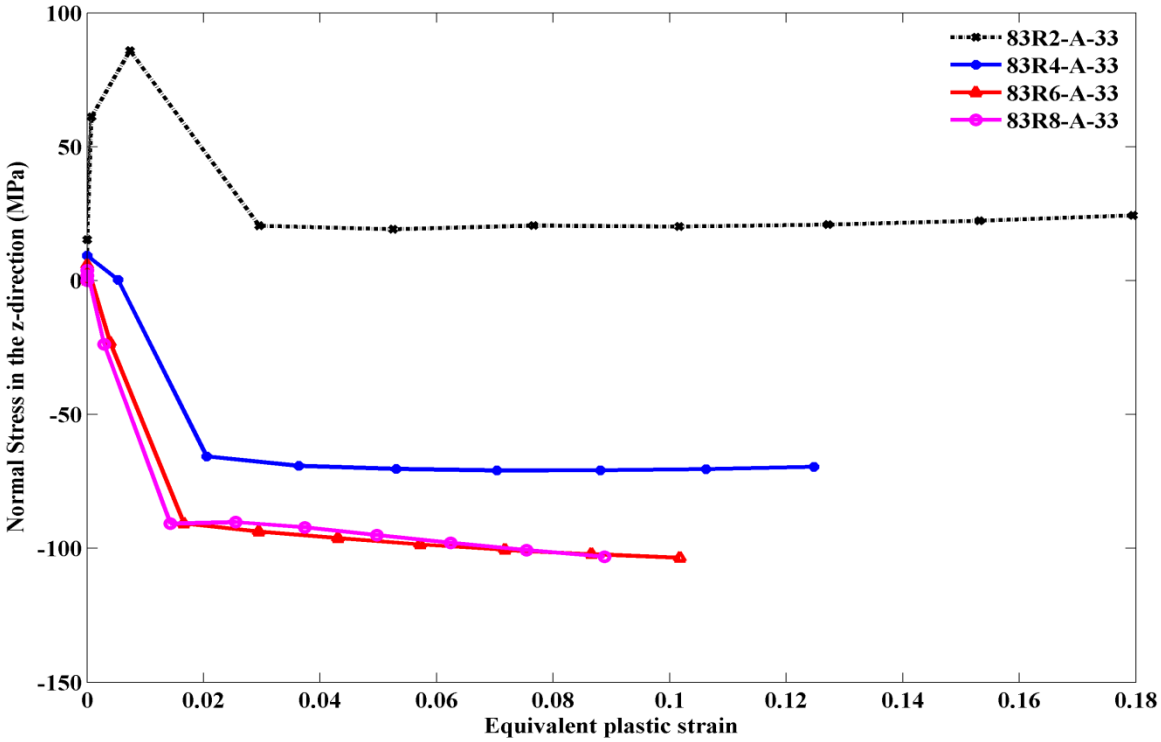

(c) A80283

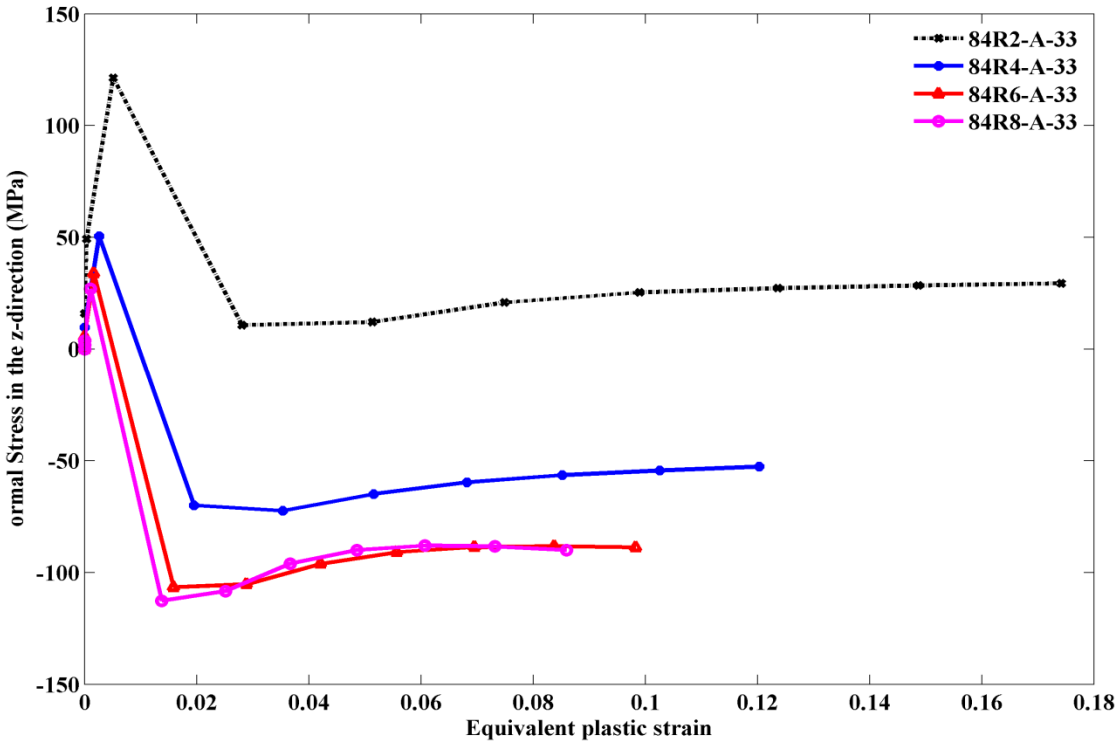

(d) A80284

Fig. 3.8: Comparison of principal stress in Z-direction of element A

4. Comparison between Results of Experiment and Numerical Simulation

4.1. Introduction

This chapter is devoted to compare and discuss the results of both experiment and finite element simulation of circular notched steel samples as introduced in the previous chapters. Possible error sources which may cause the discrepancy between results of experiment and finite element simulation are also discussed.

4.2. Results and Discussion

The comparison of FE results and experimental results for steel sample A80273 are shown in Fig. 4.1. For sample A80273 with notch radius of 2 mm, two curves almost coincide, as shown in Fig. 4.1 (a). Images for different stages were captured by digital camera *Nikon D300s*, contour plots at the same time were exported from *ABAQUS/Standard* [31] to provide a more comprehensive understanding of the evolution of material behavior as shown in Fig. 4.1 (a). The maximum percentage difference of true stress is found to be 0.56%. It indicates that the prediction of finite element simulation is validated by experimental results. Comparisons for sample A80273 with different notch sizes are shown in Fig. 4.1 (b), (c) and (d). The maximum percentage differences of true stress are found to be 2.23%, 5.395 and 5.31%, respectively.

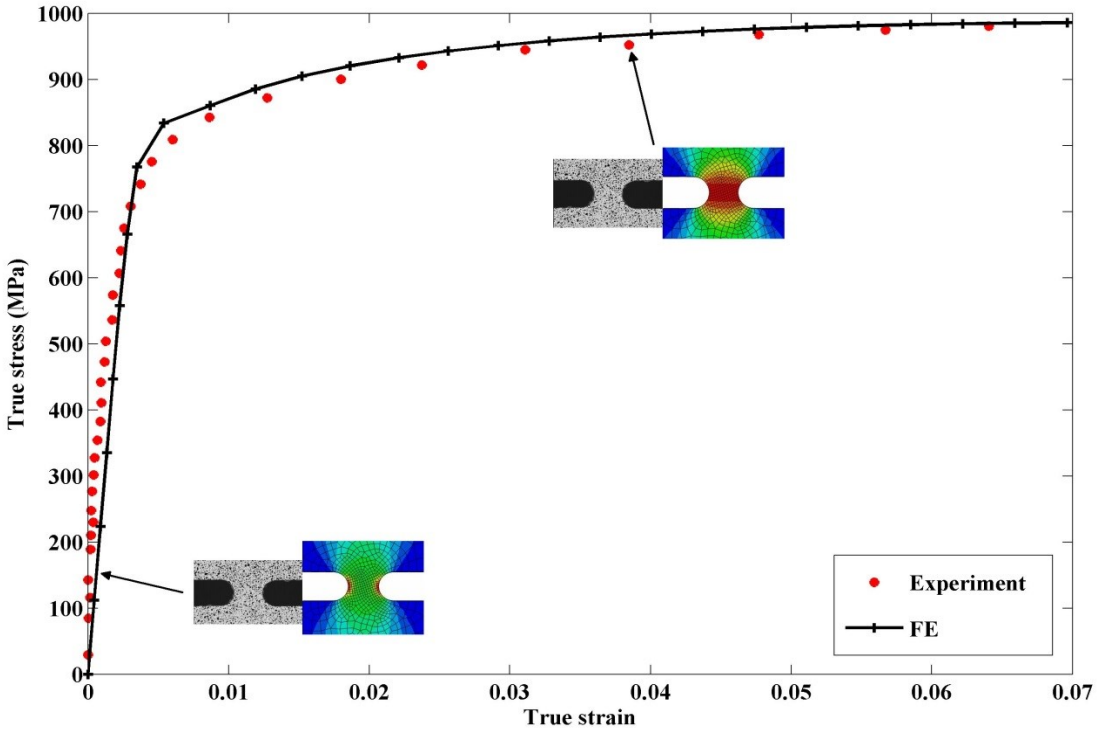
True stress (MPa)
True strain
Experiment
FE

(a) R2

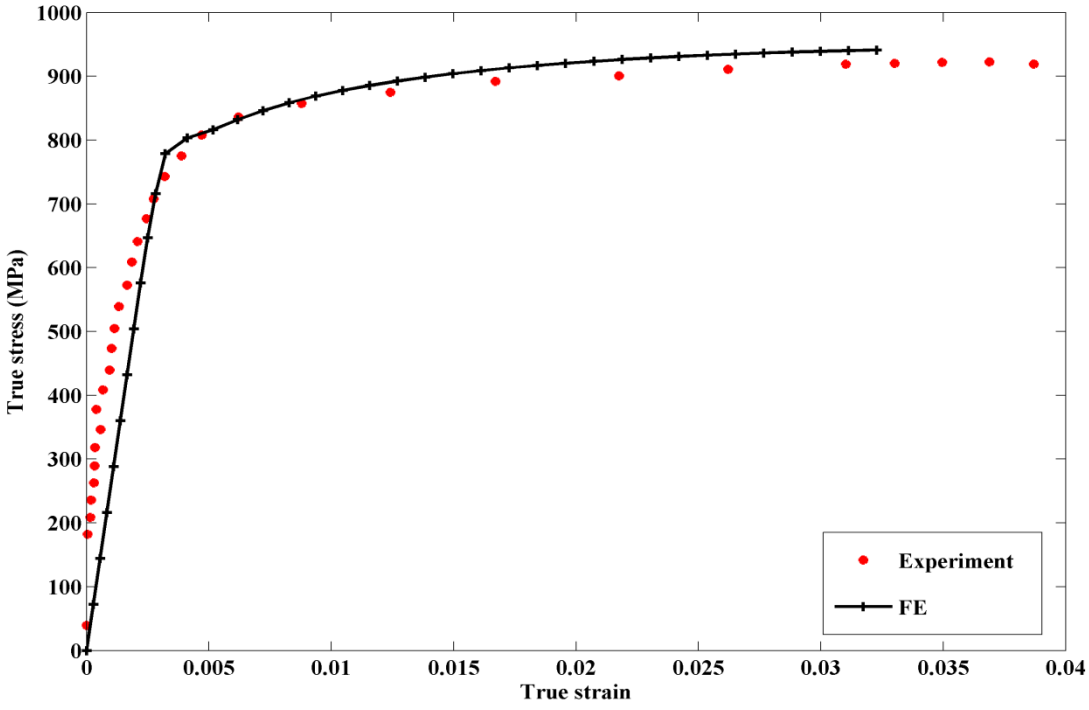
True stress (MPa)
True strain
Experiment
FE

(b) R4

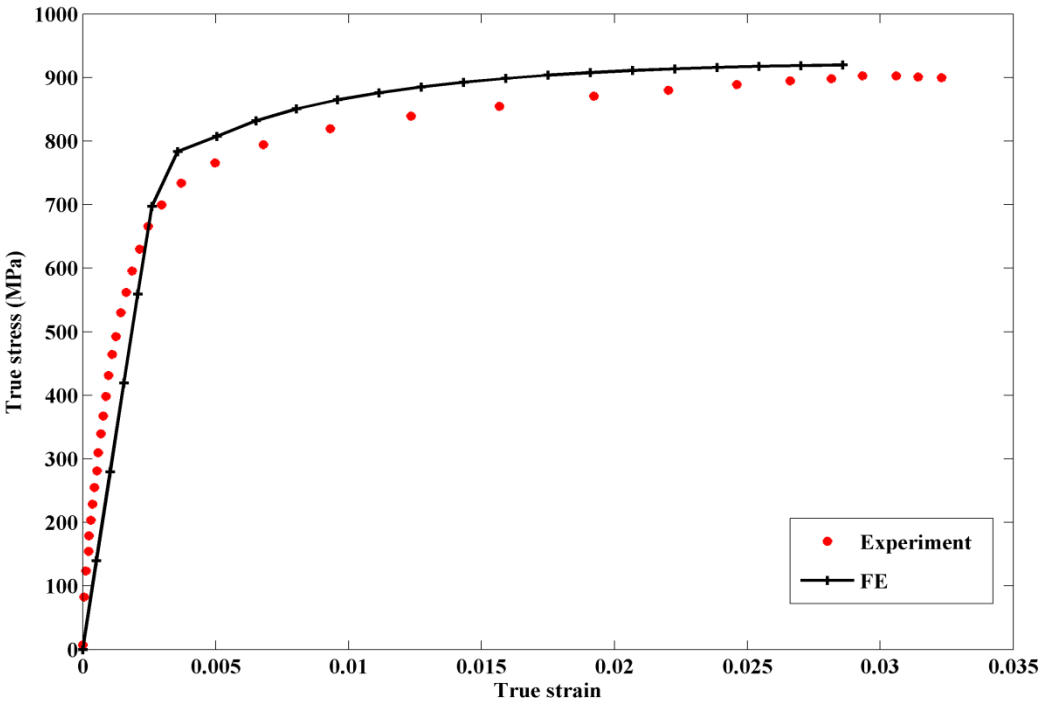

(c) R6

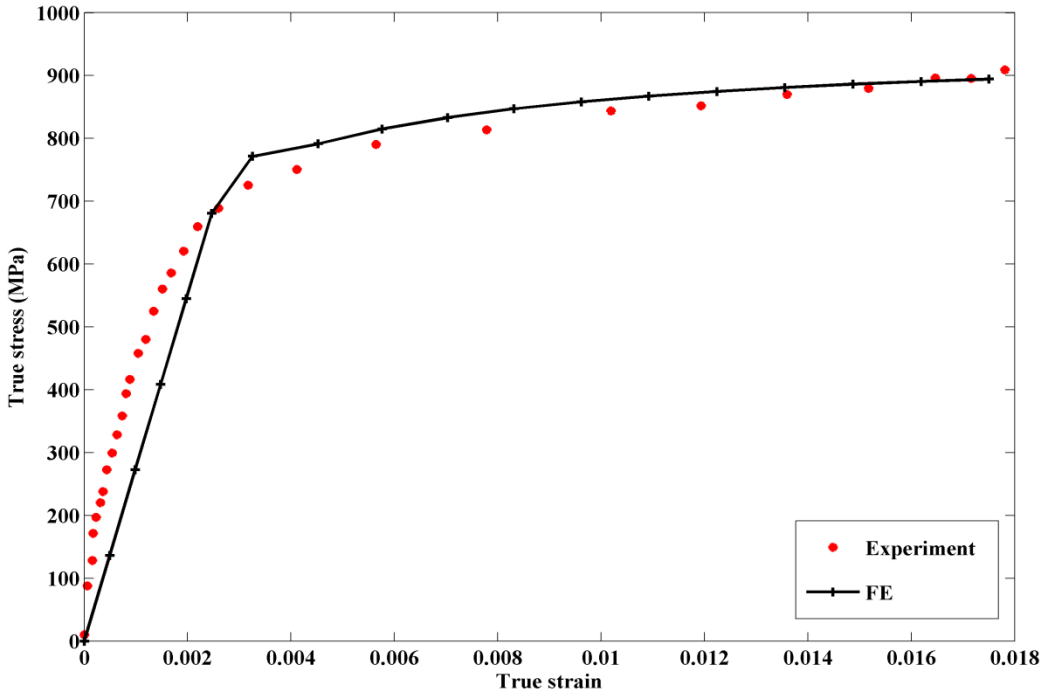

(d) R8

Fig. 4.1: Comparison between FE results and Experimental results (A80273)

Fig. 4.2 shows the results for steel samples A80274 R4, A80283 R4, A80284 R6 and R8. Larger percentage differences of stress-strain behavior are found between FE predictions and experimental results for steel samples A80283 and A80284. The comparisons of maximum forces for different steels samples are listed in Table 4.1. It clearly shows that the FE simulation predicts stronger material responses than experimental results. The largest percentage difference of maximum forces is found to be 9.56% for sample A80284 R2.

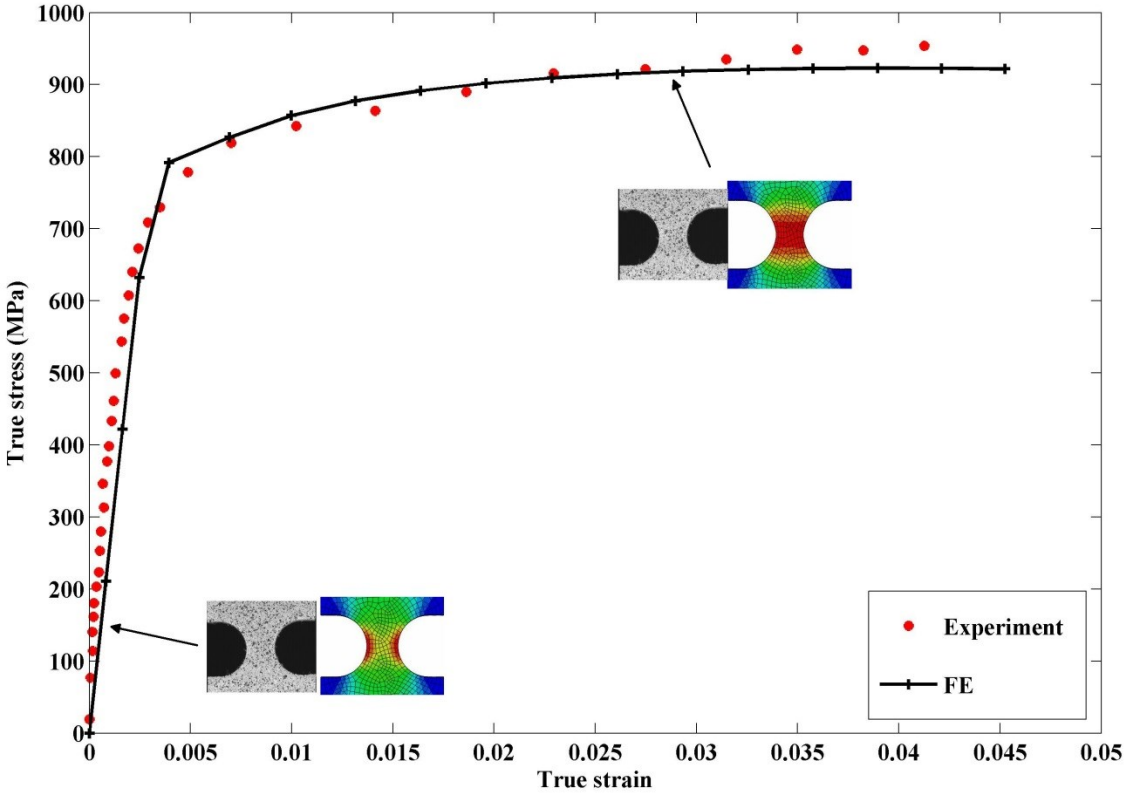

(a) A80274 R4

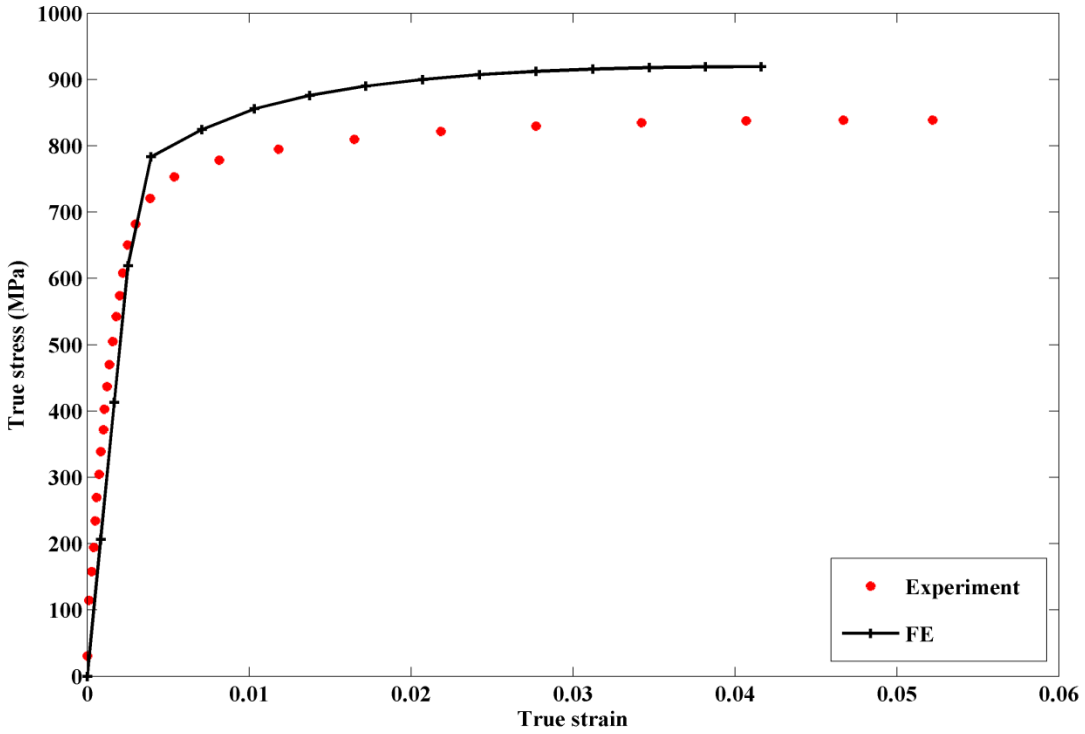

(b) A80283 R4

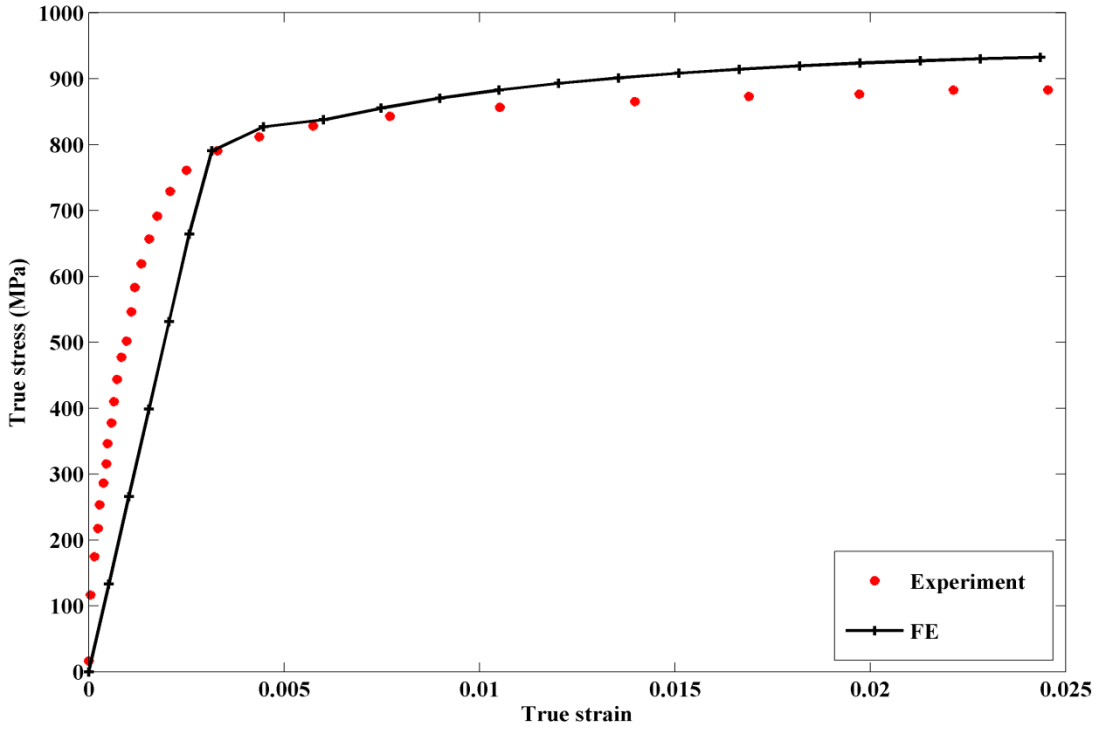

(c) A80284 R6

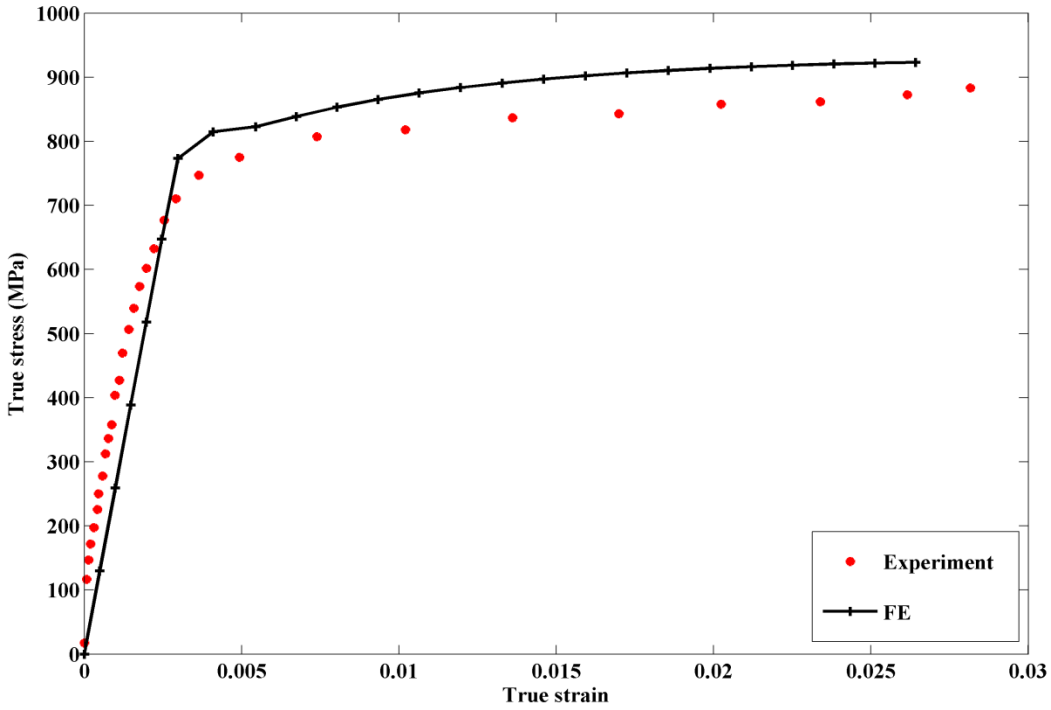

(d) A80284 R8

Fig. 4.2: Comparison between FE results and Experimental results for different steel sample

Table 4.1: FE and Experimental Results of Maximum forces for different steel samples

Steel samples		**Maximum Force (N)**		**% diff**
		FE	**Experiment**	
A80273	R2	12461.5	12205.3	2.08
	R4	11926.1	11580	2.94
	R6	11634	11423.3	1.8
	R8	11455.8	11431	0.22
A80274	R2	12187.7	12438.4	2.04

	R4	11637.7	11920.3	2.13
	R6	11365.4	11754.4	3.37
	R8	11175.8	11870	6.02
A80283	R2	12150.2	11237	7.81
	R4	11551.9	10572.1	8.6
	R6	11325.2	10403.5	8.5
	R8	11139.1	10572.5	5.22
A80284	R2	12715.1	11554.9	9.56
	R4	12149.6	11061	9.38
	R6	11852.3	11081	6.73
	R8	11657.6	11031	5.52

4.3. Possible Error Sources

As shown in Fig. 4.2 and Table 4.1, relatively large differences were found for HRSF steel samples A80283 and A80284. Several possible error sources were proposed. As shown in Table 4.2, hardening modulus and hardening exponent were derived from experimental results. Averaged elastic properties of steel samples were shown in Table 4.2. All these data were approximated from experimental results. Stress-strain relations calculated by using both approximated data and original experimental data were shown in Fig. 4.3. The areas where maximum differences were found for samples A80273, A80274, A80283 and A80284 were highlighted. Differences occurred at yielding and the beginning of plastic deformation. As the

plastic increases, the differences between two curves decrease. The stress-strain behavior predicted by using averaged material properties exhibits softer response than that calculated by using original experimental data. The maximum percentage differences for samples A80273, A80274, A80283 and A80284 were 7.74%, 9.72%, 7.54%, and 15.13%, respectively. These values were also listed in Table 4.3.

Other possible error sources include:

- Only a few samples were tested for each kind of HRSF steels, it may not provide a general material response
- Testing environment (temperature, humidity, etc.)
- Post-processing of experimental data
- DIC technique (preparations, analyzing process, etc.)
- Voids were not considered in FE simulation

Table 4.2: Averaged properties for steel samples from experiments (approximation)

HRSF Steels	**Yield Stress (MPa)**	**Young's Modulus (MPa)**	**Hardening Modulus (K')**	**Hardening Exponent (n)**	**Calculated Yield Strain**
A80273	722	194503	1122	0.0843	0.00371
A80274	712	190000	1100	0.0856	0.00375
A80283	705	186000	1085	0.0817	0.00379
A80284	763	185000	1180	0.095	0.00412

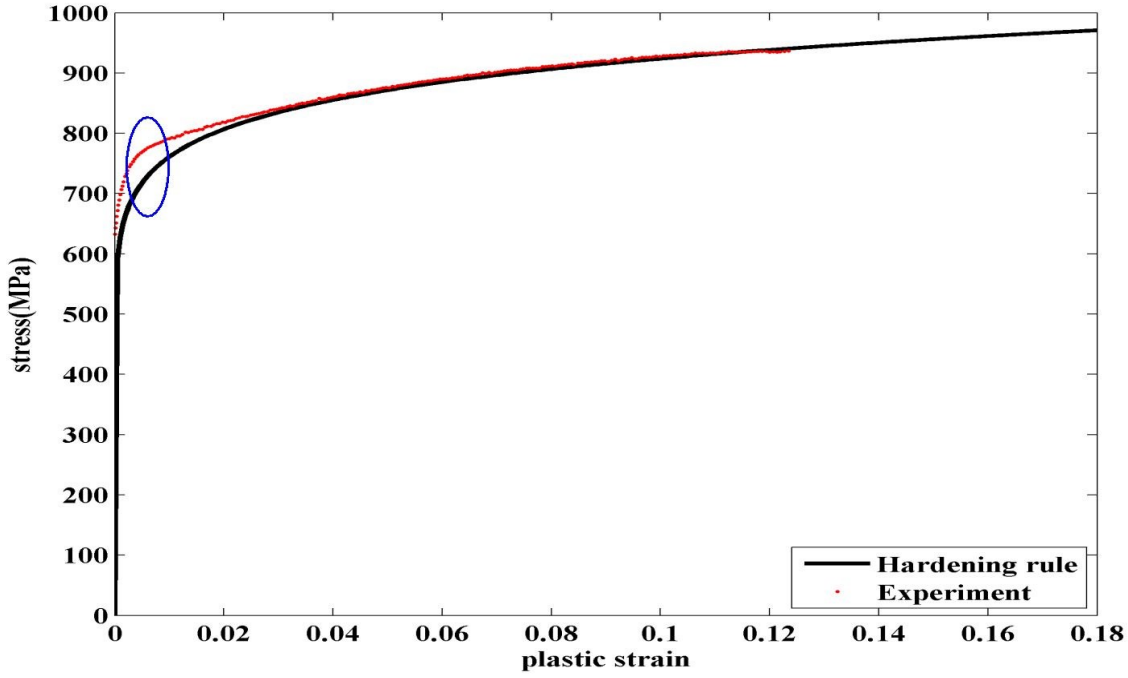

(a) A80273

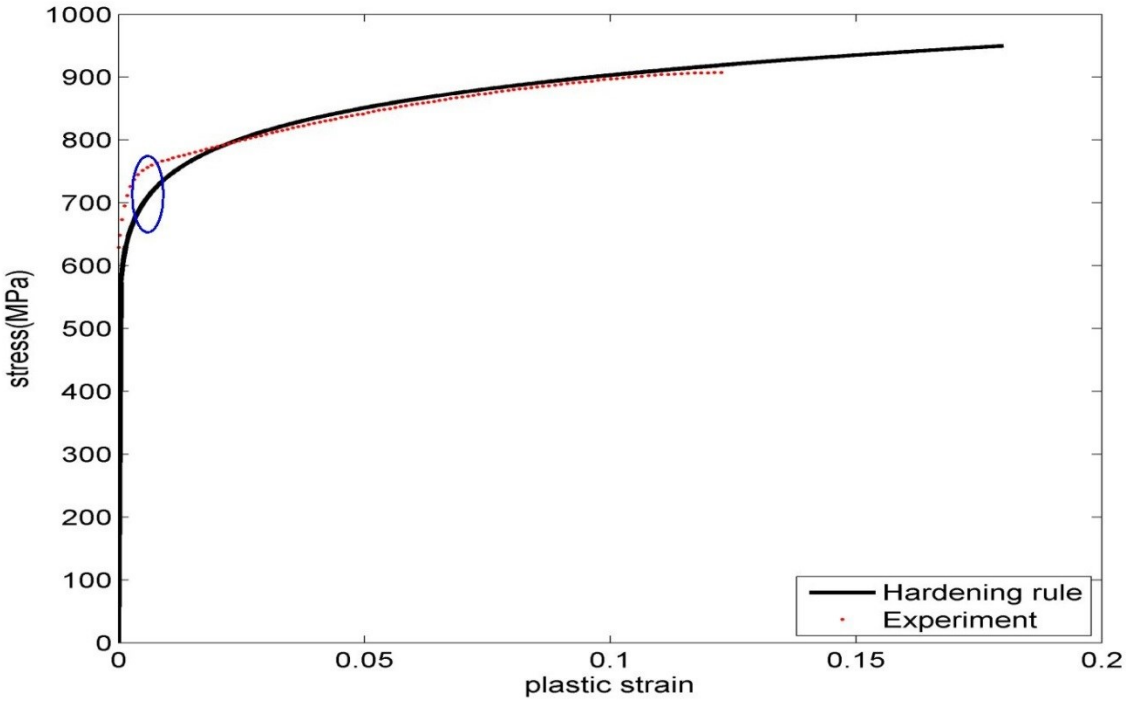

(b) A80274

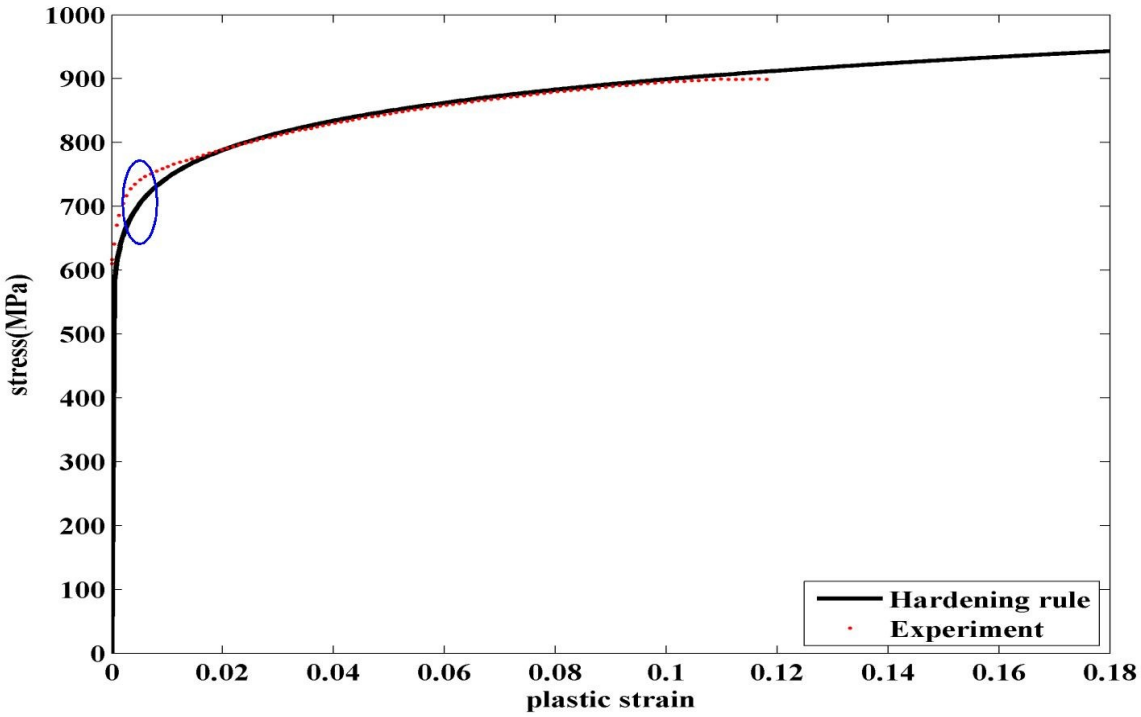

(c) A80283

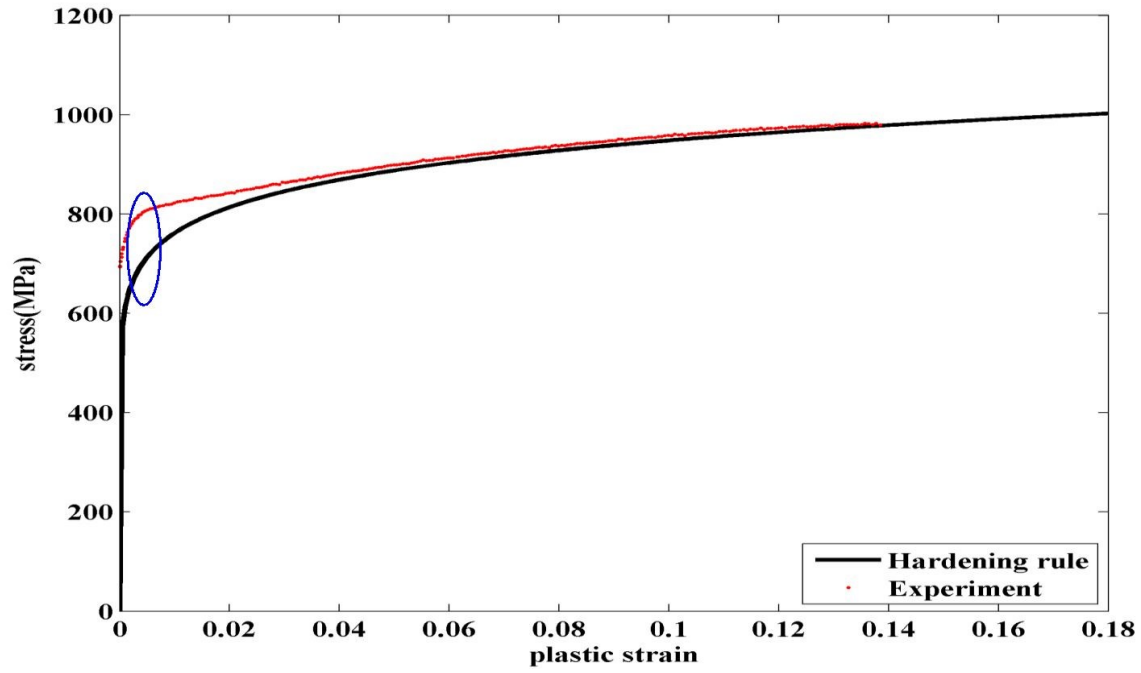

(d) A80284

Fig. 4.3: Stress-strain relations plotted by hardening rule method and experimental data

Table 4.3: Maximum difference of stress between experiments and hardening rule method

HRSF Steels	Experiment	Hardening Rule	% difference
	Stress (MPa)		
A80273	761.1	704.4	7.74
A80274	726	658.7	9.72
A80283	717.1	665	7.54
A80284	790.7	679.5	15.13

5. Micromechanical model for Hot Rolled Steels

5.1. Unit Cells

5.1.1. Two-dimensional Unit Cells

The common approach in the finite element analysis of the stress and strain behavior of particle-reinforced composite materials is based on describing the microstructure by a periodically repeating unit cell. The early studies in this area were limited to two-dimensional unit cells due to limited computational resources [37, 38]. Two-dimensional unit cells include plane stress and plane strain models and axisymmetric models. For plane stress and plane strain models, less computational time is required to simulate the material behavior of composites. But due to the shape of reinforcements and the boundary conditions imposed on the unit cell, some studies showed that inaccurate results of two phase materials might be obtained by using this two-dimensional plane stress and plane strain models [39-41]. Christman et al. [29] introduced the axisymmetric unit cell models of particle-reinforced metal matrix composites. The microstructure of composites was simulated as a network of hexagonal unit cells containing an ellipsoidal particle at the center of each unit cell. These hexagonal unit cells can be approximated by cylindrical unit cells to obtain an axisymmetric geometry. Llorca and Gonzalez [42] successfully used this model to investigate the mechanical properties and damage of metal matrix composites by particle failure. Two-dimensional models capture the anisotropy in deformation behavior induced by anisotropy in particle orientation. However, it is impossible to have a realistic comparison of these results to actual experimental results because of their 2D stress state [43].

5.1.2. Three-dimensional Unit Cells

Nowadays, the simulation work of three dimensional unit cells can be finished by personal computers [38, 41, 44-47]. The mechanical behavior of composites containing aligned, non-aligned or randomly distributed discontinuous reinforcements has been studied by using many different finite element models [48, 49]. The tensile behavior of a metal matrix composite reinforced with aligned short fibers was investigated by Hom [47] through the method of single particle unit cell. Only little effect of a cubic array with modest volume fractions of rigid spherical particles was found on the strength of a perfectly plastic matrix by Hom and McMeeking [48] through a single particle unit cell model. Recently, the study of periodic unit cells focuses on the multi-particle model with randomly distributed reinforcements [49]. Several strategies have been reported in the literature for building matrix-inclusion micro-geometries with random dispersion of inclusions, such as methods based on Monte Carlo methods [50], and on the random sequential adsorption algorithm (RSA) [51-54]. RSA algorithms sequentially add particles to a volume. The candidate particle will be generated randomly and accepted if it meets the requirements, otherwise, it will be rejected and a new candidate particle will be generated. The elasto-plastic behavior of metal matrix composites reinforced by short fibers of spheroidal or cylindrical shapes with an aspect ratio of 5 was investigated by Bohm et al. [41] via the method of multi-inclusion unit cell models. For low and medium volume fractions (< 30%), it is easier to arrange all particles perfectly. As the particle volume fraction increases, there is a tendency to show the geometrical frustration [41]. In order to increase the particle volume fraction, either the larger or more smaller particles need to be used. It would be harder to accommodate these particles. The RSA algorithm was modified by Segurado et al. [55] to be feasible for particle volume fractions of up to 50%, and they investigated the elastic properties of particle-reinforced

composites with three different types of materials. Only a very small scatter was found between estimates with a few dozen spheres in the unit cell and the average values of elastic constants by Gusev [56]. The elastic constants were obtained from the simulation of varying numbers of spheres in the unit cell. Suh et al. [57] proposed an enhanced continuum model for the size-dependent strengthening and failure of particle reinforced metal matrix composites. They further demonstrated that smaller particles lead to larger strengthening, and larger size effects were found for larger volume fractions. Pierard et al. [58] investigated the effective mechanical behavior of particle-reinforced metal matrix composites by using multi-particle unit cell model with a random distribution of elastic ellipsoids and analytical homogenization methods.

The results of the analytical homogenization models were used as benchmark to assess the accuracy of unit cell models. In the present work, multi-particle unit cells were used to evaluate the stress-strain behavior of the notched hot rolled flangeable steel samples. For completeness, the 3D multi-particle unit cell models were built and the general results were discussed first, followed by the applications in the HR steels.

5.2. Three-dimensional Multi-particle Unit Cell

Only a very small scatter was found between estimates with a few dozen spheres in the unit cell, and the average values of elastic constants, which were obtained from the simulation of varying numbers of spheres in the unit cell, as reported in [56]. These results were very close to the

exact solution. In the present thesis work, this approach was used to find the stress-strain relations for the HR steels.

5.2.1. 3D Multi-particle Unit Cell Model

Several methods have been proposed and reported in the literature for building matrix-inclusion micro-geometries with random distribution of particulate inclusions, such as methods based on Monte Carlo methods [59], and on the RSA algorithm [60-63]. The basic theory of RSA algorithm is that particles are added sequentially until a desired volume fraction is achieved. This algorithm is applied in this work. The general idea of RSA in this investigation is that the candidate particle will be accepted if it does not overlap any previously accepted particles; otherwise, it will be rejected and a new candidate particle will be generated until all particles are distributed perfectly. For unit cells with low to medium volume fractions of inclusions ($\leq 25\%$), it is easier to arrange all particles; but when the volume fraction of inclusions increases, it becomes more and more difficult to arrange all particles perfectly. Bohm's [48] demonstrated that as the volume fraction of particles increased, there was a tendency to show the geometrical frustration. Therefore, this RSA algorithm can only be applied if the particle volume fraction is less than or equal to 30%. If the particle volume fraction is larger than 30%, it is almost impossible to assign all particles perfectly in the unit cell by using standard RSA algorithm. In the present work, 15 non-overlapping identical spheres randomly distributed within the periodic cubic unit cell of volume L^3 were generated by using the standard Random Sequential Adsorption algorithm (RSA).

Obviously, the accuracy of results increases as more particles are distributed inside the unit cell. However, the computational resources increase dramatically with the increasing number of particles. As a compromise between computational resources and the accuracy of results, 15 particles were used in this work. In order to achieve better results, particles must be dispersed statistically isotropic within the unit cell, and the distribution of particles must also be suitable for finite element discretization. Since the volume fraction (f) of particles in the cubic unit cell is known and spherical particles are identical, thus, the radius (b) of particles can be obtained by using Equation (5.1).

$$n \times \frac{4}{3}\pi b^3 / L^3 = f \tag{5.1}$$

where L and n are the side length of the cubic unit cell and the number of particles, respectively.

In order to make sure that the candidate particle is acceptable, three conditions need to be fulfilled. The first condition is that the distances between the candidate particle and all the previously accepted particles must be larger than or equal to the minimum value. A minimum distance between particles needs to be set to make sure the finite element mesh is appropriate. In the present work, a value of 0.0094 times the side length of the unit cell which corresponds to 7% of the radius of the spherical particles ($2.07b$) was chosen to be this minimum distance [51, 64]. Other minimum distances ($2.056b$) can also be used and found in work of Bohm et al. [47, 48]. Secondly, if any intersection was found between surfaces of cubic unit cell and particles, because of the periodic microstructure of particle-reinforced composites, the distances between the corresponding particles and the particles near the opposite surfaces of intersected surfaces need to be checked as well. Finally, the distance between each particle and surfaces of cubic unit

cell is also critical to build a good finite element model. This distance cannot be so small in order to improve the quality of mesh. In the present work, the minimum distance is set to be $0.1b$.

Since the idea of unit cell approach is based on a periodic microstructure, special care needs to be taken for particles which intersect the surfaces of unit cell. The common is to split corresponding particles into appropriate number of parts, and copy these parts to the opposite surfaces of the unit cell. In this way, the periodicity of the unit cell is ensured. The number of parts need to be split can be obtained by using Equation (5.2).

$$g = 2^k - 1, k = 1,2,3 \tag{5.2}$$

In which k refers to the number of surfaces of the unit cell which are intersected by the particle. g refers to the number of particles need to be added. For example, if the particle intersects three surfaces of the unit cell, seven additional particles (g = 7) need to be added to opposite surfaces of the unit cell.

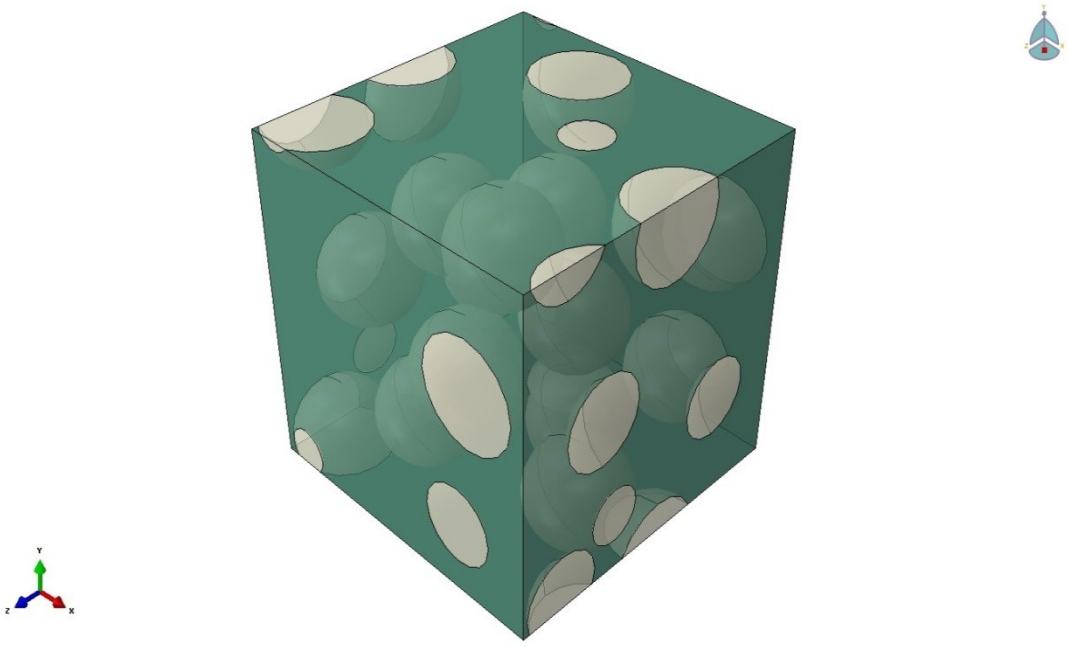

(a) Transparent sketch

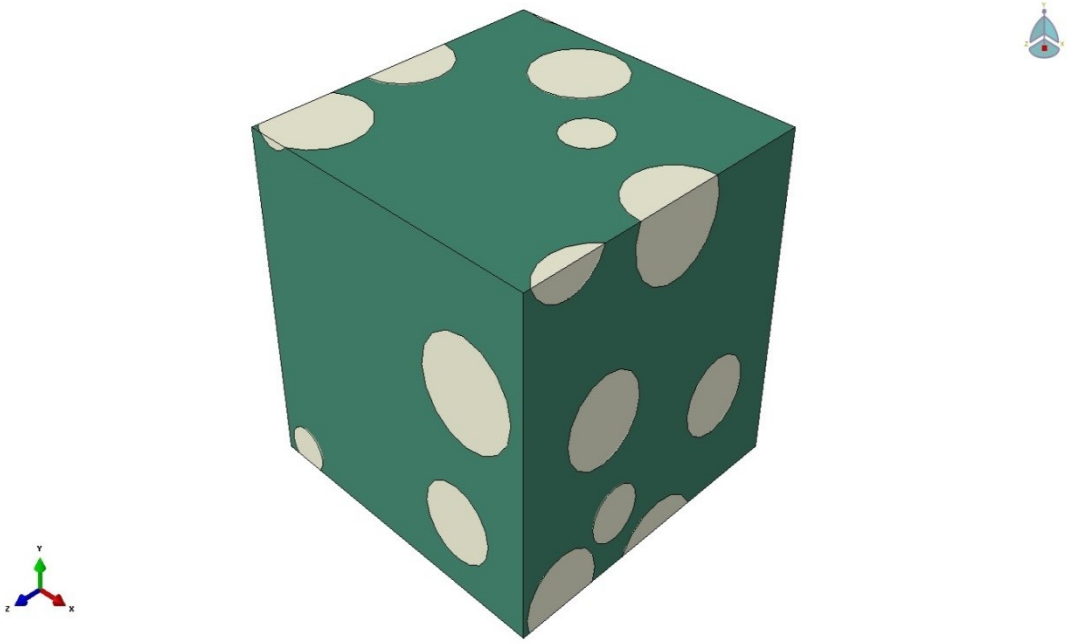

(b) Solid sketch (The light areas are intersections of particles and surfaces)

Fig. 5.1: A cubic unit cell containing 15 identical spherical particles with a random dispersion. The particle volume fraction is 25%

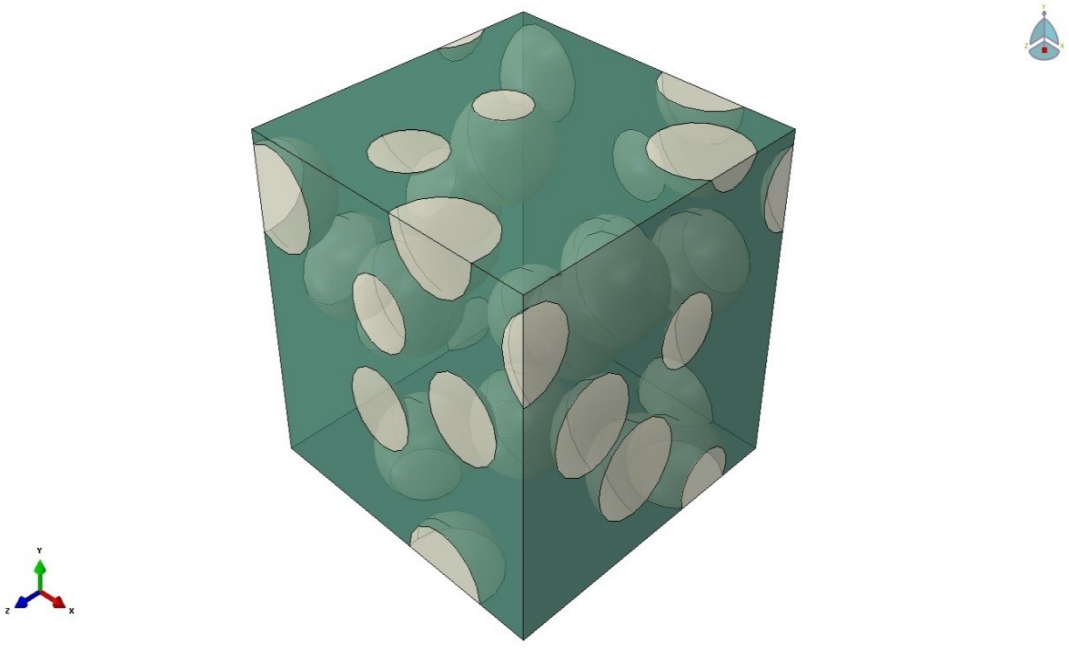

(a)

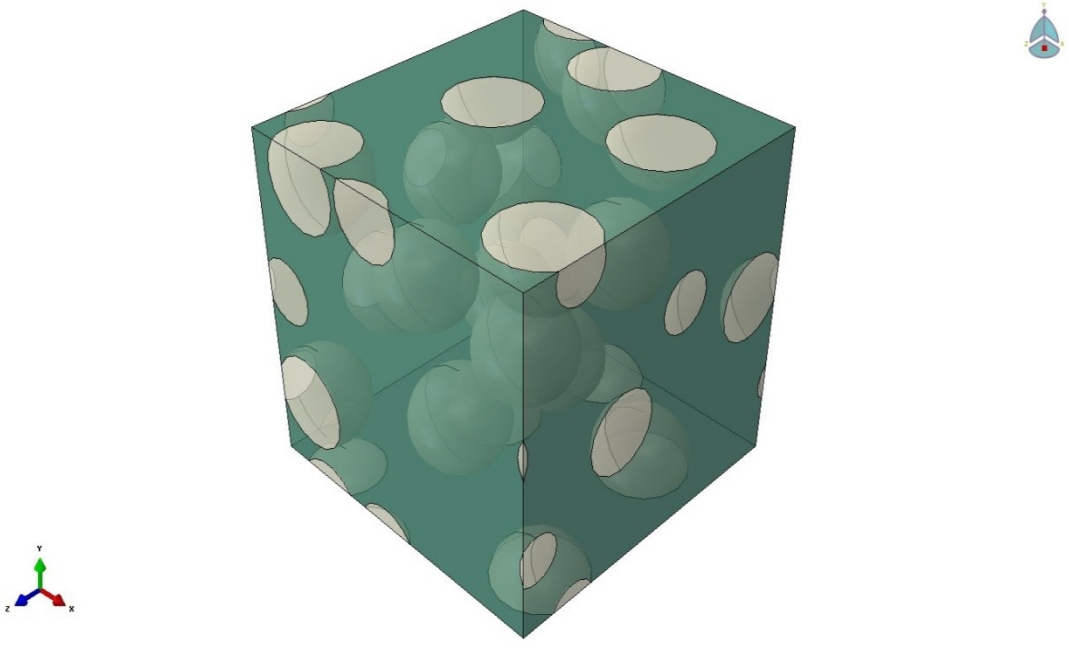

(b)

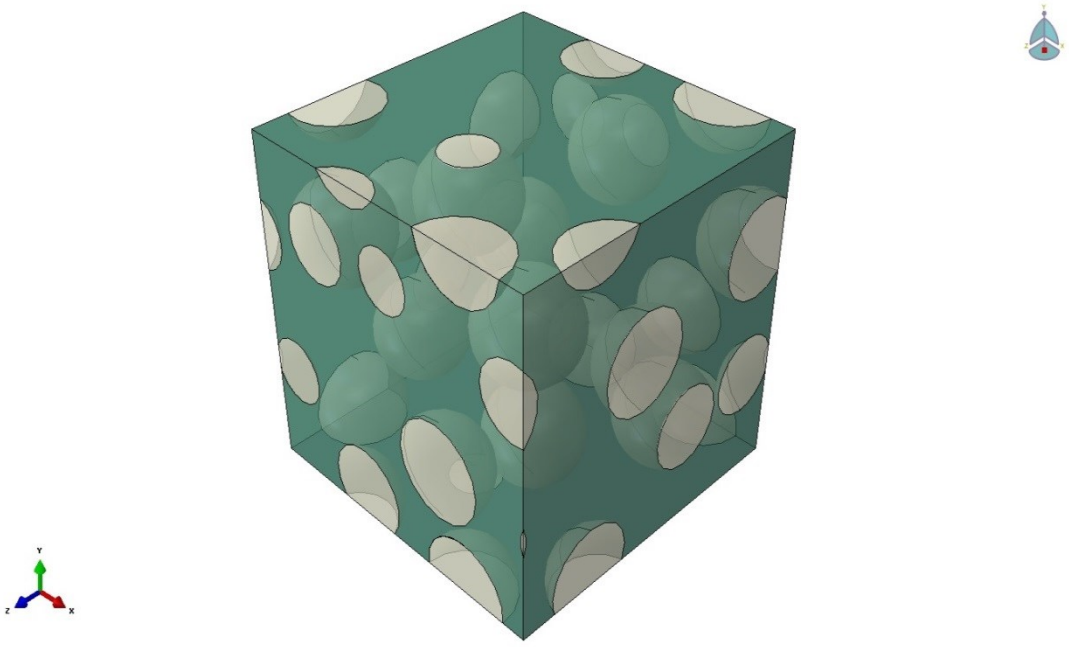

(c)

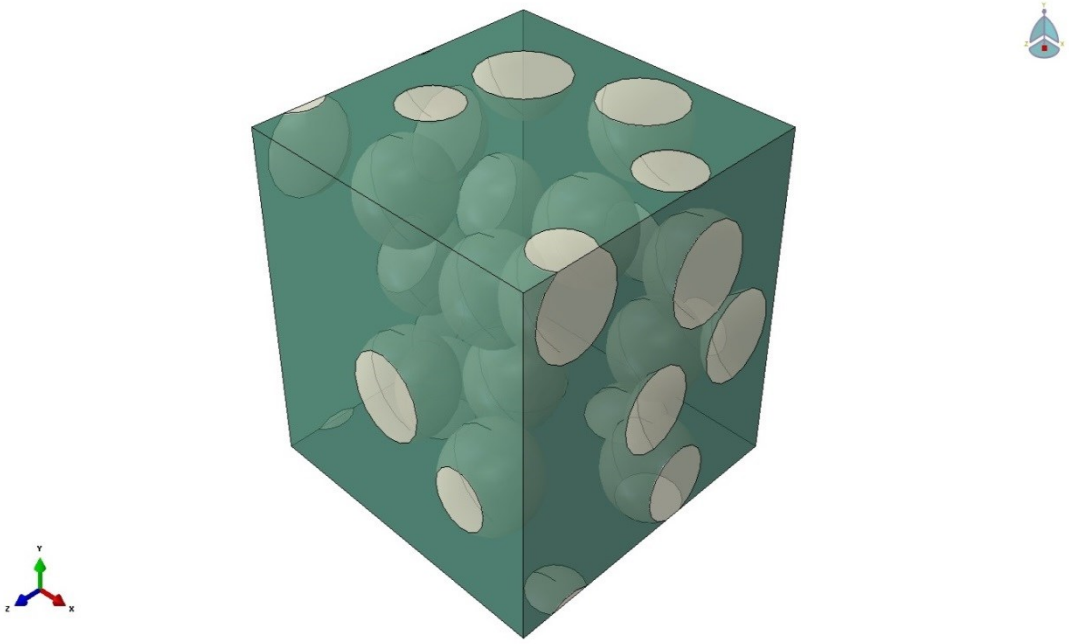

(d)

Fig. 5.2: Unit cells with four different spatial distributions of particles (20%)

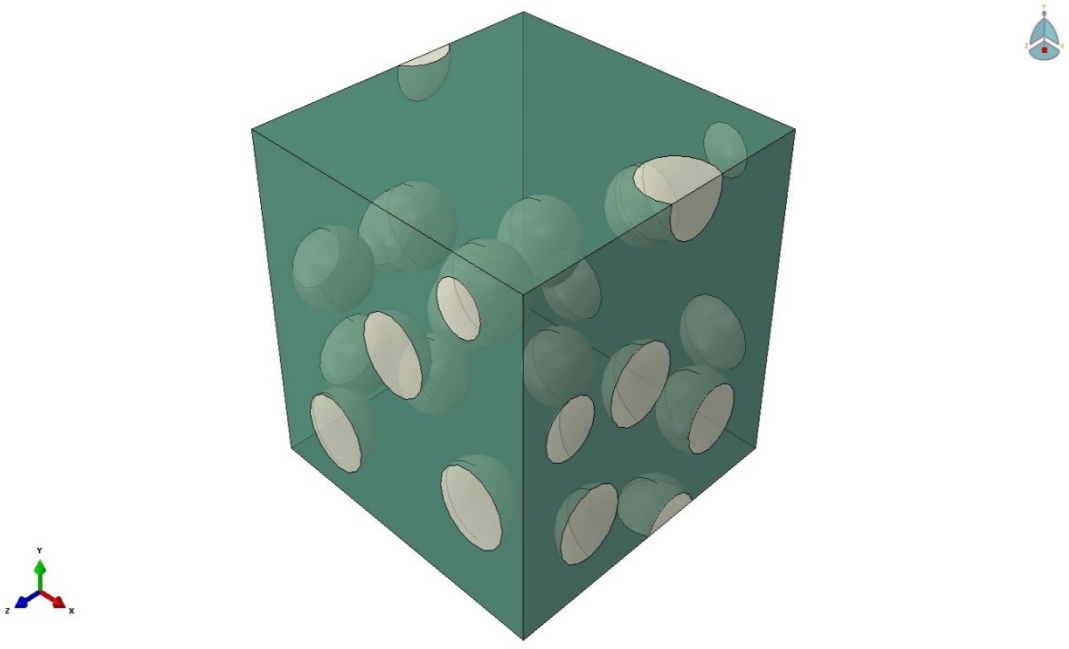

(a) 10%

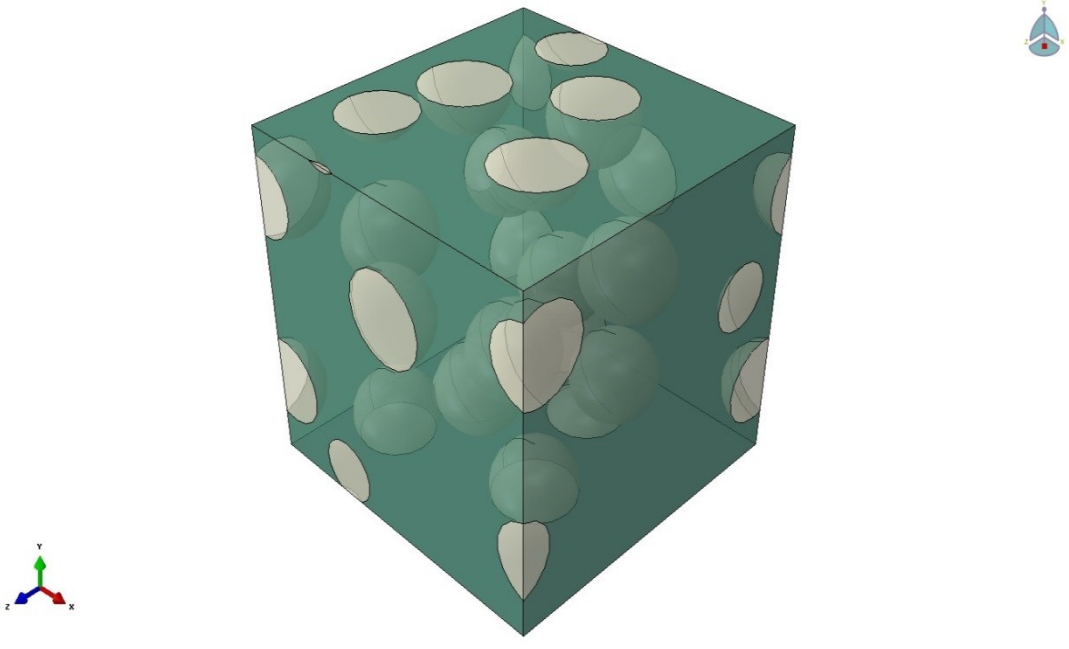

(b) 15%

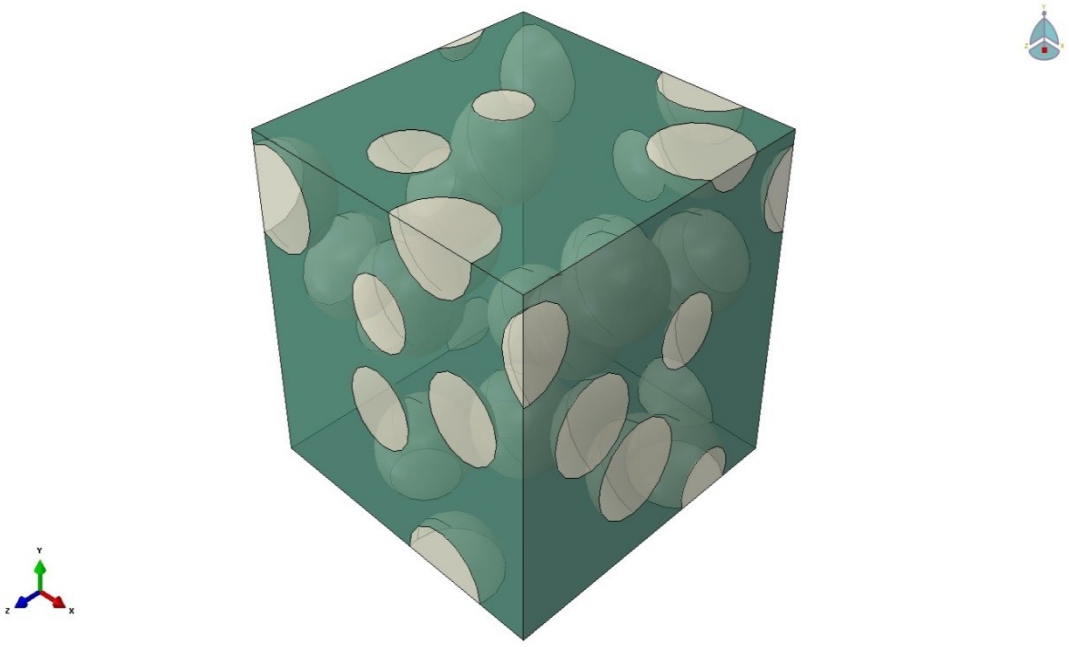

(c) 20%

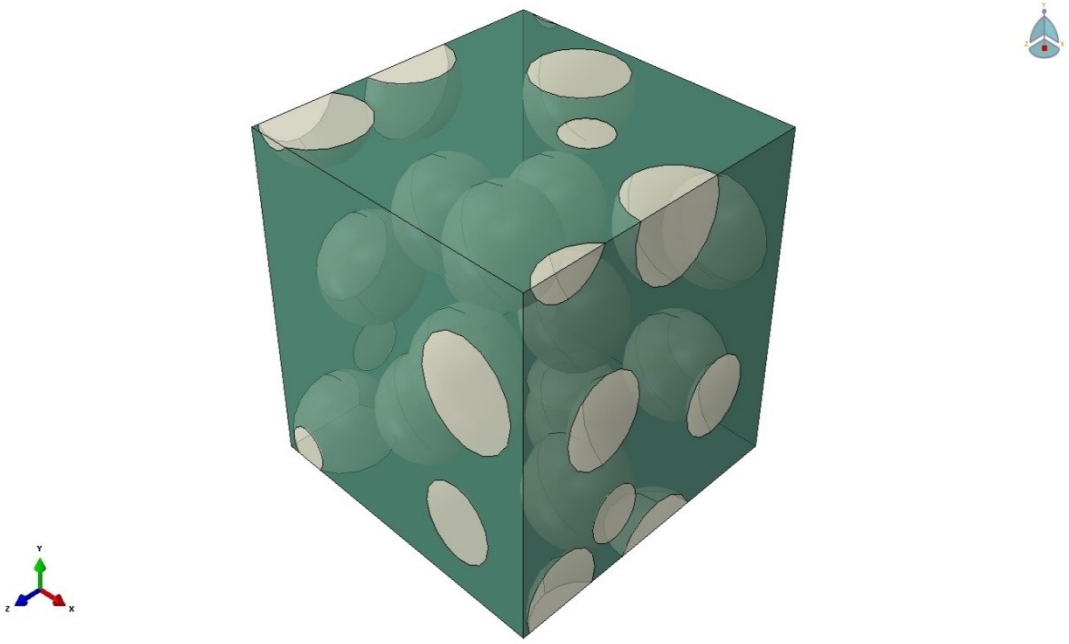

(d) 25%

Fig. 5.3: Unit cells containing 15 identical spherical particles with different volume fractions of particles

After applying all the model strategies discussed above, a completed unit cell with 15 particles is shown in Fig. 5.1. The distribution of particles can be observed in the transparent sketch which is Fig. 5.1 (a). The ratio of the length of the cubic unit cell and the diameter of particles is found to be 3.1556. For each particle volume fraction, four models with different particle spatial distributions are generated. Fig. 5.2 shows four different spatial distributions of particles for unit cells with 20% volume fraction of particles. Unit cells with 10%, 15%, 20% and 25% volume fractions of particles are shown in Fig. 5.3. Since the distribution of particles is random, it is very difficult to apply structured mesh. Instead, only free mesh with Tet shaped elements can be used. Modified 10-node tetrahedron elements (C3D10M) are used to avoid volume locking in fully yielded matrix regions [47, 51, 64]. Approximately 70,000 elements are used to mesh each unit cell model. For each model, mesh is verified to avoid or minimize the number of distorted elements. The meshed unit cell models with different volume fractions of particles are shown in Fig. 5.4. Fig. 5.5 (a) shows a finer meshed model which has 135,233 elements and 189,848 nodes is used to check the mesh dependency of unit cells with 10% volume fraction of reinforcements.

In the present work, *ABAQUS/Standard* [31] is used to complete the finite element simulation. Note that the spherical SiC particles are elastic and isotropic solids, while the metallic matrix (Aluminum) is an isotropic elasto-plastic solid. The J_2-flow theory is used as plasticity model for the aluminum matrix. The matrix obeys the Ludwig hardening relation [66] of

$$\sigma = \sigma_y + K' p^n \tag{5.3}$$

Where p is the accumulated plastic strain, σ_y is the initial yield stress, and K' and n refer to hardening modulus and hardening exponent, respectively. The material parameters used are listed in Table 5.1, where E and ν are Young's modulus and Poisson's ratio, respectively. The overall stress-strain curves are compared with that obtained with the coarse mesh. As shown in Fig. 5.6 (a), the maximum percentage difference of equivalent stress is found to be 0.42%. Similarly, the mesh dependency of unit cells with 25% volume fraction of reinforcements is analyzed by a finer meshed model which has 145,127 elements and 202,925 nodes as shown in Fig. 5.5 (b). The maximum percentage difference of equivalent stress is found to be 0.59%, which is shown in Fig. 5.6 (b). Therefore, standard mesh is good enough to provide good results.

Table 5.1: Material properties used for the aluminum matrix and ceramic particles

Material	E (GPa)	υ	$\boldsymbol{\sigma_y}$ (MPa)	$\boldsymbol{K'}$	n
Aluminum	75	0.3	75	416	0.39
Ceramic (SiC)	400	0.2	-	-	-

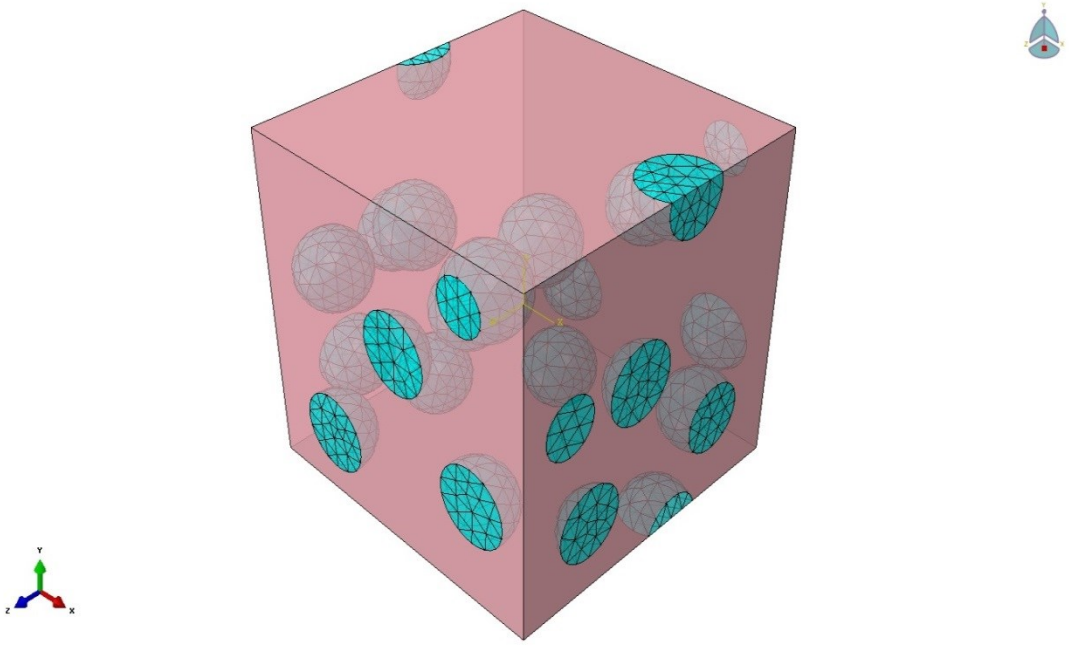

(a) 10% volume fraction of reinforcements

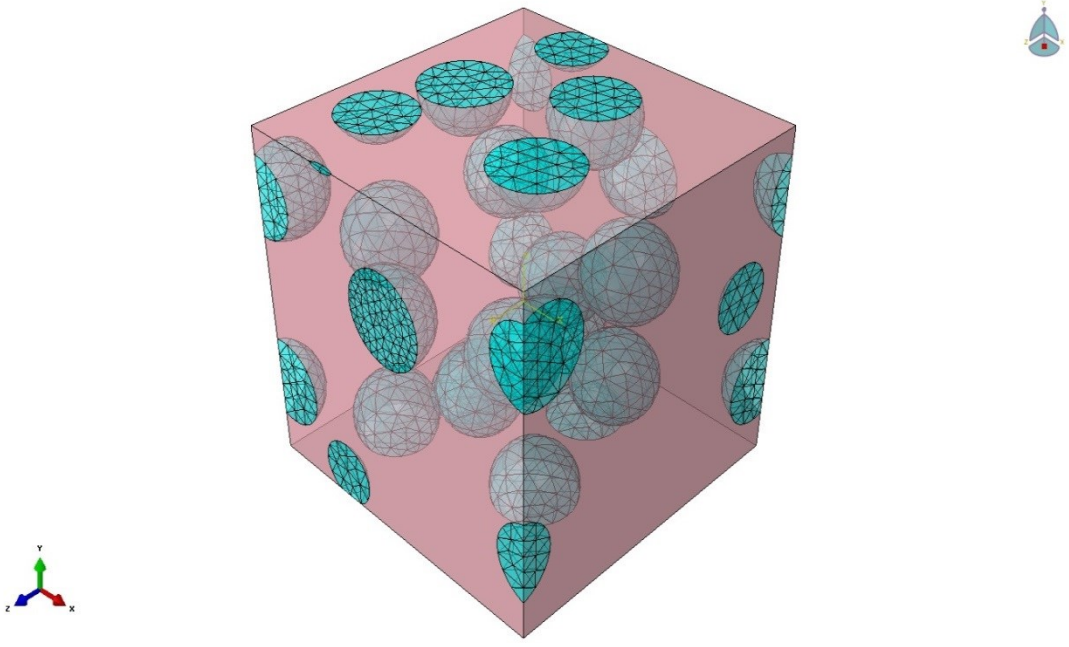

(b) 15% volume fraction of reinforcements

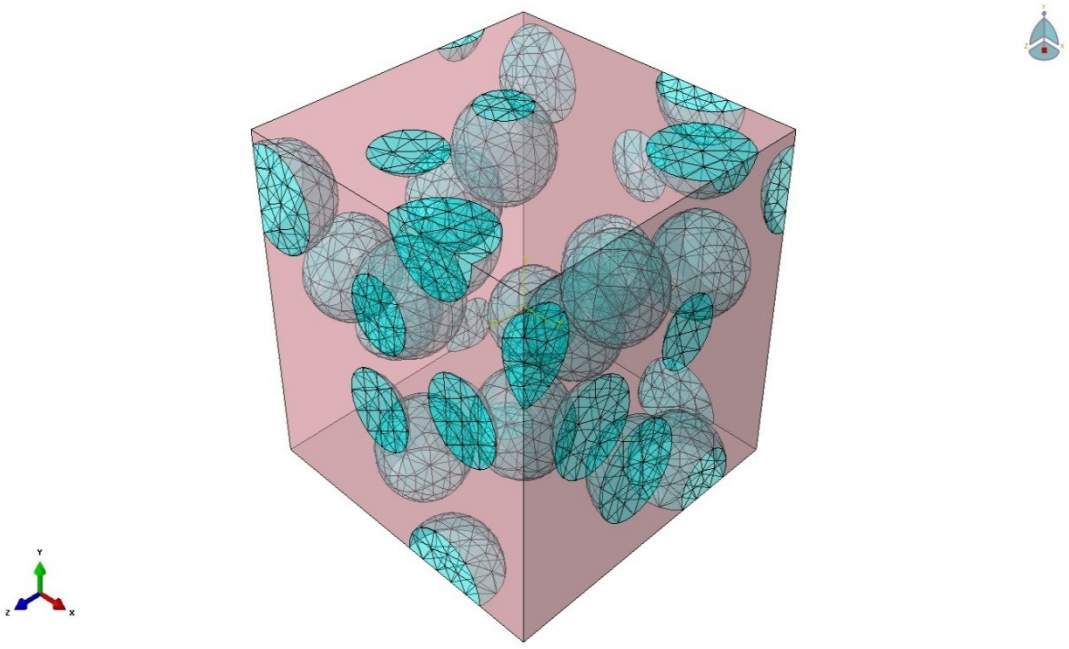

(c) 20% volume fraction of reinforcements

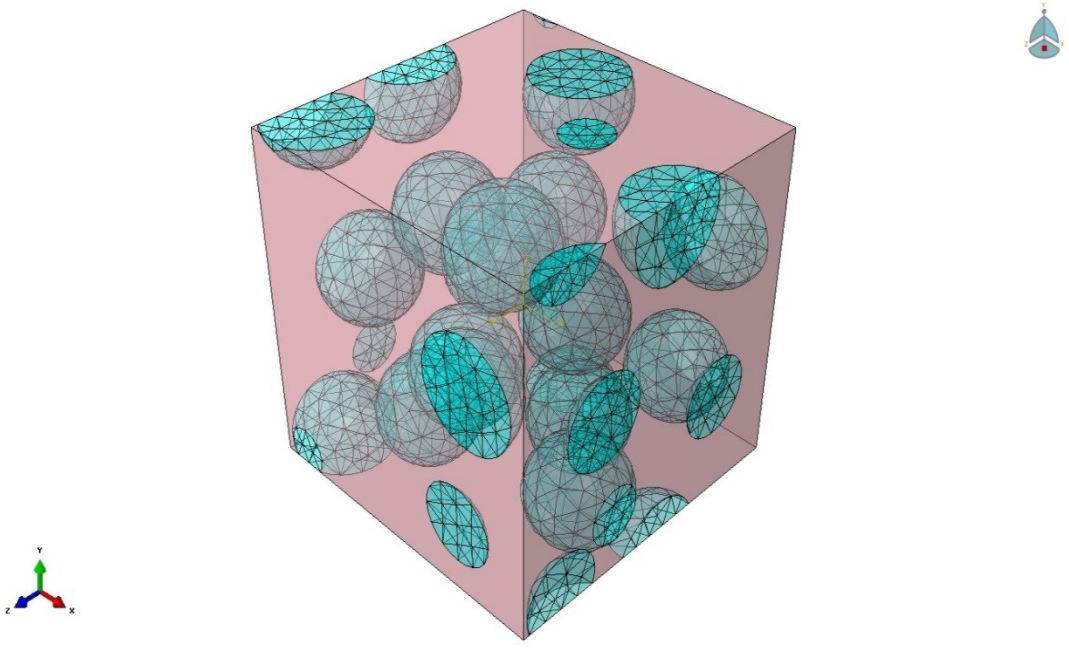

(d) 25% volume fraction of reinforcements

Fig. 5.4: Cubic unit cells with multiple meshed particles

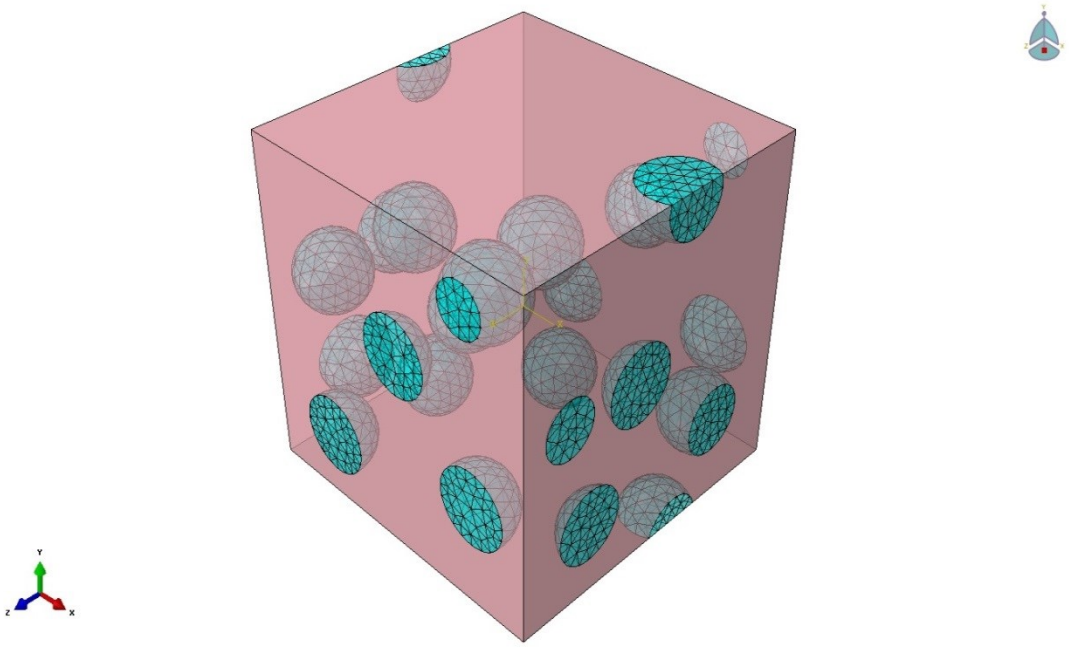

(a) 10% volume fraction of reinforcements

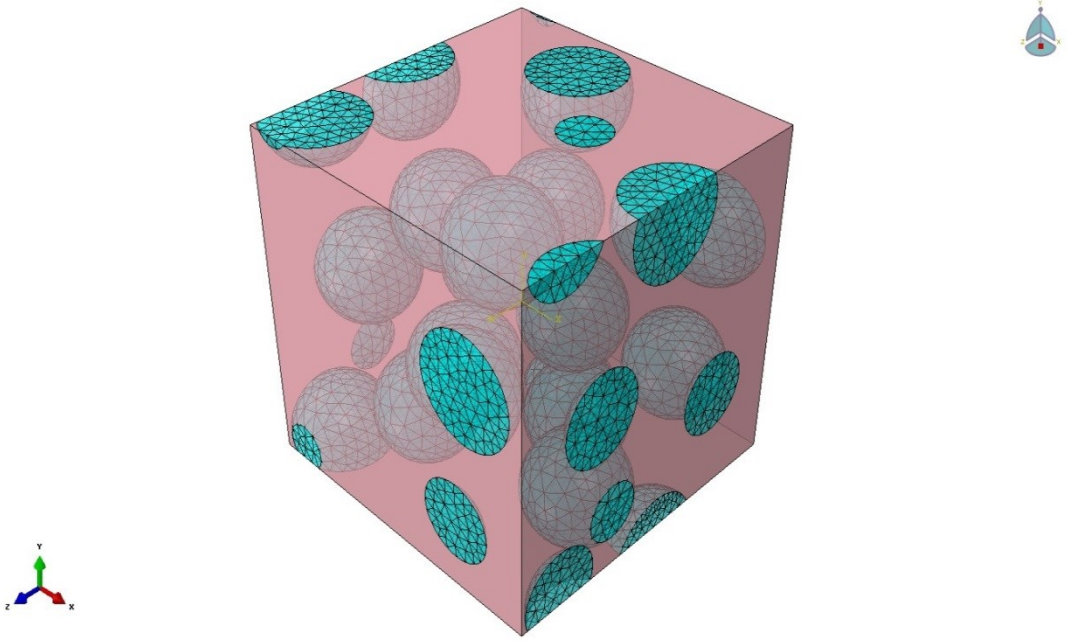

(b) 25% volume fraction of reinforcements

Fig. 5.5: Unit cell with finer meshed particles

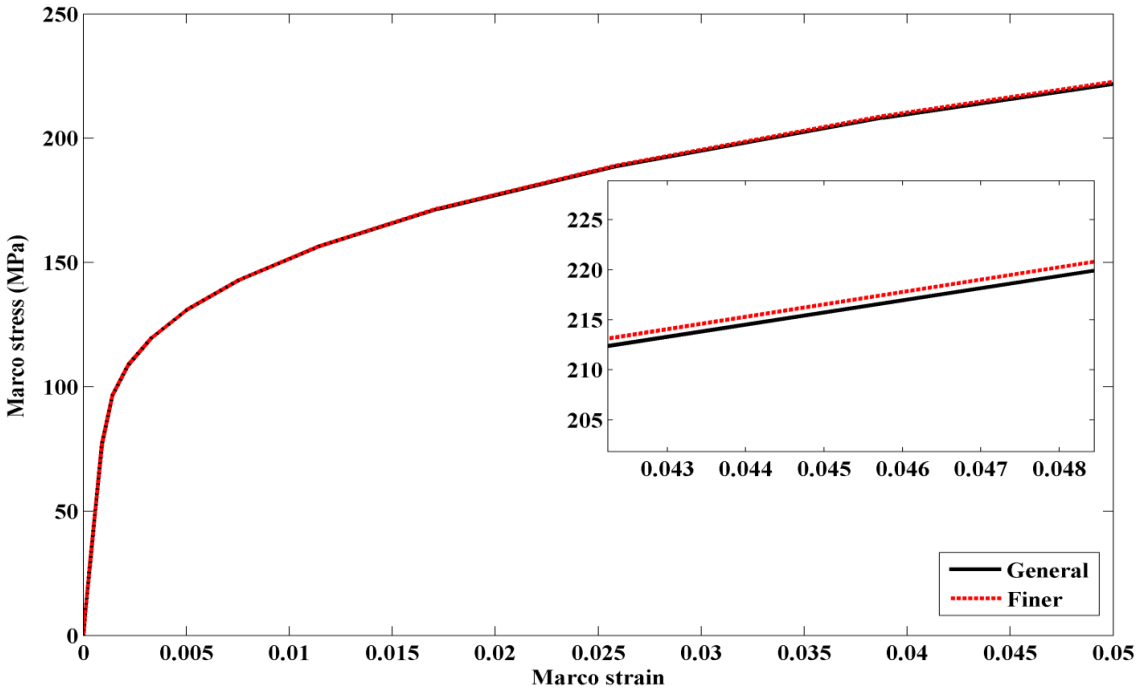

(a) 10% volume fraction of particles

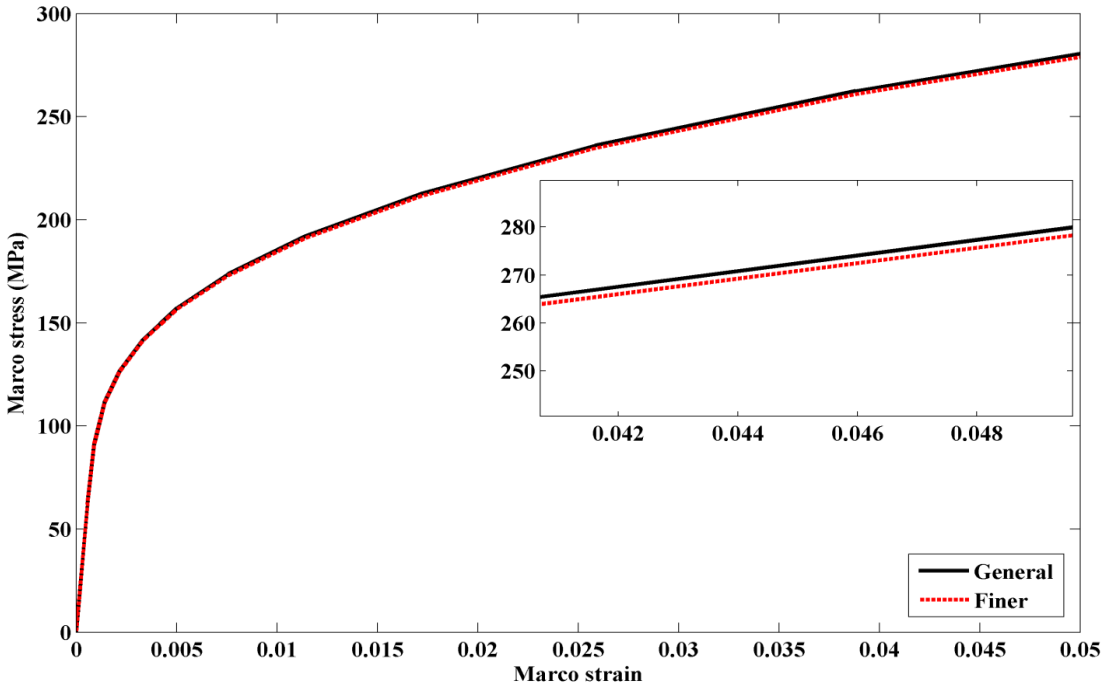

(b) 25% volume fraction of particles

Fig. 5.6: Analysis of mesh fineness

Simplified periodic boundary conditions are applied on the unit cell models. No gaps and overlaps are allowed between neighboring unit cells, as well as unphysical constraints on their deformation. This means that the cells must be geometrically compatible. Perfect bonding is assumed between the matrix and particles [67]. Thus, the continuity of displacement vectors at the interface between matrix and particles must be satisfied and can be expressed by Equation (5.4).

$$u_i^M = u_i^P, \; i = 1, 2, 3 \tag{5.4}$$

Where superscript *P* represents particle, *M* represents matrix and *u* is the displacement.

Like defined in Equation (5.4), the displacements of each pair of nodes on opposite surfaces of unit cell must behave the same, and these displacements can be controlled by using equation constraints. It shows that the effective composite behavior derived under these conditions is always bounded by those obtained under imposed forces or displacements [68, 69]. Full periodic boundary conditions for multi-particle unit cells are complicated and they can be found in [44, 68]. Many researchers worked on periodic boundary conditions, and they have reported in the literature [70-72]. Different kinds of boundary conditions for the representative volume element (RVE) have been studied and compared with periodic boundary conditions. The effect of mixed uniform boundary conditions on the predicted mechanical behavior of elastic and inelastic particle-reinforced composites was investigated by Pahr and Bohm [72]. Rodriguez [72] demonstrated that only small differences were found between the predictions obtained with periodic boundary conditions and mixed uniform boundary conditions.

Similarly, void, damage, and nucleation caused by particle cracking or de-bonding are not considered in this work. Thermal residual stresses are not considered. For all the simulations of the multi-particle unit cells, tensile loading is applied to the maximum far-field strain of five percent. The values of the macroscopic stress are calculated by dividing the sum of the reaction forces by the current area of the corresponding surfaces.

5.2.2. Validation of the 3D Multi-particle Unit Cell Models

5.2.2.1. Macroscopic Responses

This section is devoted to provide both macroscopic and microscopic responses of multi-particle unit cells. The macroscopic results were compared with the results of the analytical methods (tangent homogenization model coupled with the Mori-Tanaka method [73, 74]) and single particle unit cells.

In order to find out the influences of particle distribution on the stress-strain relations, four models with different particle distributions were generated and analyzed by the procedures described in section 5.2 for each particle volume fraction (10%, 15%, 20% and 25%).

The comparison of tensile stress-strain curves for multi-particle unit cell with different particle distributions are shown in Fig. 5.7. For the legends shown in figures, SP, MP, and MP10 are abbreviations of single particle unit cell, multi-particle unit cell, and multi-particle unit cell with 10% particle volume fraction, respectively. MP-10-5P stands for multi-particle unit cell with

10% particle volume fraction with five particles inside the unit cell. This nomenclature is used in the following figures in this chapter. The analytical method used in this study is a modified tangent-based method of homogenization [75, 76] which has been proved to have a good accuracy for particle-reinforced composites.

Results

Four stress-strain curves for unit cells with different particle volume fraction are shown in Fig. 5.7. The results of four stress-strain curves show a little scatter. The maximum percentage differences of macro stress between these four curves at a far-field strain of 5% are found to be 1.5%, 1.1%, 3.6% and 2.6% for 10%, 15%, 20% and 25% volume fraction of particles, respectively.

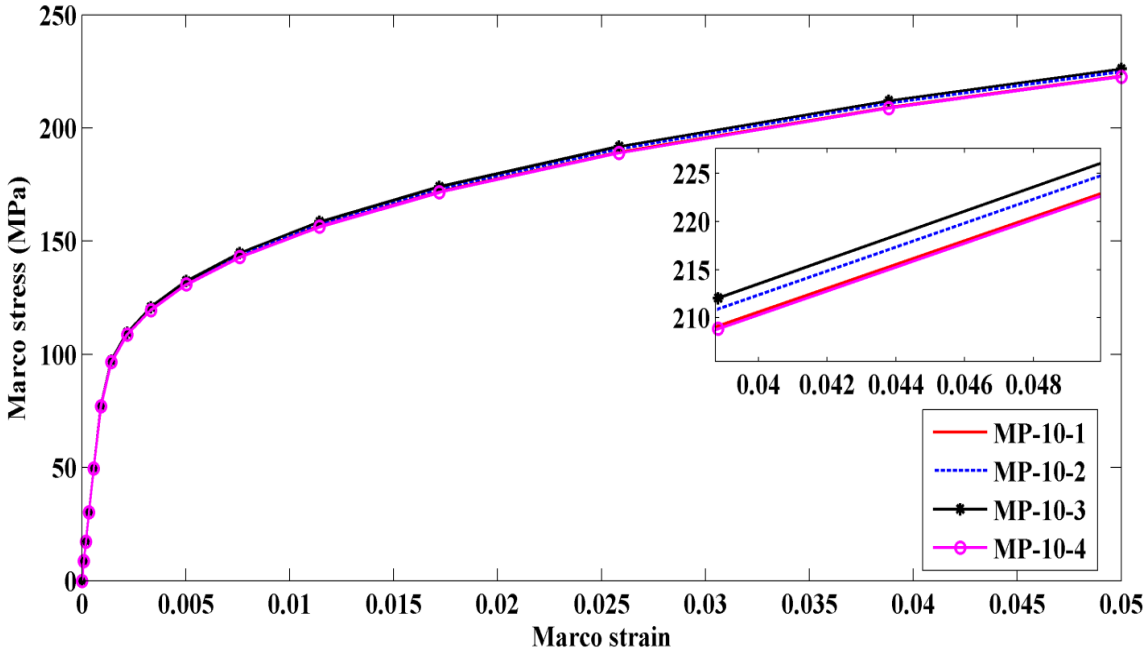

(a) 10%

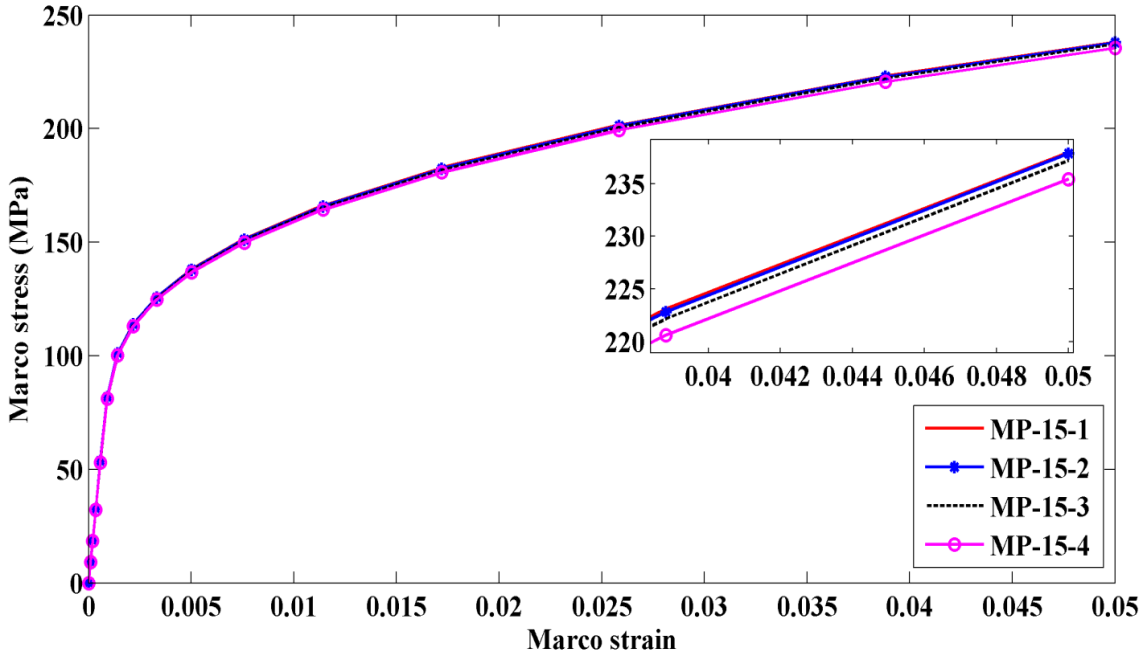
Marco stress (MPa)
Marco strain
MP-15-1
MP-15-2
MP-15-3
MP-15-4

(b) 15%

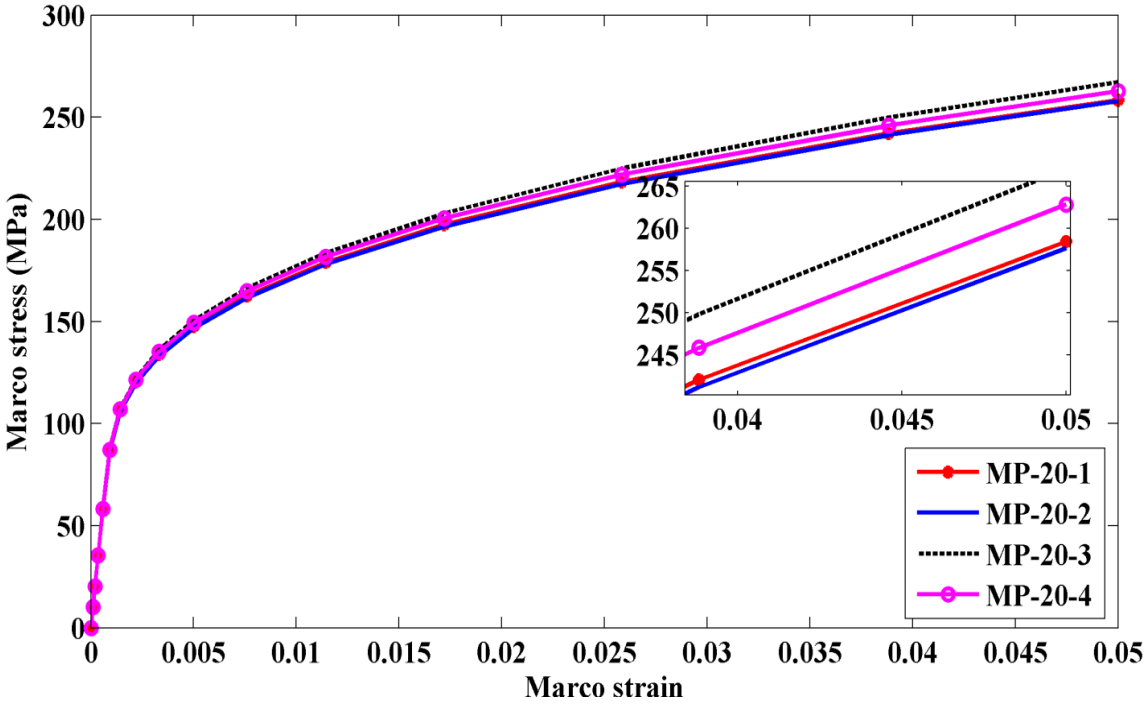
Marco stress (MPa)
Marco strain
MP-20-1
MP-20-2
MP-20-3
MP-20-4

(c) 20%

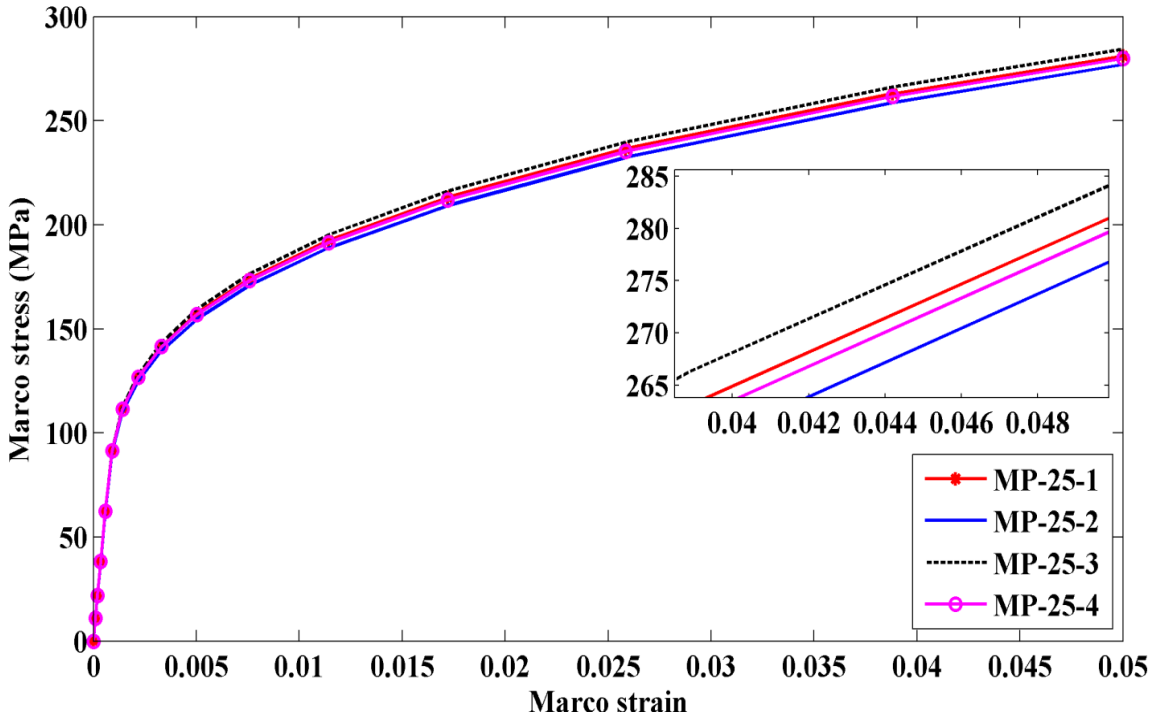

(d) 25%

Fig. 5.7: Tensile stress-strain curves with reinforcement volume fraction of (a) 10%, (b) 15%, (c) 20%, (d) 25%

The effects of particle volume fractions

An average curve is obtained by averaging all four stress-strain curves for each particle volume fraction. Since this average tensile stress-strain curve has taken the effect of particle distributions into account, it is more accurate and closer to the exact result. Therefore, this average can be considered as the general solution for MP unit cell with different spatial distributions of particles, and it can be validated by the analytical results. The average stress-strain curves for multi-particle unit cells are shown in Fig. 5.8 (a). As shown in Fig. 5.8 (a), MP unit cell with particle volume fraction of 10% exhibits the softest response, while unit cell with particle volume

fraction of 25% exhibits the strongest response. It shows that the stress increases as volume fraction of particles increases. It can be seen that the numerical results are superposed in the elastic regime and at the onset of plastic deformation. However, the matrix deformation becomes dominant as the strain increases. The elastic modulus increases as the volume fraction of particles increases, which lead to higher flow stress of composites. This increase in flow stress can be observed in the plastic regime. The maximum percentage difference of stress between 10% and 25% particle volume fractions is found to be 22.4% at the tensile strain of five percent. It can be concluded that the tensile strength of composites is significantly improved by a higher volume fraction of particles, in the case of low to medium volume fraction of reinforcements ($\leq$ 25%). These results are based on the averaged Cauchy stress values with respect to far-field strains. Similar results are found for single particle unit cells, the stress increases as volume fraction of particles increases. The maximum percentage difference of stress between 10% and 25% volume fractions of particles is found to be 24.1% at the tensile strain of five percent. The comparison of tensile stress-strain curves of single particle unit cells are shown in Fig. 5.8 (b). The same trends are found in the results of the analytical tangent-based model [77], as shown in Fig. 5.9. The maximum percentage difference of stress between 10% and 25% volume fractions of particles is found to be 19.7% at the tensile strain of five percent.

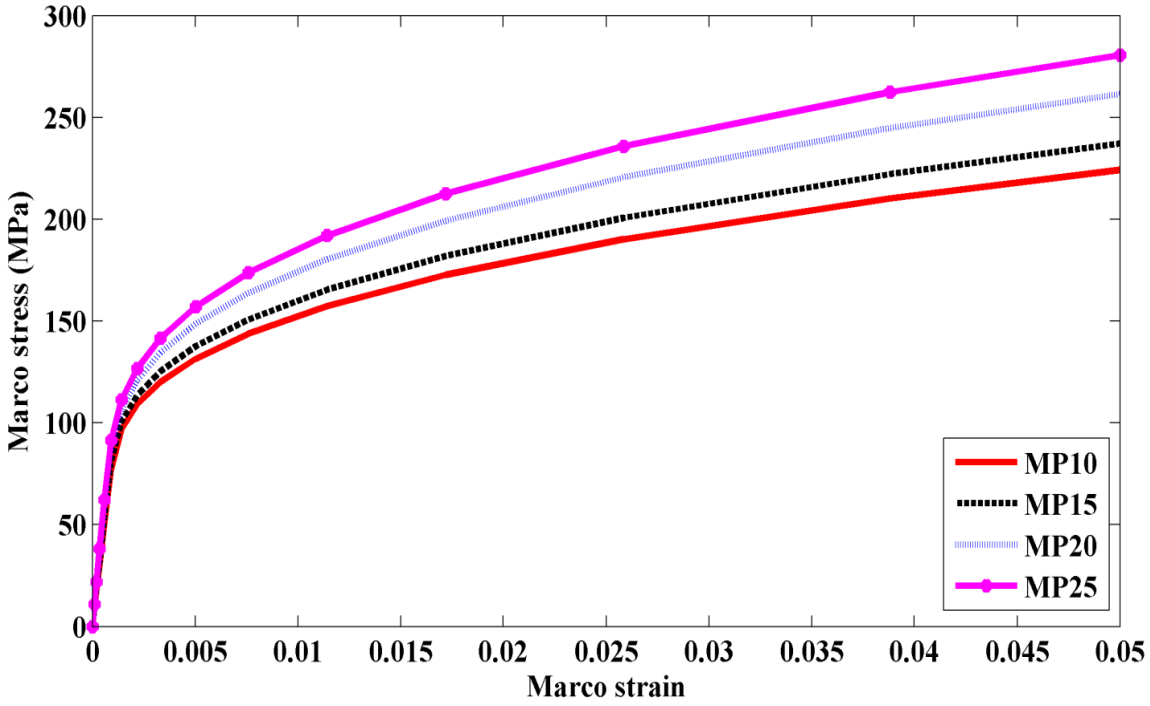

(a) Multi-particle Unit Cell

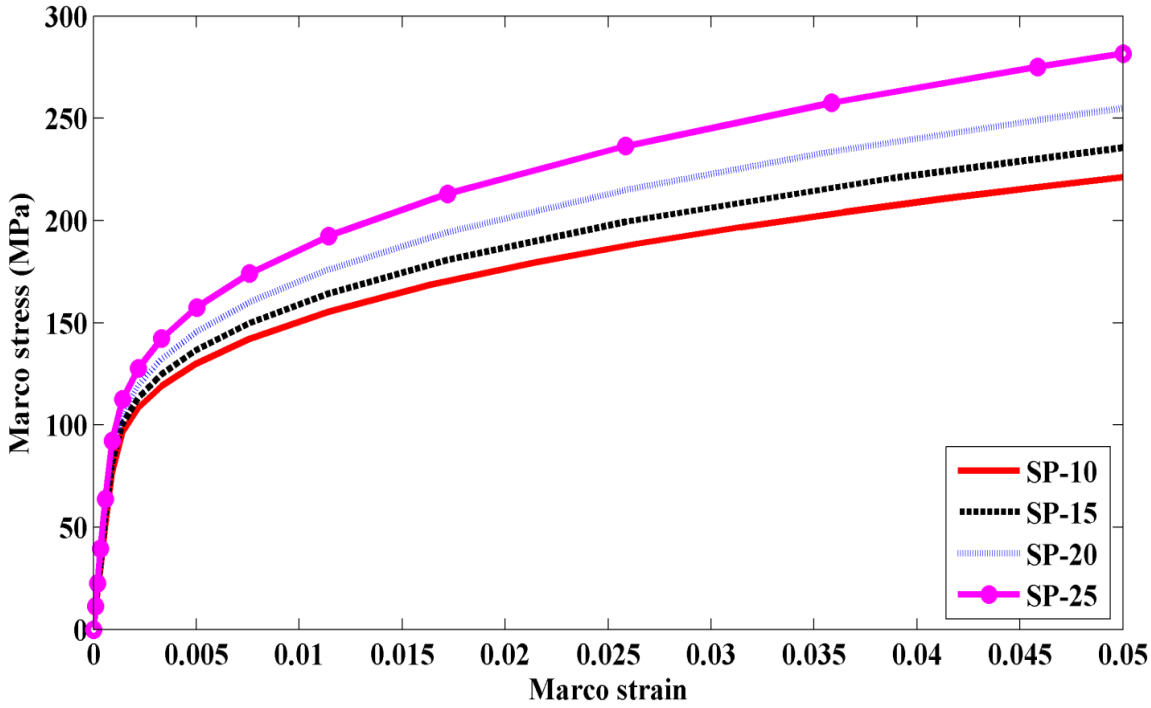

(b) Single particle Unit Cell

Fig. 5.8: Comparison of average stress-strain curves of (a) multi-particle unit cells (b) single particle unit cells

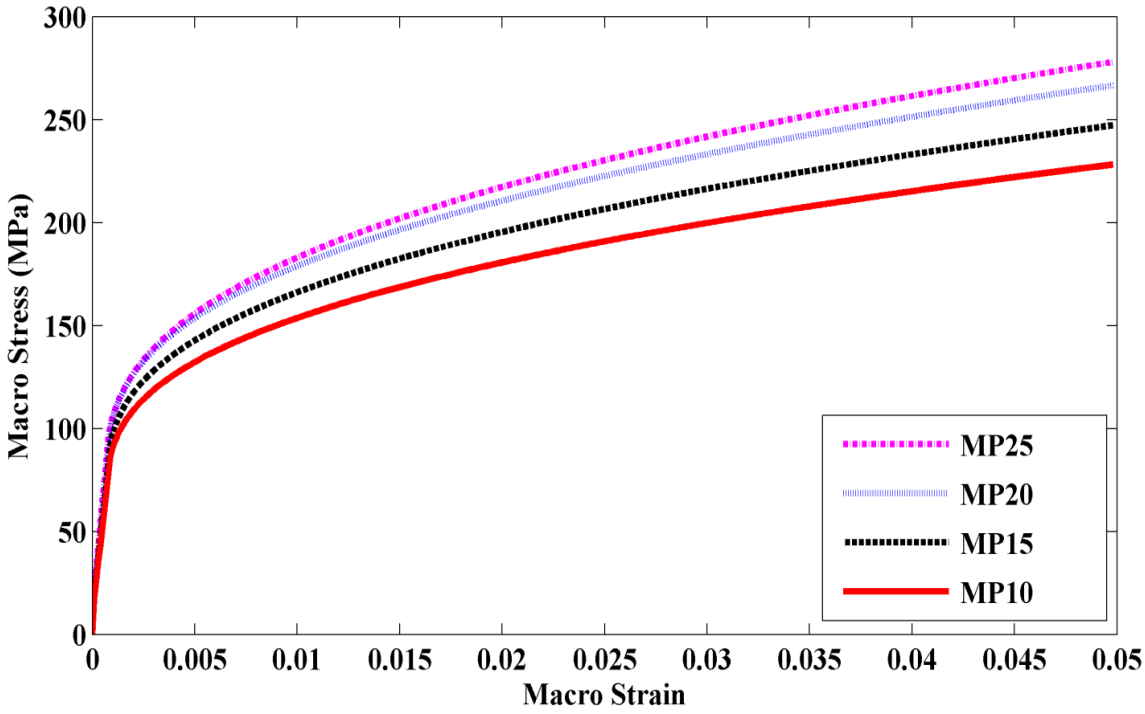

Fig. 5.9: Comparison of stress-strain curves of multi-particle unit cells predicted by analytical model under uniaxial tensile loading

Comparison between Numerical and Analytical results

Fig. 5.10 shows the comparison of numerical results and analytical results of multi-particle unit cells and single particle unit cells at each volume fraction of particles. It can be seen that multi-particle unit cells predict the moderate responses, while the analytical model predicts the strongest response and single particle unit cells predict the softest response in Fig. 5.10 (a), (b) and (c). However, the single particle unit cell is observed to exhibit the strongest response, while the analytical model exhibits the softest response for unit cell with particle volume fraction of 25% in Fig. 5.10 (d). The maximum percentage differences of Cauchy stress between single particle unit cells and multi-particle unit cells are 1.4%, 0.62%, 2.5%, and 0.37% for f = 10%,

15%, 20% and 25%, respectively. By comparing the analytical results with the multi-particle unit cell, the percentage differences can be obtained as follows: 1.8%, 4.2%, 1.9% and 0.93%, respectively. It can be concluded that, in general, multi-particle unit cells provide a moderate stress-strain response while the analytical model predicts the strongest response and single particle unit cells give the softest response.

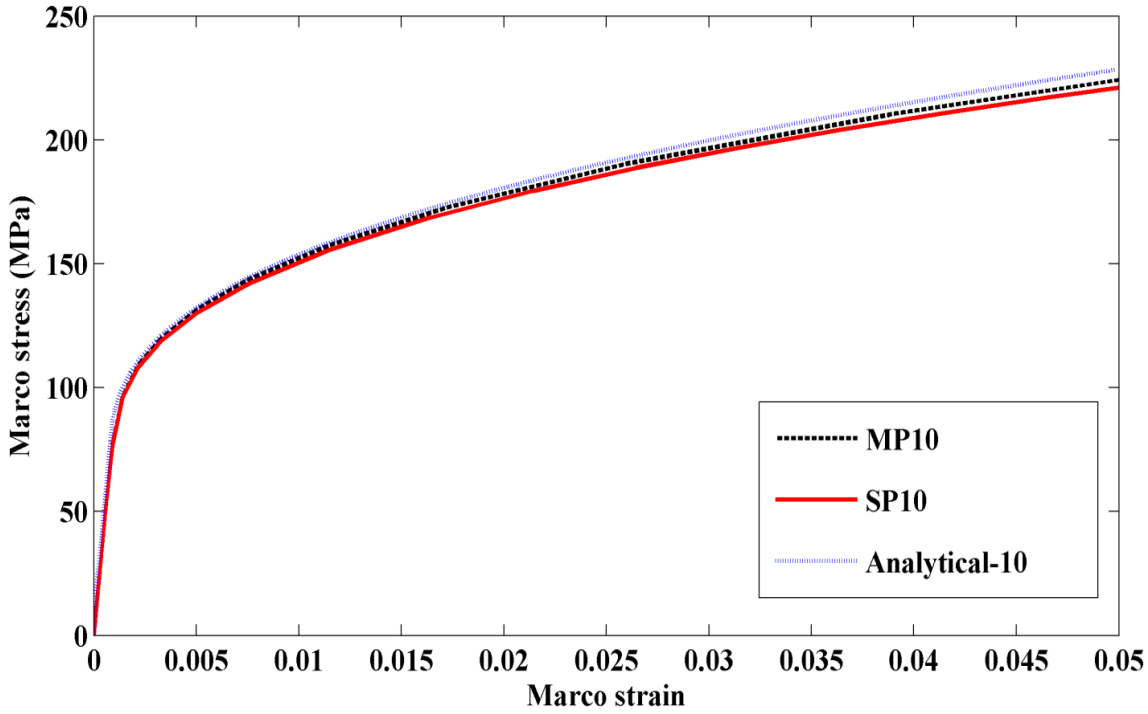

(a) 10% particle volume fraction

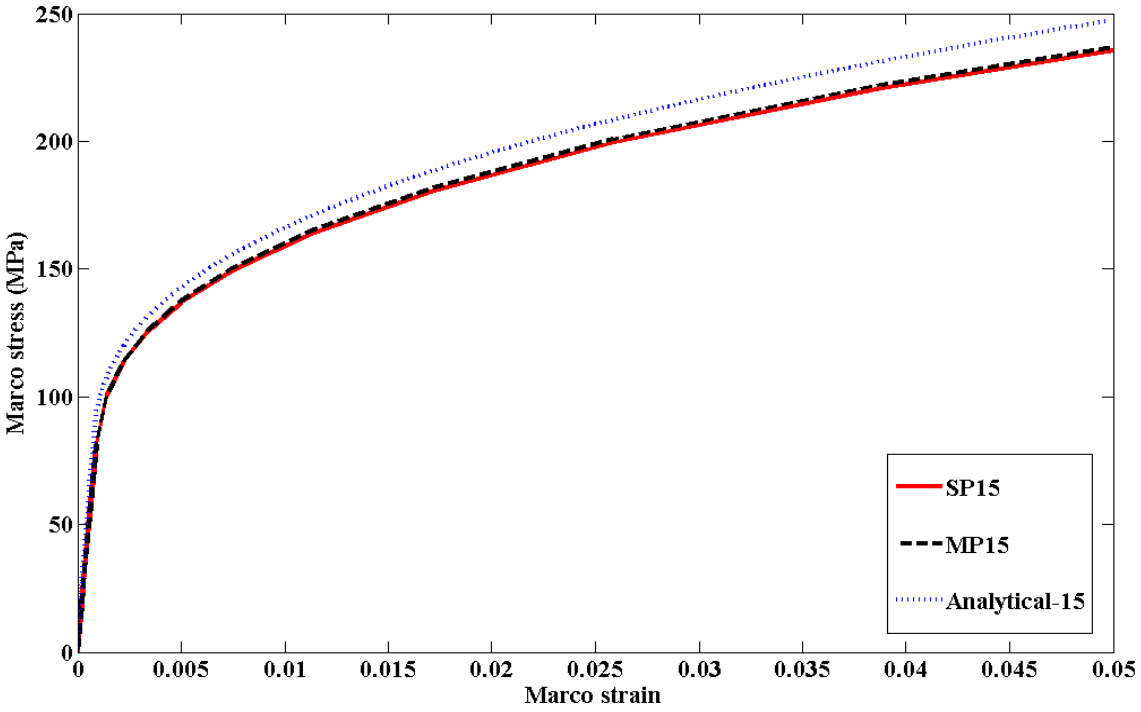

(b) 15% particle volume fraction

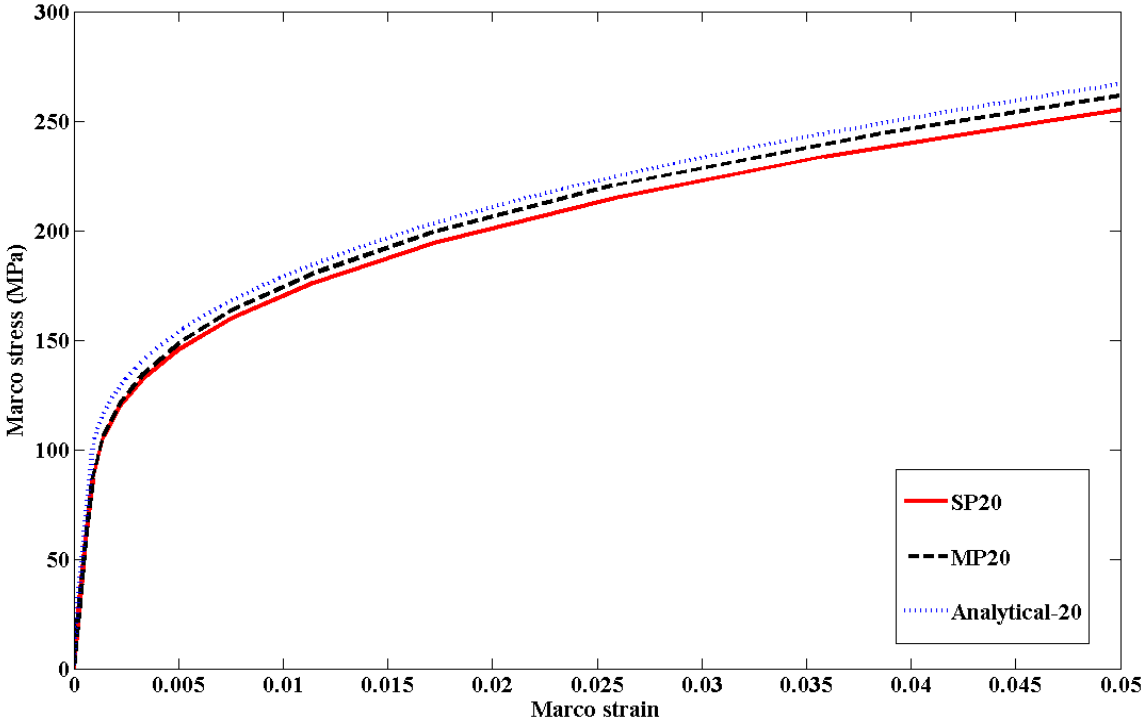

(c) 20% particle volume fraction

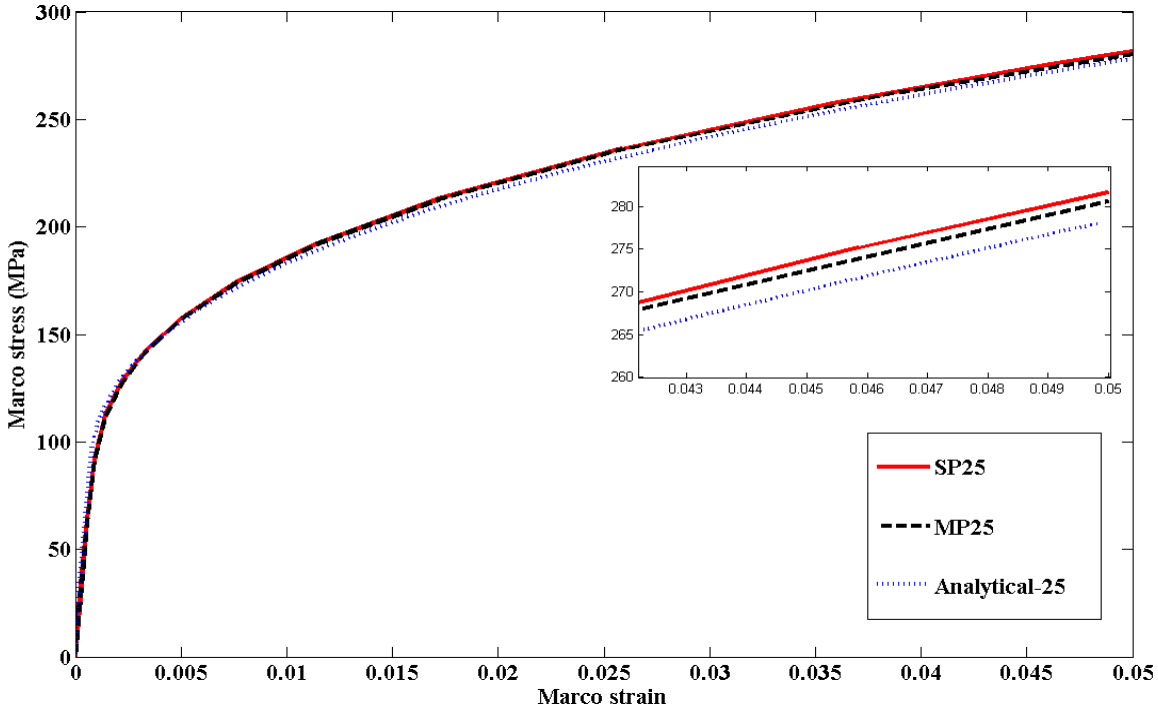

(d) 25% particle volume fraction

Fig. 5.10: Comparisons of tensile stress-strain curves of numerical and analytical models

Effects of Particle Size

Unit cells with 1, 5, 15, 20, 30 and 45 particles are built and evaluated to reveal the effects of size on stress-strain behaviors. The volume fraction of particles is constant at 10%. Unit cells with 30 and 45 particles are shown in Fig. 5.11. The tensile stress-strain curves of these unit cells are compared, as shown in Fig. 5.11. All the stress-strain curves are close to each other; the maximum difference of Cauchy stress is found to be 1.7% at a far-field strain of five percent. The largest ratio of radii of particles is 3.56. This ratio can be used as a measurement of the variation of particle sizes. Fig 5.12 indicates that particle size does not play an important role in the Cauchy stress of composites, in case of a small ratio of radii of particles. Larger effects of

particle sizes may be found for a larger ratio of the radii of particles (e.g. 10, 50). However, it is difficult to investigate the effects of particle size with a large ratio of particle radii by using numerical simulation. In order to get a large ratio of particle radii, it may results into thousands of smaller particles compared with 20 particles with the same particle volume fraction. Much research has been done on the effects of particle size. Abedini [78] demonstrated that as the particle size decreased, the strengthening and hardening effects on the overall behavior of the composites increased by using tangent-based model. Suh et al. [57] demonstrated that smaller particles lead to a higher strengthening effect, and size effect was found to be pronounced at larger particle volume fractions.

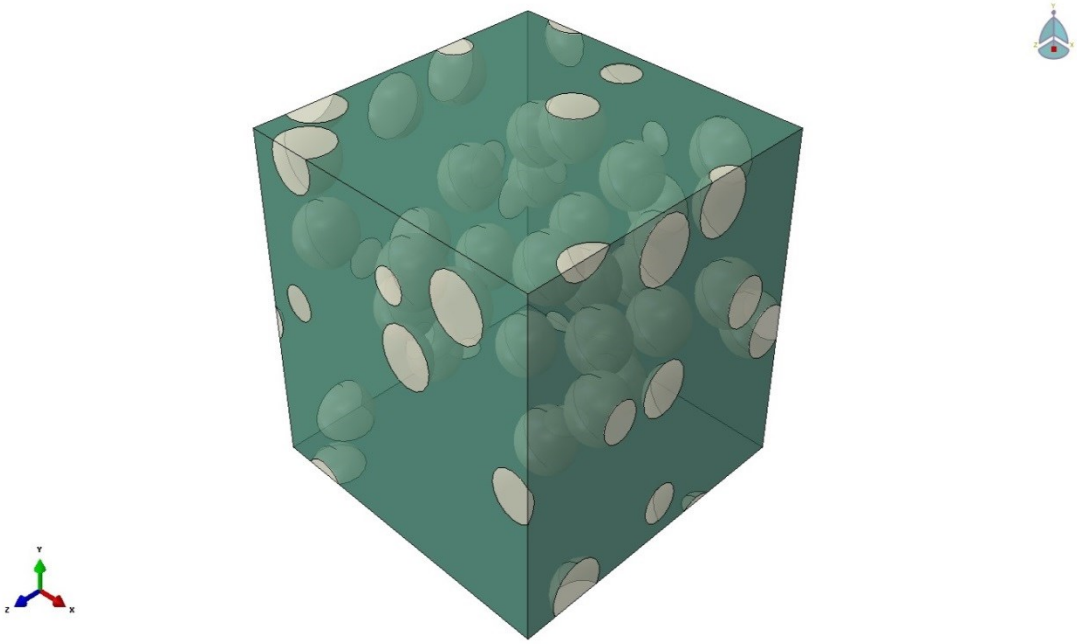

(a) 20 particles

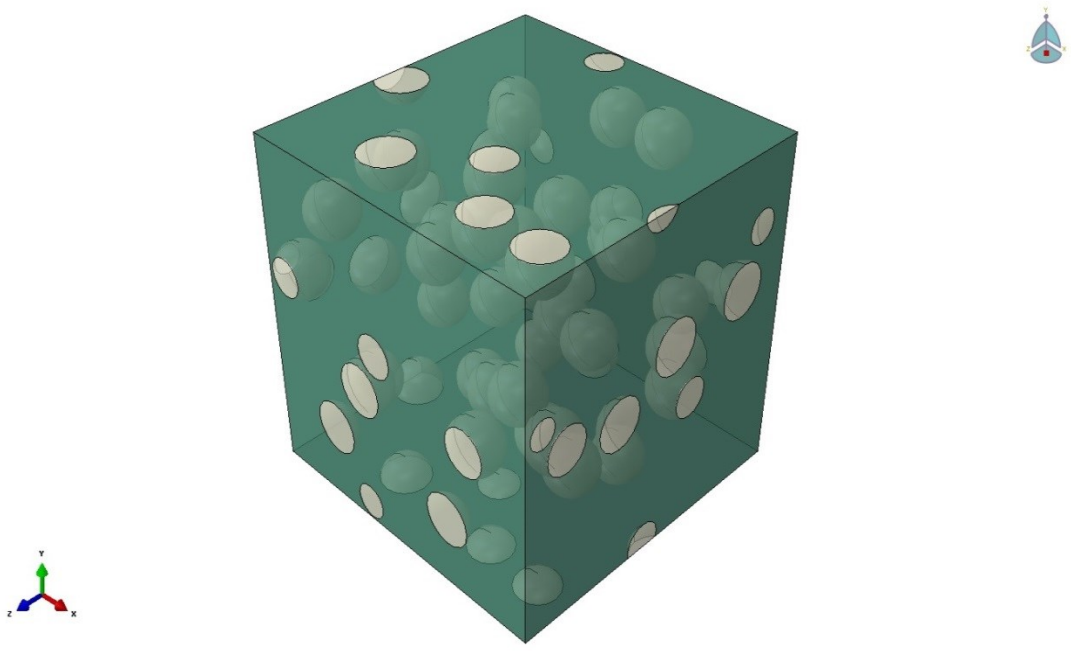

(b) 45 particles

Fig. 5.11: Unit cells with 10% volume fraction of particles (a) 20 particles (b) 45 particles

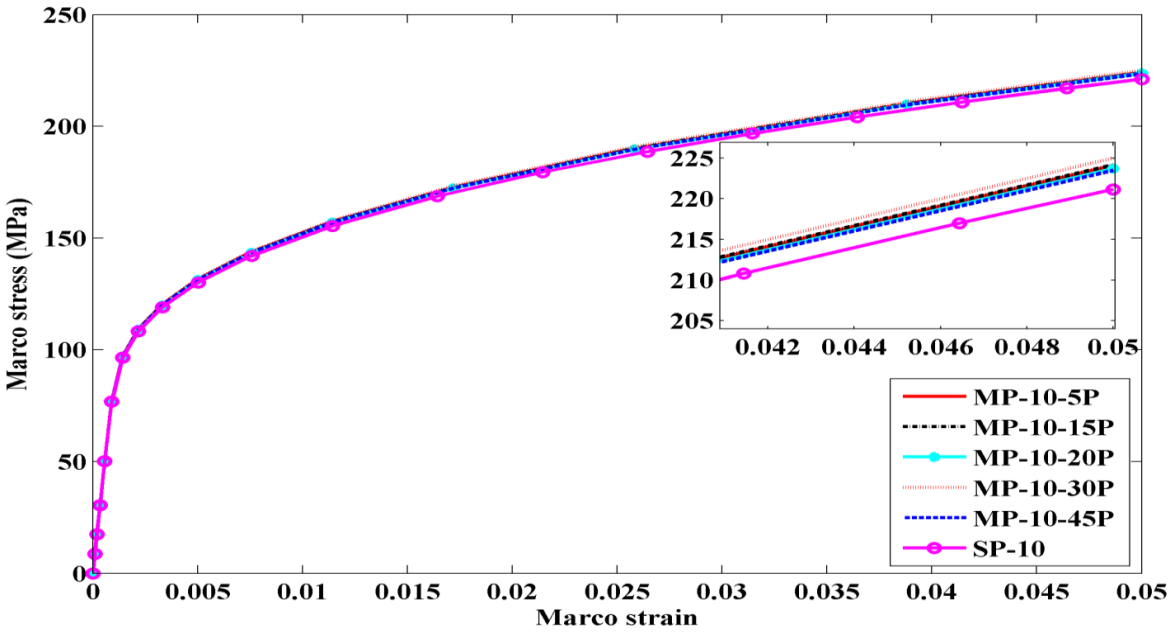

Fig. 5.12: Comparison of Multi-particle unit cell with 10% particle volume fraction with different number of particles inside the unit cell

5.2.2.2. Microscopic Response

While the macroscopic response of composite materials is important in many ways, it does not provide any information about how heterogeneous material (metal matrix and elastic particles) behaves and fails. The initiation of failure is more like a local event. By investigating the microscopic responses, the areas where have higher stress need to be paid attention, since these areas are the places where de-bonding or cracking most likely occurs. Therefore, microscopic response of composite materials is also necessary. Accurate results can be provided by using numerical techniques, like finite element software *ABAQUS/Standard* [31]. Field quantities in metal matrix and elastic particles during deformation, like von Mises stress, can be captured.

The distributions of von Mises stress of elastic particles and metal matrix are shown in Fig. 5.13. Similarly, for the metallic matrix, the maximum von Mises stress was found around the interfaces between particles and matrix. It increases with increasing particle volume fraction from 493.8 MPa to 693.5 MPa. The percentage difference of von Mises stress between single particle unit cell with 10% and 25% particle volume fraction is 33.6%. As shown in Fig. 5.13 (a), higher equivalent stress occurred at the area between two closely located particles (area B), while lower stress was found at the area around the intersection of particles and matrix (area A) and area C. Similarly, the results for elastic particles show that the highest equivalent stress occurred at the interface between particles and matrix. It turns out that the smaller intersection, the higher stress.

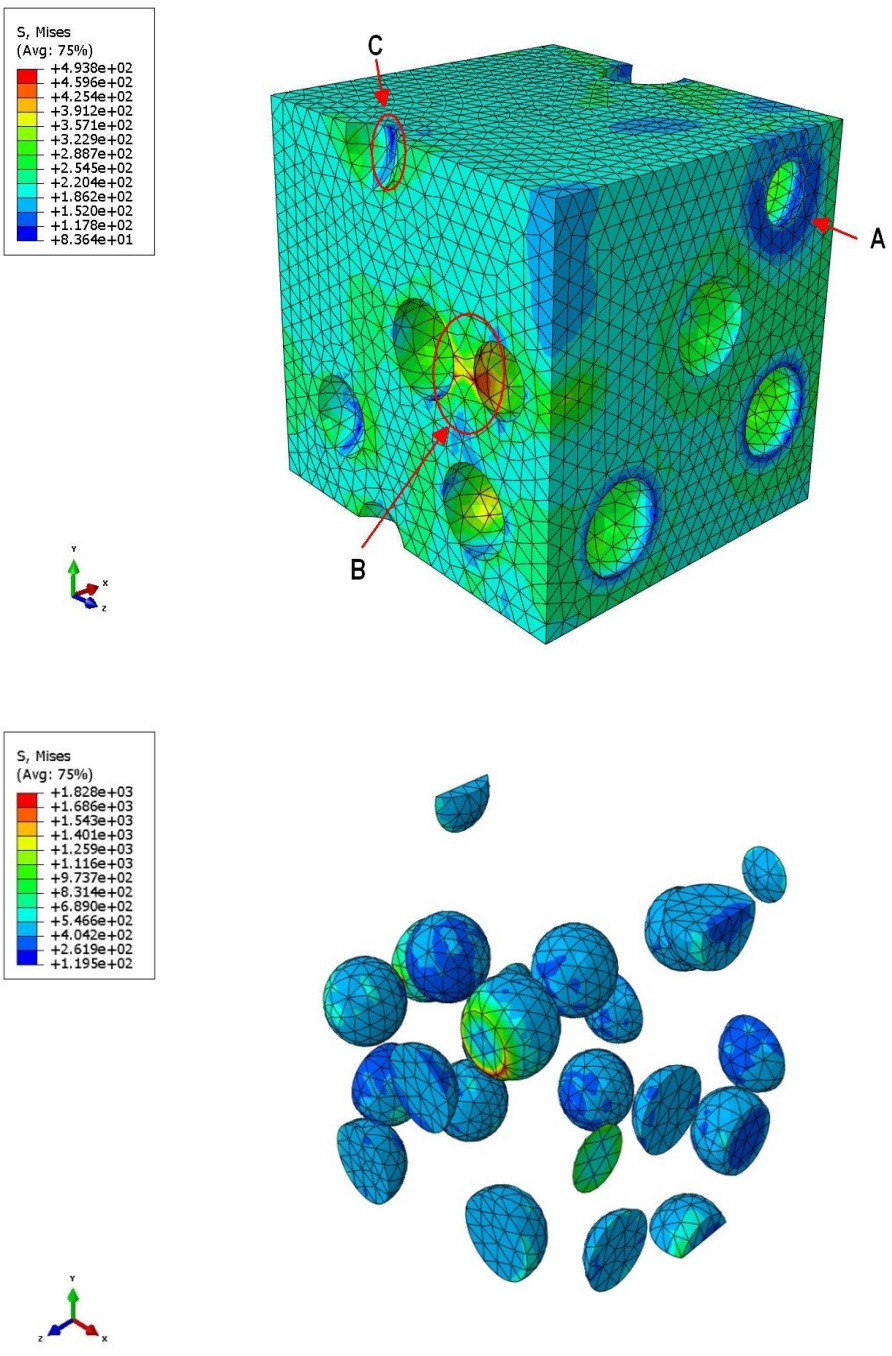
S, Mises
(Avg: 75%)
+4.938e+02
+4.596e+02
+4.254e+02
+3.912e+02
+3.571e+02
+3.229e+02
+2.887e+02
+2.545e+02
+2.204e+02
+1.862e+02
+1.520e+02
+1.178e+02
+8.364e+01
C
A
B
S, Mises
(Avg: 75%)
+1.828e+03
+1.686e+03
+1.543e+03
+1.401e+03
+1.259e+03
+1.116e+03
+9.737e+02
+8.314e+02
+6.890e+02
+5.466e+02
+4.042e+02
+2.619e+02
+1.195e+02

(a) 10%

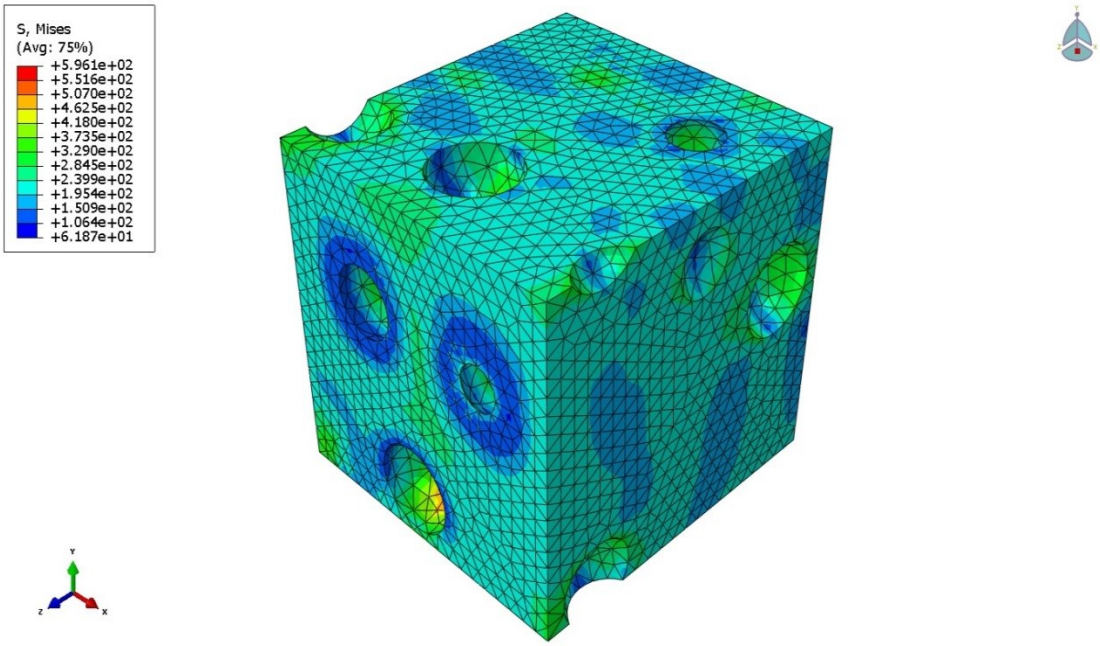
S, Mises
(Avg: 75%)
+5.961e+02
+5.516e+02
+5.070e+02
+4.625e+02
+4.180e+02
+3.735e+02
+3.290e+02
+2.845e+02
+2.399e+02
+1.954e+02
+1.509e+02
+1.064e+02
+6.187e+01

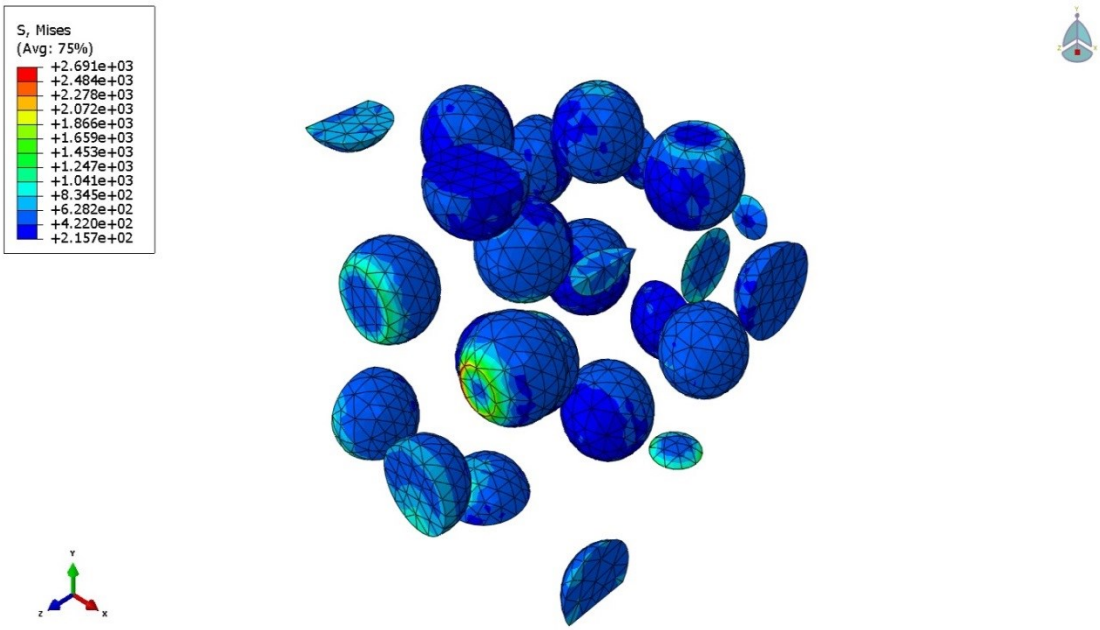
S, Mises
(Avg: 75%)
+2.691e+03
+2.484e+03
+2.278e+03
+2.072e+03
+1.866e+03
+1.659e+03
+1.453e+03
+1.247e+03
+1.041e+03
+8.345e+02
+6.282e+02
+4.220e+02
+2.157e+02

(b) 15%

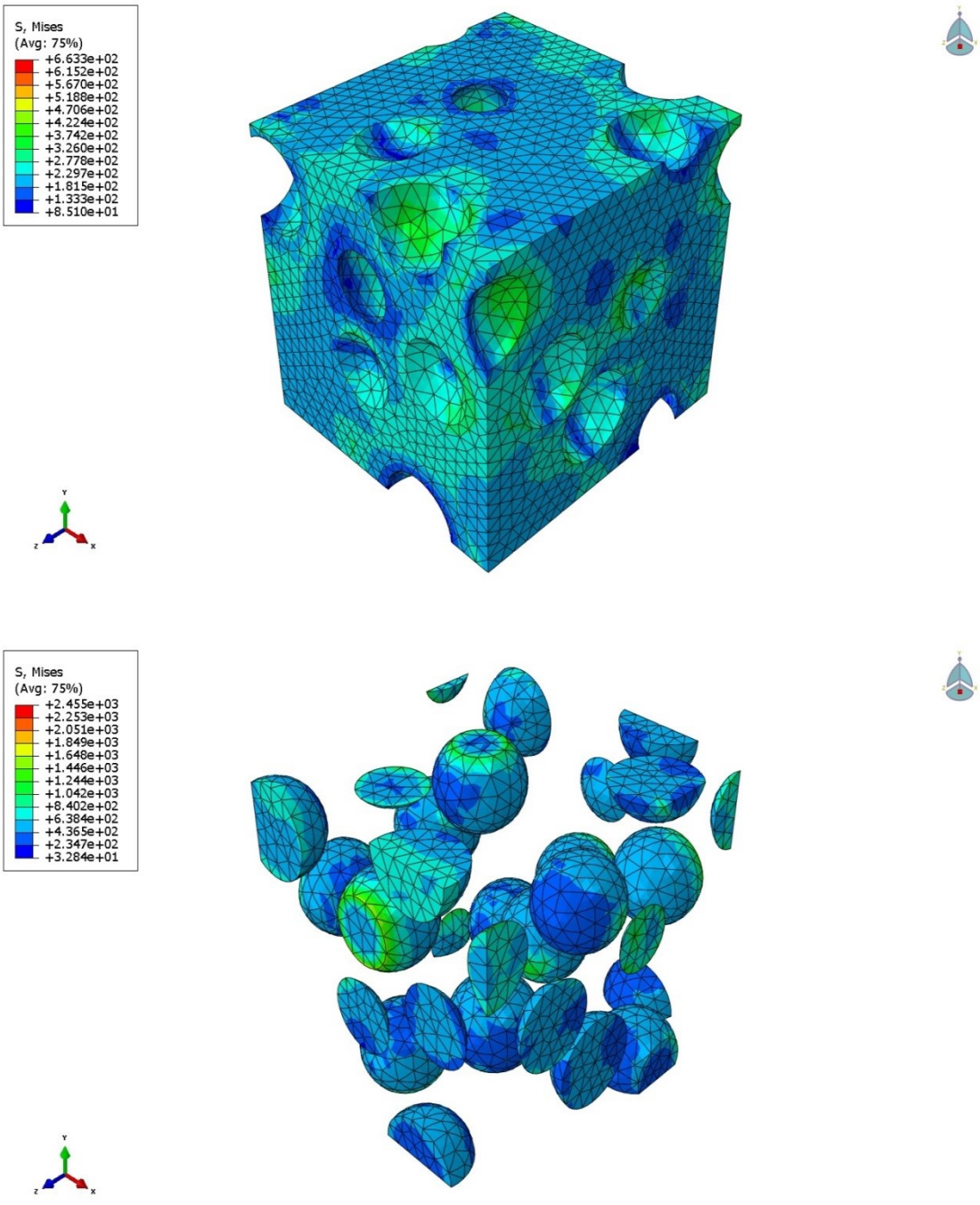
S, Mises
(Avg: 75%)
+6.633e+02
+6.152e+02
+5.670e+02
+5.188e+02
+4.706e+02
+4.224e+02
+3.742e+02
+3.260e+02
+2.778e+02
+2.297e+02
+1.815e+02
+1.333e+02
+8.510e+01
S, Mises
(Avg: 75%)
+2.455e+03
+2.253e+03
+2.051e+03
+1.849e+03
+1.648e+03
+1.446e+03
+1.244e+03
+1.042e+03
+8.402e+02
+6.384e+02
+4.365e+02
+2.347e+02
+3.284e+01

(c) 20%

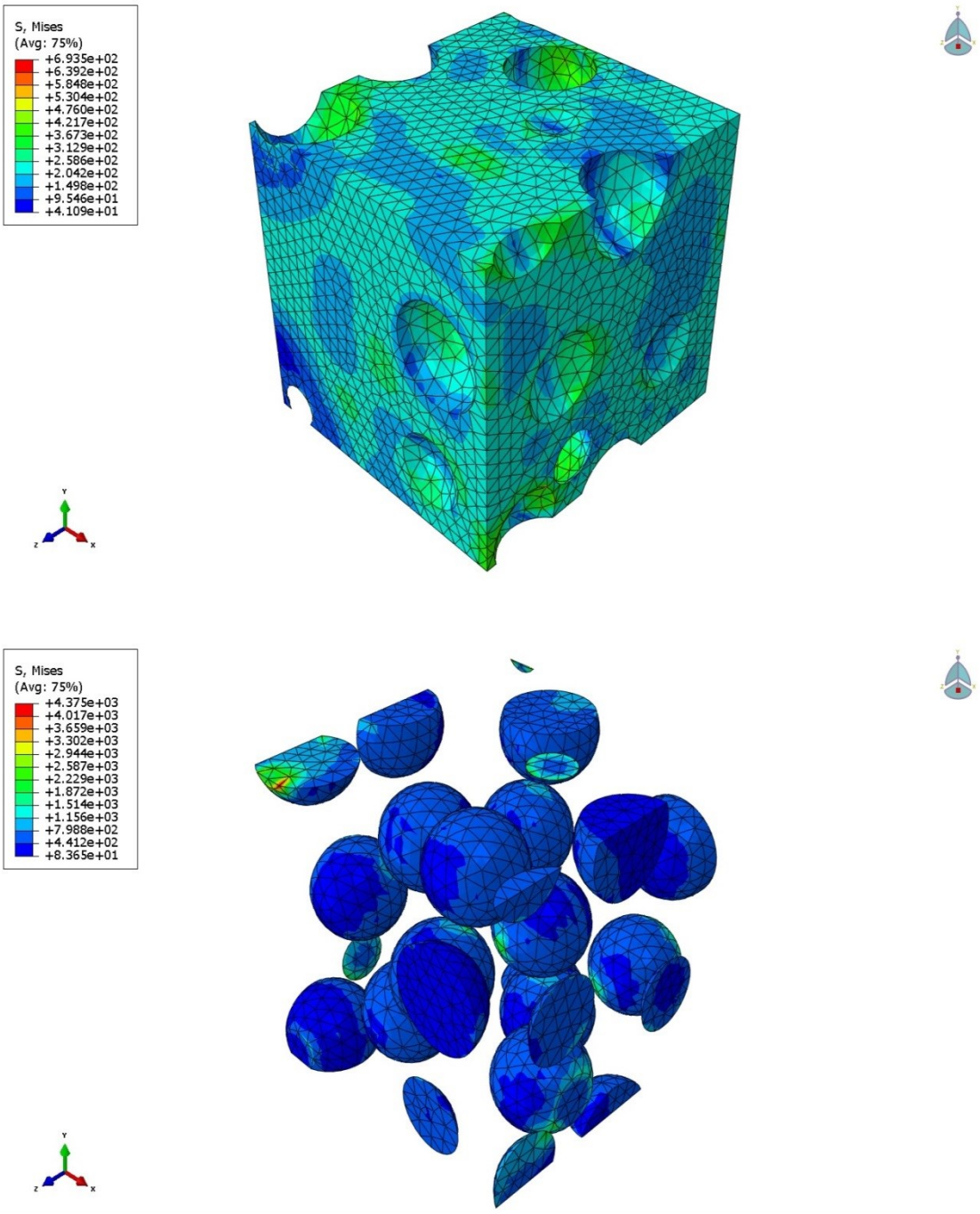

(d) 25%

Fig. 5.13: Equivalent Stress distribution of MP unit cell (a) 10%, (b) 15%, (c) 20% and (d) 25%

5.3. Micromechanical Modelling of Hot Rolled Steels

5.3.1. Material Response under Specific Stress States

This section devotes to provide the microscopic responses of HRSF steels. The purpose of building micromechanical model for HR steels is to reveal the local stress distribution of HR steels under specific stress states. It helps us to understand the local behavior around hard martensitic phases of HR steels. The volume fraction of martensite is assumed to be around 10% based on scattered measurement results. Since the martensitic phase is relatively hard to yield, the combination of bainitic and ferritic phases can be treated as soft metallic matrix, while martensite can be treated as elastic particles. Same strategies as mentioned in section 5.2 are used to generate the micromechanical model. However, particles are allowed to be overlapped in these micromechanical models in order to achieve more accurate results. The completed models with 10%, 15% and 20% volume fractions of particles are shown in Fig. 5.14. Green areas are ferrite/bainite, and while areas are elastic particles. The material properties are shown in Table 5.2.

Table 5.2: Material properties for micromechanical model

	Material	Property	E (GPa)	ν	Yield stress (MPa)
Material	Ferrite Bainite	Elastic-plastic	210	0.33	685.24
Particle	Martensite	Elastic	210	0.33	1052.8

Since the combination of ferritic and bainitic phases is treated as soft matrix while martensitic phase is treated as hard particles. The tensile strength of matrix can be obtained by using the rule of mixture [79, 80]

$$\sigma = f\sigma_p + (1 - f)\sigma_m \tag{5.5}$$

f refers to the volume fraction of particles, σ_p and σ_m refer to tensile strength of particle and matrix, respectively. σ refers to the tensile strength of the composite.

The tensile strength of martensite can be calculated by using equation [80]

$$\sigma_{mar} = 541 + 2289(C_{mar})^{0.5} \tag{5.6}$$

Where σ_{mar} refers to tensile strength of martensite, C_{mar} refers to the carbon content (in wt%).

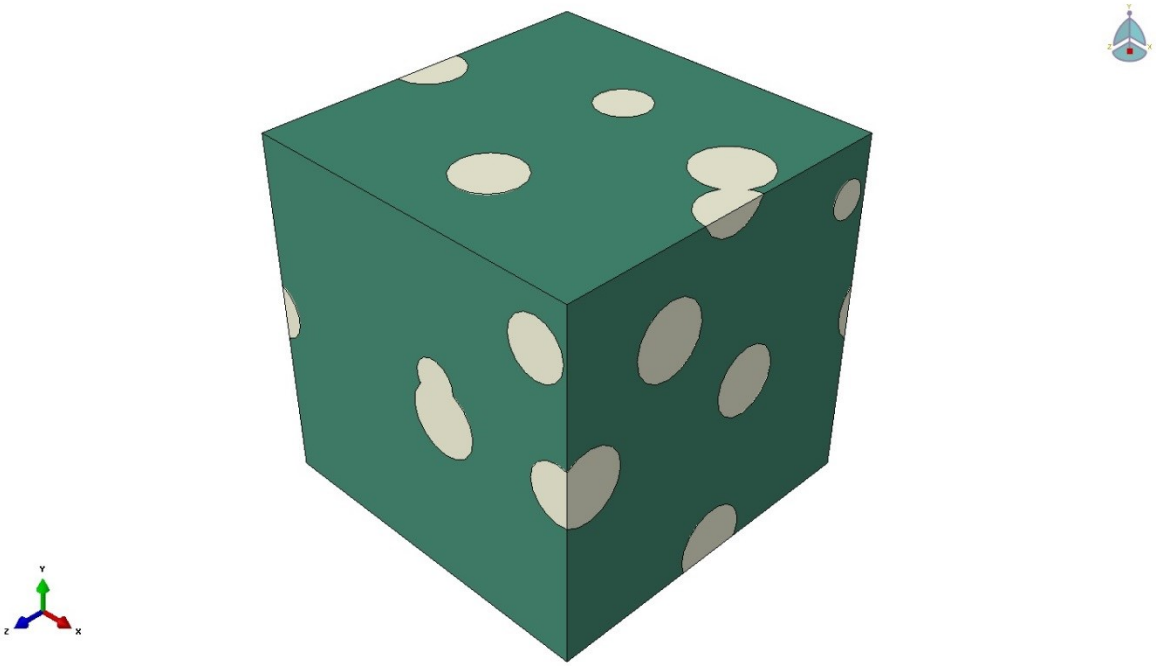

(a) Micromechanical model with 10% volume fraction of particles

(b) Micromechanical model with 15% volume fraction of particles

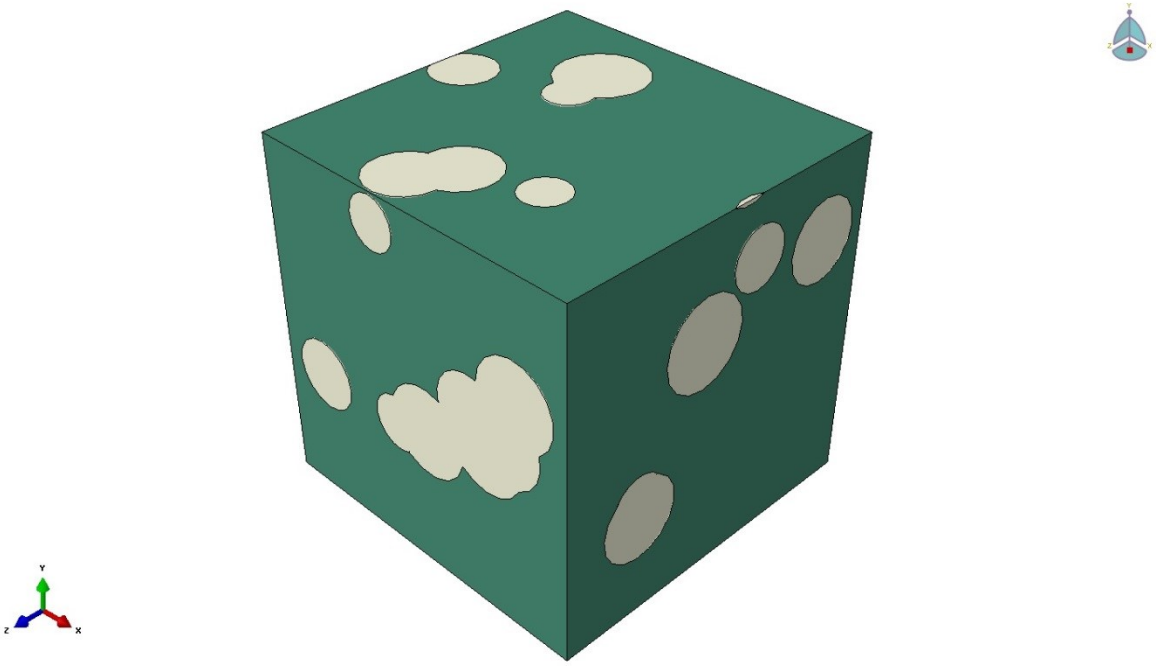

(c) Micromechanical model with 20% volume fraction of particles

Fig. 5.14: Micromechanical model for HR steels

Fig. 5.15 shows the stress states and their directions applied on the unit cell. Three normal stresses and three shear stresses are extracted from the FE models of circular-notched steel samples and then applied to the multi-particle unit cells. The detailed data of applied stress states of circular-notched steel samples with notch radii of 2 mm, 4 mm, 6 mm and 8 mm are listed in Table 5.3.

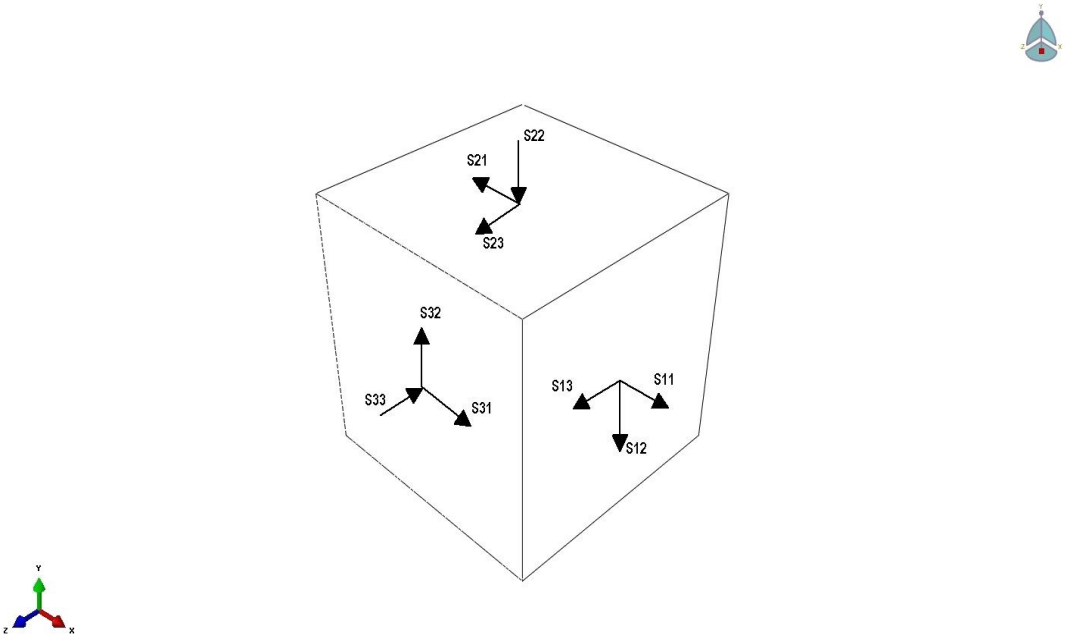

Fig. 5.15: Applied stress states of the unit cell

Table 5.3: Stress states of steel sample A80273

Stress components S_{ij} (MPa)	A80273			
	R2	R4	R6	R8
S11	240.893	252.805	255.032	253.66
S22	97.77	60.662	41.725	30.929
S33	1.98	0.903	0.548	0.393
S12	0.103	0.662	0.129	0.0949
S13	0.014	0.0125	0.00191	0.00129
S23	0.0436	0.018	0.00812	0.0053

The distributions of equivalent stresses for unit cells with different applied stress states are shown in Fig. 5.16 (a), (b), (c) and (d). For the unit cell with stress states extracted from A80273 sheet steel sample with 2 mm of notch radius, the maximum equivalent stress is found to be 1,708 MPa. The maximum stress decreases as the notch radius increases. The maximum equivalent stresses of unit cells with stress states extracted from A80273 sheet steel samples with 4 mm, 6 mm and 8 mm of notch radius are found to be 1,508 MPa, 1,430 MPa and 1,363 MPa, respectively. According to these contour plots of equivalent stress, lower stresses are distributed around the particles in the direction perpendicular to the direction of normal stress in x-direction (S11). Moreover, higher stresses are distributed on interfacial areas of particles and metal matrix in the direction of normal stress in x-direction (S11). Therefore, de-bonding probably occurs at the interfaces between matrix and particles, especially in the direction of S11.

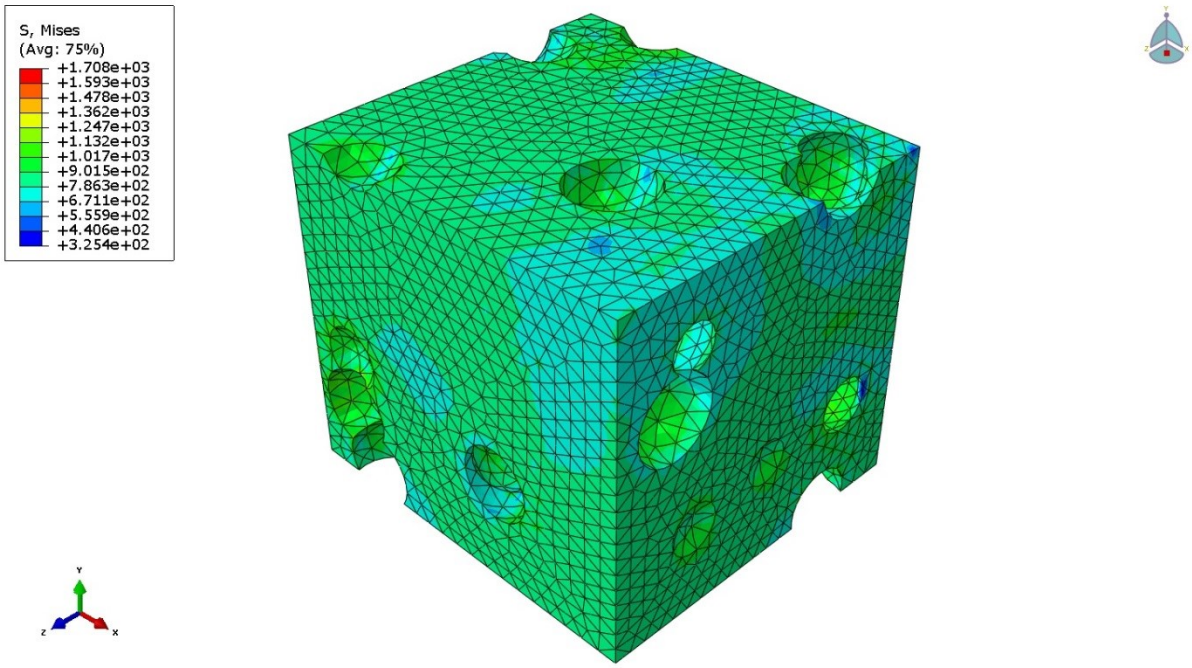
S, Mises
(Avg: 75%)
+1.708e+03
+1.593e+03
+1.478e+03
+1.362e+03
+1.247e+03
+1.132e+03
+1.017e+03
+9.015e+02
+7.863e+02
+6.711e+02
+5.559e+02
+4.406e+02
+3.254e+02
Y
Z
X

(a) R2

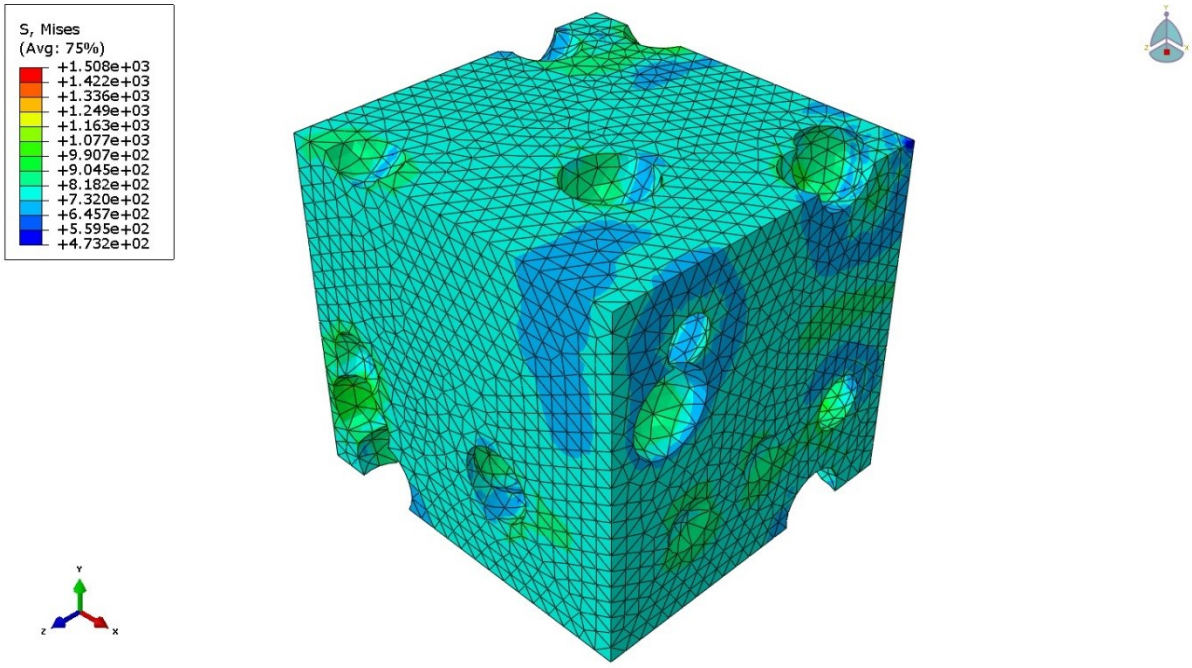
S, Mises
(Avg: 75%)
+1.508e+03
+1.422e+03
+1.336e+03
+1.249e+03
+1.163e+03
+1.077e+03
+9.907e+02
+9.045e+02
+8.182e+02
+7.320e+02
+6.457e+02
+5.595e+02
+4.732e+02
Y
Z
X

(b) R4

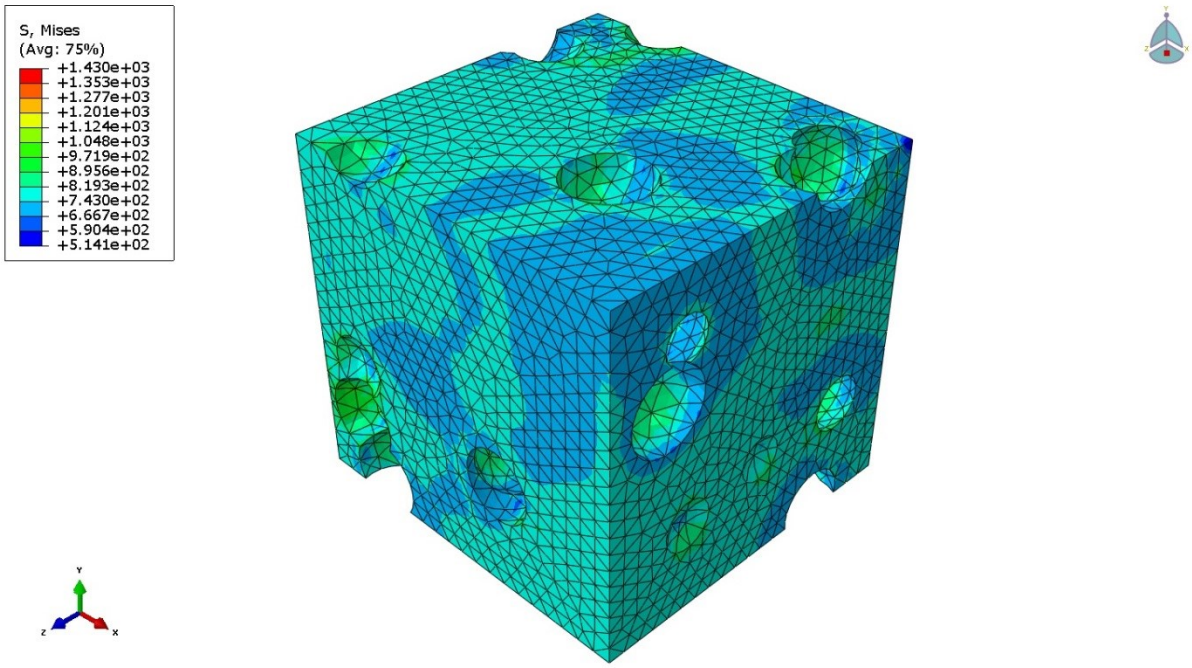

(c) R6

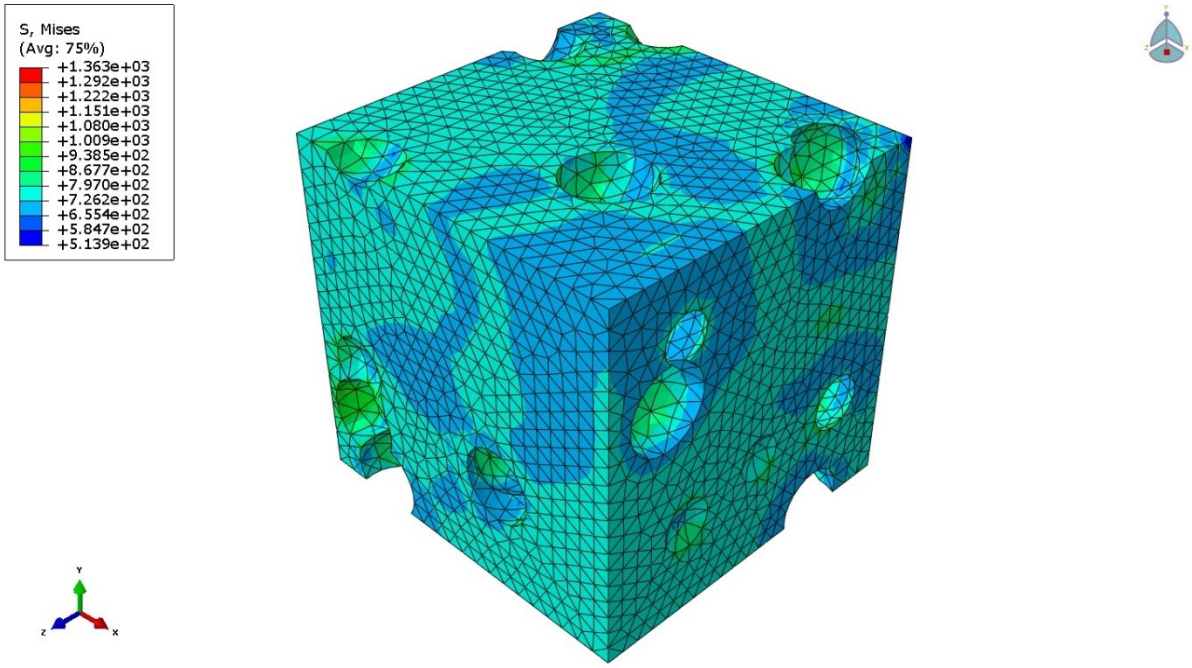

(d) R8

Fig. 5.16: Mises stress distributions for unit cells with different stress states of (a) R2 (b) R4 (c) R6 and (d) R8. Volume fraction of particles is 15%.

Fig. 5.17 shows the stress behavior of interfacial nodes between elastic particles and metallic matrix and nodes on particle cross-section and matrix. The red "saw teeth" shaped curve is the stress behavior of interfacial nodes. The upper (black curve) and lower bounds (blue curve) of the red curve are the equivalent stresses of nodes on particles and matrix. The reason that the stress behaves like this is that the particles are assumed to be perfectly bonded with the matrix. Metallic matrix and particles are connected by interfacial nodes. When the metallic matrix starts to deform, particles are forced to move with the matrix. Therefore, at the same time step, the interfacial nodes exhibit the stress behavior of both particles and matrix.

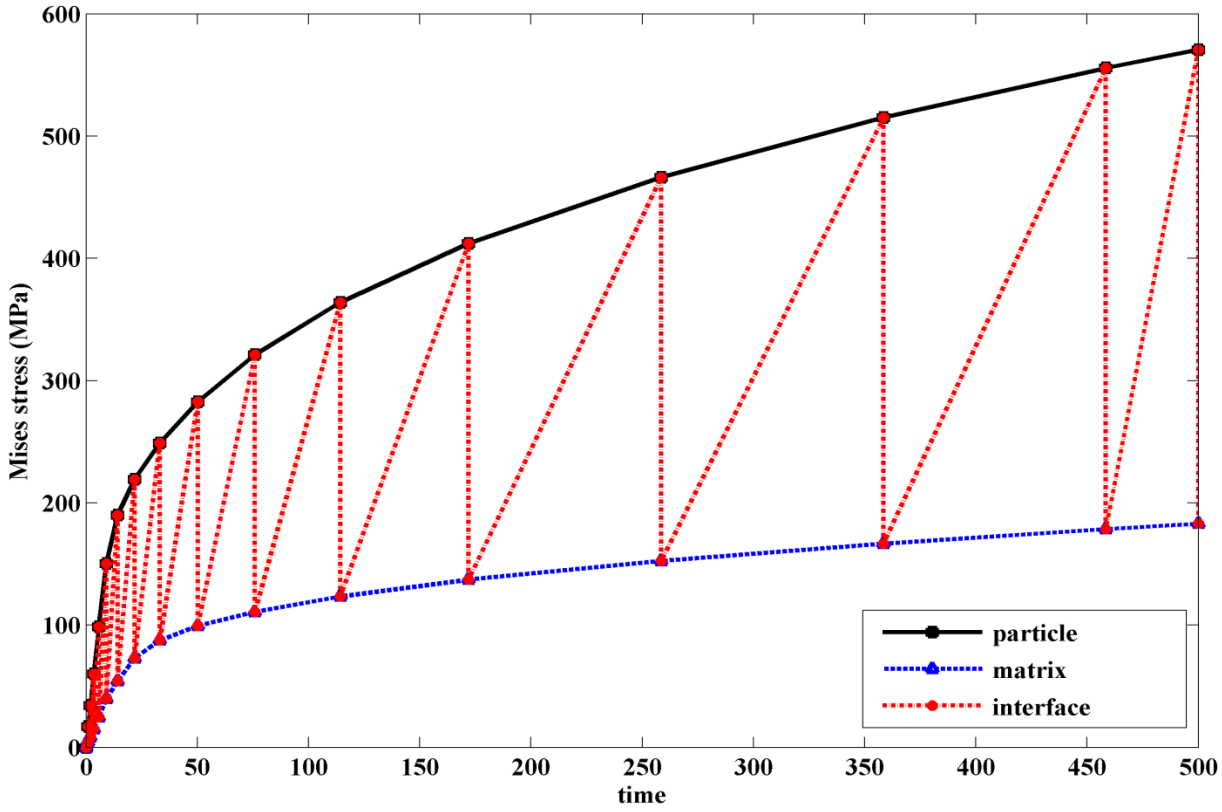

Fig. 5.17: Stress behavior of interfacial nodes of a unit cell model

5.3.2. Stress-strain relations

Periodic boundary conditions are applied on the micromechanical model. The stress-strain curves of experiment, FE model, and micromechanical models are shown in Fig. 5.18. The micromechanical model with 15% volume fraction of particles provides the best results to the results of experiment and FE model. The micromechanical model with 10% volume fraction of martensitic particles provides a softer response while micromechanical model with 20% volume fraction of martensitic particles provides a stronger response. The discrepancy between the results of experiment and micromechanical models is found in the yield area. The reason is that the accurate volume fraction of each phase in HR steels is unknown. Therefore, the results may show the discrepancy in the yield behavior of the stress-strain responses.

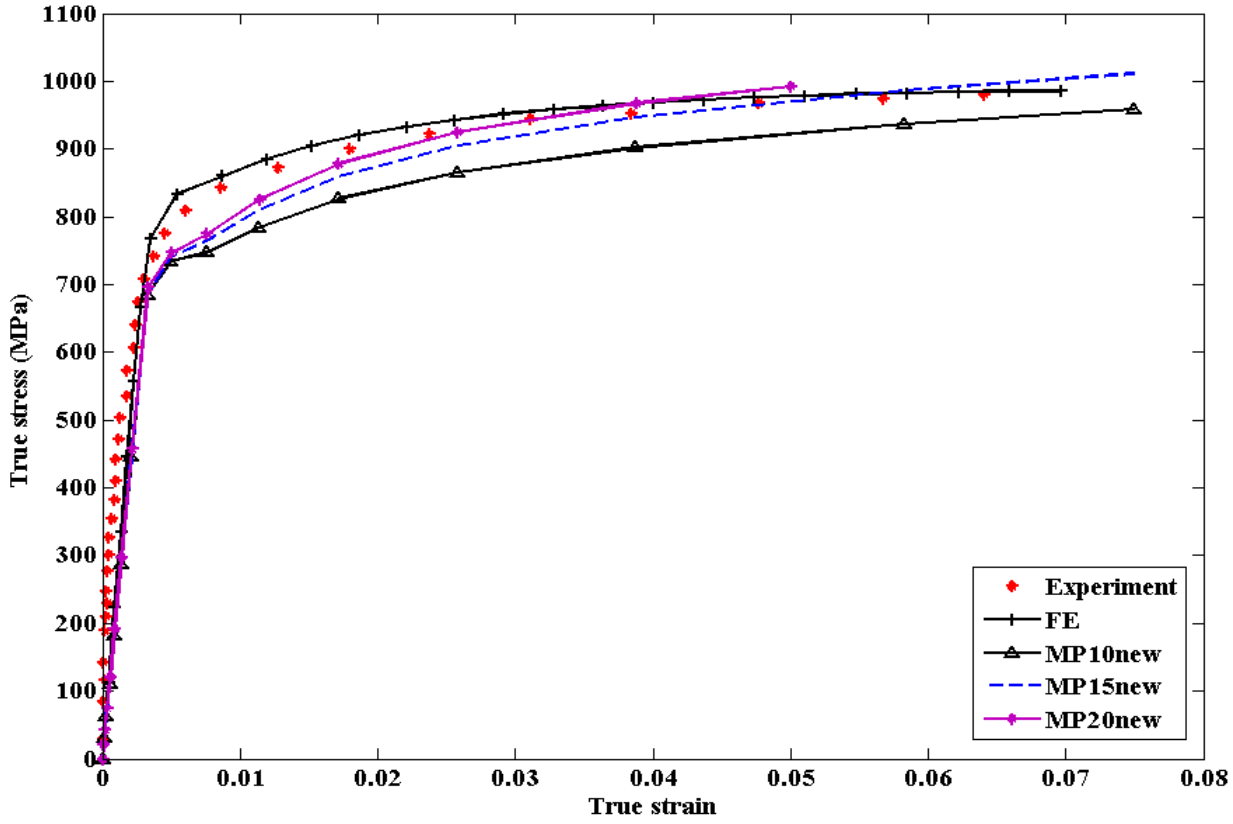

Fig. 5.18: Comparison of stress-strain relations

6. Conclusions and Recommendations

6.1. Conclusion

The principal objective of the present work was to investigate the effects of notch geometry on stress-strain relations of hot rolled stretch flangeable steel (HR780SF) during uniaxial tensile tests by using both experimental and finite element approaches. The experimental approach was to perform uniaxial tensile tests on the circular-notched sheet steel samples. In the meantime, digital image correlation technique (DIC) was used to measure the changes of strain during the whole deformation process. Finite element models of circular-notched steel samples were also built and evaluated by using *ABAQUS/Standard* [31].

Primary conclusions were summarized as follows:

- In order to evaluate the effects of the volume fraction of reinforcement on the stress-strain behavior of hot rolled steels, three-dimensional multiple-particle unit cell was built and evaluated. Identical spherical particles were randomly distributed inside the unit cell by using random sequentially adsorption algorithm (RSA). The results demonstrated that the Cauchy stress increases with the increasing volume fraction of reinforcement (< 30%). In order to validate the multiple-particle unit cell, stress-strain behaviors of multiple-particle unit cell were compared with the results of single particle unit cell and analytical tangent homogenization model. It demonstrated that multiple-particle unit cell predicts a moderate response while analytical model predicts the strongest response.

- In the view of microscopic responses, a small displacement was applied on the unit cell to resemble a uniaxial load in tension. The results demonstrated that the equivalent stress distributed on the unit cell increases with increasing volume fraction of reinforcement.
- Approximately 0.22% to 9.56% differences of maximum forces were found between experimental and finite element results. The stress-strain responses of finite element models were stronger than the experimental results. These differences were mainly caused by the voids inside the material since the effects of voids were not considered in finite element models.
- Microstructures of tested notched steel samples demonstrated that most changes occurred in the necked area. Grains were elongated about 45° and voids were observed in the necked area.
- The microscopic responses of HRSF steels were also investigated by extracting stress states from macroscopic models and applying them on the micromechanical models. The results demonstrated that lower stresses were distributed around the particles in the direction perpendicular to the direction of normal stress in x-direction while higher stresses were distributed on interfacial areas between particles and metal matrix in the direction of normal stress in x-direction.
- The micromechanical models with 10% volume fraction of particles provided the closest results in comparison with the results of experiment and FE model. The discrepancy was found in the plastic regime of stress-strain curves.
- De-bonding probably occurred at the interface between matrix and particles. Especially in the direction along loading direction.

6.2. Recommendations for Future Work

Some recommendations are proposed and could be done in the future to further the present work are listed as follows:

- Repeat the uniaxial tensile tests on different sheet steel samples to minimize the errors caused by testing environment, DIC preparations, etc.
- The effects of damage and failure can be considered in finite element models to provide profiles of complete deformation process.
- Standard RSA algorithm can only be used for volume fraction of particle less than 30%. Modified RSA algorithm can be developed and used to build unit cell with volume fraction of particles up to 50%.
- Identical spherical particles were used in the present work to build the multiple-particle unit cells. Reinforcement with difference sizes and shapes can be considered to evaluate the material behavior of particle-reinforced composites. For example, ellipsoidal or irregular shaped particle, and continuous fibers. Note that the orientations of particles need to be considered if particle shape is not spherical. Unit cell with irregular shaped particles may provide more accurate material responses.
- A small volume fraction of voids can be added to the unit cell to provide a more realistic material response.
- Circular-notched sheet steel samples with different sizes of ligament can be machined and tested to investigate the effects of ligament size on material behavior of HRSF steels.

- Scan electron microscope (SEM) and more advanced equipment and other etching techniques can be used to validate the results of optical microscope and distinguish different phases of HRSF steels.
- Other experiments can be performed to further investigate the HR steels. For example, hole expansion tests can be used to test the stretch flangability of HR steels.

Bibliography

[1] V. Uthaisangsuk, U. Prahl, and W. Bleck, 2008, "Micromechanical Modelling of Damage Behavior of Multiphase Steels," Computational Materials Science, 43(1), pp. 27-35.

[2] C.M. Tamarelli, 2011, "The Evolving Use of Advanced High-Strength Steels for Automotive Applications," Report, University of Michigan, Ann Arbor, Michigan, USA.

[3] C.D. Horvath, and J.R. Fekete, June 6-9, 2004, Proceedings of the International Conference on Advanced High Strength Steels for Automotive Applications, pp. 3-11.

[4] W. Bleck, June 19-21, 2002, Proceedings of the International Conference on TRIP-Aided High strength Ferrous Alloys, pp. 13-23.

[5] U. Prahl, S. Papaefthymiou, and V. Uthaisangsuk, 2007, "Micromechanics-Based Modelling of Properties and Failure of Multiphase Steels," Computational Materials Science, 39, pp. 17-22.

[6] G. Bao, J.W. Hutchinson, and R.M. McMeeking, 1991, "Particle Reinforcement of Ductile Matrices against Plastic Flow and Creep," Acta Metallurgica Et Materialia, 39 (8), pp. 1871-1882.

[7] N. Pathak, C. Butcher, M. Worswick, E. Bellhouse, and J. Gao, 2014, "Edge Formability and Material Characterization of Hot-Rolled Multiphase Steels," SAE 2014 World Congress & Exhibition, SAE.

[8] Z.T. Chen, and M. Worswick, 2007, "Strain Loci in Stretch Flange Forming of Aluminum Alloys," Key Engineering Materials, 345-346, pp. 1085-1088.

[9] Z.T. Chen, M. Worswick, and D. Lloyd, 2006, "Damage-Based Finite Element Modelling of Stretch Flange Forming of Aluminum-Magnesium Alloy," Material Science Forum, 519-521, pp. 815-820.

[10] T. Kanit, S. Forest, and I. Galliet, 2003, "Determination of the Size of the Representative Volume Element for Random Composites: Statistical and Numerical Approach," International Journal of Solids and Structures, 40, pp. 3647-3679.

[11] V. Uthaisangsuk, U. Prahl, and W. Bleck, 2009, "Stretch-Flangeability Characterisation of Multiphase Steel using a Microstructure Based Failure Modelling," Computational Materials Science, 45 (3), pp. 617-623.

[12] K. T. Conlon, and D.S. Wilkinson, 2001, "Effect of Particle Distribution on Deformation and Damage of Two-Phase Alloys," Materials Science and Engineering: A, 317 (1-2), pp. 108-114.

[13] Y.W. Kim, J.H. Kim, and S.G. Hong, 2014, "Effects of Rolling Temperature on the Microstructure and Mechanical Properties of Ti–Mo Microalloyed Hot-Rolled High Strength Steel," Materials Science and Engineering: A, 605 (0), pp. 244-252.

[14] A. Mucsi, 2014, "Effect of Hot Rolled Grain Size on the Precipitation Kinetics of Nitrides in Low Carbon Al-Killed Steel," Journal of Materials Processing Technology, 214 (8), pp. 1536-1545.

[15] X.D. Wang, F. Li, and Q. Yang, 2013, "FEM Analysis for Residual Stress Prediction in Hot Rolled Steel Strip during the Run-Out Table Cooling," Applied Mathematical Modelling, 37 (1-2), pp. 586-609.

[16] H. Rastegari, A. Kermanpur, and A. Najafizadeh, 2015, "Investigating the Effects of Short Time Austenitizing and Cooling Rate on Pearlitic Microstructure and Mechanical Properties of a Hot Rolled Plain Eutectoid Carbon Steel," Materials and Design, 67, pp. 217-223.

[17] Q.X. Feng, L.F. Li, and W.Y. Yang, 2014, "Microstructures and Mechanical Properties of Hot-Rolled Nb-Microalloyed TRIP Steels by Different Thermo-Mechanical Processes," Materials Sciences and Engineering A, 605, pp. 14-21.

[18] S. Chen, Y.G. An, and C. Lahaije, 2015, "Toughness Improvement in Hot Rolled HSLA Steel Plates through Asymmetric Rolling," Materials Sciences and Engineering A, 625, pp. 374-379.

[19] Y.W. Kim, S.W. Song, and S.J. Seo, 2013, "Development of Ti and Mo Micro-Alloyed Hot-Rolled High Strength Sheet Steel by Controlling Thermomechanical Controlled Processing Schedule," Materials Sciences and Engineering A, 565, pp. 430-438.

[20] ArcelorMittal Dofasco Inc, http://www.dofasco.arcelormittal.com/ [Web resource].

[21] Private Communication, 2015, "Private Communication with the Research Group at University of Waterloo".

[22] S. Krajewski, and J. Nowacki, 2014, "Dual-Phase Steels Microstructure and Properties Consideration Based on Artificial Intelligence Techniques," Archives of Civil and Mechanical Engineering, 14, pp. 278-286.

[23] D. Holstein, C. Theiler, H.J. Hartmann, and W. Juptner, 1999, "Application of Digital Speckle Photography for Local Strain Analysis," The International Society for Optical Engineering, SPIE, 3824**,** pp. 229-236.

[24] F. Ackermann, 1984, "Digital Image Correlation: Performance and Potential Application in Photogrammetry," Photogrammetric Record, 11 (64) pp. 429-439.

[25] M. Grediac, 2004, "The use of Full-Field Measurement Methods in Composite Material Characterization: Interest and Limitations," Composites: Part A, 35, pp. 751-761.

[26] D. Lecompte, A. Smits, and S. Bossuyt, 2006, "Quality Assessment of Speckle Patterns for Digital Image Correlation," Optics and Lasers in Engineering, 44, pp. 1132-1145.

[27] R. Cintron, 2008, "Strain Measurements with the Digital Image Correlation System Vic-2D," University of Colorado, Boulder.

[28] C. Eberl, R. Thompson, D. Gianola, 2007, "Digital Image Correlation Tracking with MATLAB," Johns Hopkins University, Baltimore, Marland.

[29] The Mathworks Inc., 2013, "MATLAB," 2013a.

[30] J.H. Hollomon, 1945, "Tensile Deformation," Transactions of the American Institute of Mining, Metallurgical and Petroleum Engineers, 162, pp. 268-290.

[31] ABAQUS 6.13, 2013, "ABAQUS User's Manual," 6.13.

[32] C.S. Oh, N.H. Kim, and Y.J. Kim, 2011, "A Finite Element Ductile Failure Simulation Method using Stress-Modified Fracture Strain Model," Engineering Fracture Mechanics, 78, pp. 124-137.

[33] U. Borah, D. Samantaray, and S.K. Albert, 2013, "Thermo-Mechanical Axial-Torsion Testing to Assess Workability-Modeling using Finite Element Method and Experimental Validation," International Journal of Metallurgical Engineering, 2 (2), pp. 214-220.

[34] G. Mirone, 2007, "Role of Stress Triaxiality in Elastoplastic Characterization and Ductile Fracture Failure Prediction," Engineering Fracture Mechanics, 74 (8), pp. 1203-1221.

[35] M.S. Mirza, D.C. Barton, P. Church, 1996, "The Effect of Stress Triaxiality and Strain-Rate on the Fracture Characteristics of Ductile Metals," Journal of Materials Science, 31, pp. 453-461.

[36] Y. Zhang, and Z.T. Chen, 2007, "On the Effect of Stress Triaxiality on Void Coalescence," International Journal of Fracture, 143 (1), pp. 105-112.

[37] G.P. Tandon, G. J. Weng, 1988, "A Theory of Particle-Reinforced Plasticity," Journal of Applied Mechanics, 55 (1), pp. 126-135.

[38] H.P. Ganser, F.D. Fisher, and E.A. Werner, 1998, "Large Strain Behavior of Two-Phase Materials with Random Inclusions," Computational Materials Science, 11, pp. 221-226.

[39] The Engineering Toolbox. http://www.engineeringtoolbox.com/ [Web resource].

[40] T. Mori, K. Tanaka, 1973, "Average Stress in Matrix and Average Elastic Energy of Materials with Misfitting Inclusions," Acta Metallurgica Et Materialia, 21 (5), pp. 571-574.

[41] J.S. Griffin, 2012, "A Numerical and Experimental Investigation of Void Coalescence Causing Ductile Fracture," Master's Thesis, University of New Brunswick, Fredericton.

[42] V. Tvergaard, 1990, "Analysis of Tensile Properties for a Whisker-Reinforced Metal-Matrix Composite," Acta Materialia, 38 (2), pp. 185-194.

[43] Y. Zhang, 2008, "On Void Coalescence in Ductile Fracture of Aluminum Sheet," Master's Thesis, University of New Brunswick, Fredericton.

[44] G.R. Johnson, and W.H. Cook, 1985, "Fracture Characteristics of Three Metals Subjected to Various Strains, Strain Rates, Temperatures and Pressures," Engineering Fracture Mechanics, 21 (1), pp. 31-48.

[45] H.J.K. Lemmen, R.C. Alderliesten, R. Benedictus, J.C.J. Hofstede, and R. Rodi, 2008, "The Power of Digital Image Correlation for Detailed Elastic-plastic Strain Measurements," WSEAS International Conference on Engineering Mechanics, Structures, Engineering Geology (EMESEG), Greece.

[46] C.L. Hom, and R.M. McMeeking, 1991, "Plastic Flow in Ductile Materials Containing a Cubic Array of Rigid Spheres," International Journal of Plasticity, 7 (4), pp. 255-274.

[47] H.J. Bohm, and W. Han, 2001, "Comparisons between Three-Dimensional and Two-Dimensional Multi-Particle Unit Cell Models for Particle Reinforced Metal Matrix Composites," Modelling and Simulation in Materials Science and Engineering, 9, pp. 47-65.

[48] H.J. Bohm, A. Eckschlager, and W. Han, 2002, "Multi-Inclusion Unit Cell Models for Metal Matrix Composites with Randomly Oriented Discontinuous Reinforcements," Computational Materials Science, 25, pp. 42-53.

[49] T. Iung, and M. Grange, 1995, "Mechanical Behavior of Two-Phase Materials Investigated by the Finite Element Method: Necessity of Three-Dimensional Modeling," Materials Sciences and Engineering A, 201, pp. 8-11.

[50] J. Llorca, and J. Segurado, 2004, "Three-Dimensional Multiparticle Cell Simulations of Deformation and Damage in Sphere-Reinforced Composites," Materials Sciences and Engineering A, 365, pp. 267-274.

[51] J. Segurado, J. Llorca, and C. Gonzalez, 2002, "On the Accuracy of Mean-Field Approached to Simulate the Plastic Deformation of Composites," Scripta Materialia, 46, pp. 525-529.

[52] J. Segurado, C. Gonzalez, and J. Llorca, 2003, "A Numerical Investigation of the Effect of Particle Clustering on the Mechanical Properties of Composites," Acta Materialia, 51, pp. 2355-2369.

[53] J.P. Bandstra, and D.A. Koss, 2008, "On the Influence of Void Clusters on Void Growth and Coalescence during Ductile Fracture," Acta Materialia, 56, pp. 4429-4439.

[54] J. Segurado, and J. Llorca, 2002, "A Numerical Approximation to the Elastic Properties of Sphere-Reinforced Composites," Journal of the Mechanics and Physics of Solids, 50, pp. 2107-2121.

[55] J.W. Hancock, and D.K. Brown, 1983, "On the Role of Strain and Stress State in Ductile Failure," Journal of the Mechanics and Physics of Solids, 31, pp. 1-24.

[56] J. Llorca, and C. Gonzalez, 1998, "Microstructural Factors Controlling the Strength and Ductility of Particle-Reinforced Metal-Matrix Composites," Journal of the Mechanics and Physics of Solids, 46, pp. 1-28.

[57] Y. Hua, and L.X. Gu, 2013, "Prediction of the Thermomechanical Behavior of Particle-Reinforced Metal Matrix Composites," Composites: Part B, 45, pp. 1464-1470.

[58] Y.S. Suh, S.P. Josh, and K.T. Ramesh, 2009, "An Enhanced Continuum Model for Size-Dependent Strengthening and Failure of Particle-Reinforced Composites," Acta Materialia, 57, pp. 5848-5861.

[59] A.A. Gusev, P.J. Hine, and I.M. Ward, 2000, "Fiber Packing and Elastic Properties of a Transversely Random Unidirectional Glass/Epoxy Composite," Composites Science and Technology, 60, pp. 535-541.

[60] E.S. Loscar, N. Guisoni, and E.V. Albano, 2012, "Study of Random Sequential Adsorption by Means of the Gradient Method," The European Physical Journal B, 85: 60.

[61] M.D. Rintoul, and S. Torquato, 1997, "Reconstruction of the Structure of Dispersions," Journal of Colloid and Interface Science, 186, pp. 467-476.

[62] P. Viot, G. Tarjus, S. M. Ricci, 1992, "Random Sequential Adsorption of Anisotropic Particles. I. Jamming Limit and Asymptotic Behavior," The Journal of Chemical Physics, 97 (7), pp. 5212-5218.

[63] V. Privman, 2000, "Dynamics of Nonequilibrium Deposition," Colloids and Surfaces A: Physicochemical and Engineering Aspects, 165, pp. 231-240.

[64] C. Gonzalez, J. Segurado, and J. Llorca, 2004, "Numerical Simulation of Elasto-Plastic Deformation of Composites: Evolution of Stress Microfields and Implications for Homogenization Models," Journal of Mechanics and Physics of Solids, 52, pp. 1573-1593.

[65] N. Chawla, and K.K. Chawla, 2006, "Microstructure-Based Modeling of the Deformation Behavior of Particle Reinforced Metal Matrix Composites," Journal of Material Science, 41, pp. 913-925..

[66] P. Ludwik, 1909, "Element Der Technolnischen Mechanick," Springer, Berlin, German, Chap. 32.

[67] L.H. Dai, Z. Ling, and Y.L. Bai, 2001, "Size-Dependent Inelastic Behavior of Particle-Reinforced Metal-Matrix Composites," Composites Science and Technology, 61, pp. 1057-1063.

[68] H. Shen, and C.J. Lissenden, 2005, "Stress and Strain Localization Three-Dimensional Modeling for Particle-Reinforced Metal Matrix Composites," Metallurgical and Materials Transactions A, 36, pp. 1653-1660.

[69] J.W. Hutchinson, 1976, "Bounds and Self-consistent Estimates for Creep of Polycrystalline Materials," The Royal Society of London Proceeding A, 348**,** pp. 101-127.

[70] L. Babout, Y. Brechet, and E. Maire, 2004, "On the Competition between Particle Fracture and Particle Decohesion in Metal Matrix Composites," Acta Materialia, 52, pp. 4517-4525.

[71] L.H. Dai, Z. Ling, and Y.L. Bai, 2001, "Size-Dependent Inelastic Behavior of Particle-Reinforced Metal-Matrix Composites," Composites Science and Technology, 61, pp. 1057-1063.

[72] J. Rodriguez, M.A. Garrido-Maneiro, P. Poza, 2006, "Determinatioon of Mechaincal Properties of Aluminum Matrix Composites Constituents," Materials Sciences and Engineering A, 437, pp. 406-412.

[73] K. Niu, A. Abedini, and Z.T. Chen, 2014, "The Influence of Multiple Inclusion on the Cauchy Stress of a Spherical Particle-reinforced Composite Under Uniaxial Loading," ASME 2014 International Mechanical Engineering Congress & Exposition (IMECE), Montreal, Canada.

[74] A. Abedini, and Z.T. Chen, 2014, "A Micromechanical Model of Particle-Reinforced Metal Matrix Composites Considering Particle Size and Damage," Computational Materials Science, 85, pp. 200-205.

[75] A. Abedini, C. Butcher, and Z.T. Chen, 2013, "Numerical Simulation of the Influence of Particle Clustering on Tensile Behavior of Particle-Reinforced Composites," Computational Materials Science, 73, pp. 15-23.

[76] I. Doghri, A. Ouaar, 2003, "Homogenization of Two-Phase Elasto-Plastic Composite Material and Structures Study of Tangent Operators, Cyclic Plasticity and Numerical Algorithms," International Journal of Solids and Structures, 40 (7), pp. 1681-1712.

[77] C. Huet, 1990, "Application of Variational Concepts to Size Effects in Elastic Heterogeneous Bodies," Journal of the Mechanics and Physics of Solids, 8, pp. 813-841.

[78] R. Hill, 1965, "A Self-Consistent Mechanics of Composite Materials," Journal of the Mechanics and Physics of Solids, 13 (4), pp. 213-222.

[79] H.S. Kim, S.I. Hong, S.J. Kim, 2001, "On the Rule of Mixtures for Predicting the Mechanical Properties of Composite with Homogeneously Distributed Soft and Hard Particles," Journal of the Materials Processing Technology, 112, pp. 109-113.

[80] H.C. Chen, G.H. Cheng, 1989, "Effect of Martensite Strength on the Tensile Strength of Dual Phase Steels," Journal of the Materials Science, 24, pp. 1991-1994.

Appendix A – Random Sequential Adsorption Algorithm (RSA)

```
%%%%%%%%%%%%%%%%%%%%%%%%%%%%%%%%%%%%%%%%%%%%%%%%%%%%%%%%%%%%%%%%%%%%%%%%%%%%
%Programmer: Ke Niu
%Date: April 10, 2015
%Code description: Generate coordinates (XYZ)of n particles randomly
%and sequentially by using Standard Random Sequential Adsorption
%algorithm (RSA)
%The number of particles are random
%%%%%%%%%%%%%%%%%%%%%%%%%%%%%%%%%%%%%%%%%%%%%%%%%%%%%%%%%%%%%%%%%%%%%%%%%%%%
clc
clear all
close all
%%%%%%%%%%%%%%%%%%%%%%%%%%%%%%%%%%%%%%%%%%%%%%%%%%%%%%%%%%%%%%%%%%%%%%%%%%%%

%Volume fraction of particles
vfraction = 0.2;
%Number of particles
n = round(20 + 20*rand(1));
%Creat a zero n by 4 matrix
A = zeros(n,4);
%The radius of the sphere
r = (vfraction*8/n*3/4/pi)^(1/3);
%Creat a zero 1 by 27 matrix
M = zeros(1,27);
o1 = zeros(1,3);
o2 = zeros(1,3);
%S1 is the minimum particle separation, and it was set to 2.07 times the
%radius of the sphere
S1 = 2.07*r;
%S2 is the minimum distance between the surface of
%particles and the unit cell faces
S2 = 0.1*r;

%Use loop to generate random numbers between 0 and 2 until we get 15 groups
%of numbers
for i=1:n
    while 1
        %Restart the generator every loop
        rng('shuffle')
        %Generate a 1 by 3 vector which contains numbers between 0 and 2
        %randomly
        B = 2*rand(1,3);

        %The first group of coordinates will be checked, if this particle
        %is not too close to the unit cell faces, it will be stored
        %The length of cubic unit cell is 2
        if i == 1
            x1 = abs(B(1,1)-r);
            x2 = abs(B(1,2)-r);
            x3 = abs(B(1,3)-r);

            x4 = abs(B(1,1)+r-2);
            x5 = abs(B(1,2)+r-2);
```

```
            x6 = abs(B(1,3)+r-2);

            y1 = [x1,x2,x3];
            y2 = [x4,x5,x6];
            z1 = min(y1);
            z2 = min(y2);
            if z1 >= S2 && z2 >= S2
                A(1,1) = 1;
                A(1,2) = B(1,1);
                A(1,3) = B(1,2);
                A(1,4) = B(1,3);
            break;
            end
        else
            %The following groups of coordinates will be constrained
            %Use for loop to calculate
            %Initialize s
            s = 1;

            %Use for loop to check the distance between the current
            %particle(i) and all the particles previously accepted(j=i-1)
            for j = 1:(i-1)
                %First condition S1
                %h,k,l can take 0, 2, -2, so there are 27 conditions for
                %each pair of particles
                for H = 1:3
                    h = -2 + (H-1)*2;
                    for K = 1:3
                        k = -2 + (K-1)*2;
                        for L = 1:3
                            l = -2 + (L-1)*2;
                            %Calculate the distance between the centers of
each pair of spheres
                            %In D, we need to use j to stand for previous
                            %particles
                            D = sqrt((B(1,1)-A(j,2)+h)^2+(B(1,2)-
A(j,3)+k)^2+(B(1,3)-A(j,4)+l)^2);
                            %q is the formula to calculate the sequence of 27
data
                            %store the 27 values of D
                            q = 9*(H-1)+3*(K-1)+L;
                            M(q) = D;
                        end
                    end
                end
                %Find out the minimum value of M
                m = min(M);
                % If the first condition was not satisfied, s = 0
                if m < S1
                    s = s*0;
                    break;
                end
                %Second condition S2
                %The surface of particle should not be very close to the
                %unit cell faces
                b1 = abs(B(1,1)-r);
```

```
                b2 = abs(B(1,2)-r);
                b3 = abs(B(1,3)-r);

                b4 = abs(B(1,1)+r-2);
                b5 = abs(B(1,2)+r-2);
                b6 = abs(B(1,3)+r-2);

                o1 = [b1,b2,b3];
                o2 = [b4,b5,b6];
                %Find out the minimum value
                c1 = min(o1);
                c2 = min(o2);

                %If the second condition was not satisfied, s = 0
                if c1 < S2 || c2 < S2
                    s = s*0;
                    break;
                end
            end

            %If both of these two conditions were satisfied, s = 1
            %This coordinate is accepted and stroed in A, otherwise start a
            %new loop
            if  s == 1
               %Store values of B in A
                A(i,1) = i;
                %The second column is the X-coordinate
                A(i,2) = B(1,1);
                %The third column is the Y-coordinate
                A(i,3) = B(1,2);
               %The last column is the Z-coordinate
                A(i,4) = B(1,3);
                break;
            end
        end
    end
end
%Display the selective coordinates
disp('The groups of Coordinates are:');
disp(A);

original = zeros(n,3);
for i = 1:n
    original(i,1) = A(i,2);
    original(i,2) = A(i,3);
    original(i,3) = A(i,4);
end

%Periodicity
%Calculate the coordinates for particles which are added to maintain
%periodicity
for i = 1:n
    if A(i,2) > 2 - r
        AA(i,2) = A(i,2) - 2;
        if A(i,3) > 2 - r
```

```
            AA(i,3) = A(i,3) - 2;
            if A(i,4) > 2 - r
                AA(i,4) = A(i,4) - 2;
            elseif A(i,4) < r
                AA(i,4) = A(i,4) + 2;
            else
                AA(i,4) = A(i,4);
            end
        elseif A(i,3) < r
            AA(i,3) = A(i,3) + 2;
            if A(i,4) > 2 - r
                AA(i,4) = A(i,4) - 2;
            elseif A(i,4) < r
                AA(i,4) = A(i,4) + 2;
            else
                AA(i,4) = A(i,4);
            end
        else
            AA(i,3) = A(i,3);
            if A(i,4) > 2 - r
                AA(i,4) = A(i,4) - 2;
            elseif A(i,4) < r
                AA(i,4) = A(i,4) + 2;
            else
                AA(i,4) = A(i,4);
            end
        end
    elseif A(i,2) < r
        AA(i,2) = A(i,2) + 2;
        if A(i,3) > 2 - r
            AA(i,3) = A(i,3) - 2;
            if A(i,4) > 2 - r
                AA(i,4) = A(i,4) - 2;
            elseif A(i,4) < r
                AA(i,4) = A(i,4) + 2;
            else
                AA(i,4) = A(i,4);
            end
        elseif A(i,3) < r
            AA(i,3) = A(i,3) + 2;
            if A(i,4) > 2 - r
                AA(i,4) = A(i,4) - 2;
            elseif A(i,4) < r
                AA(i,4) = A(i,4) + 2;
            else
                AA(i,4) = A(i,4);
            end
        else
            AA(i,3) = A(i,3);
            if A(i,4) > 2 - r
                AA(i,4) = A(i,4) - 2;
            elseif A(i,4) < r
                AA(i,4) = A(i,4) + 2;
            else
                AA(i,4) = A(i,4);
            end
```

```
        end
    else
        if A(i,3) > 2 - r
            AA(i,2) = A(i,2);
            AA(i,3) = A(i,3) - 2;
            if A(i,4) > 2 - r
                AA(i,4) = A(i,4) - 2;
            elseif A(i,4) < r
                AA(i,4) = A(i,4) + 2;
            else
                AA(i,4) = A(i,4);
            end
        elseif A(i,3) < r
            AA(i,2) = A(i,2);
            AA(i,3) = A(i,3) + 2;
            if A(i,4) > 2 - r
                AA(i,4) = A(i,4) - 2;
            elseif A(i,4) < r
                AA(i,4) = A(i,4) + 2;
            else
                AA(i,4) = A(i,4);
            end
        else
            if A(i,4) > 2 - r
                AA(i,2) = A(i,2);
                AA(i,3) = A(i,3);
                AA(i,4) = A(i,4) - 2;
            elseif A(i,4) < r
                AA(i,2) = A(i,2);
                AA(i,3) = A(i,3);
                AA(i,4) = A(i,4) + 2;
            else
            end
        end
    end
    AA(i,1) = i;
end

Intersectp = zeros(n,3);
for i = 1:n
    for j = 1:3
        Intersectp(i,j) = AA(i,j+1);
    end
end

%Remove zero rows
Intersectp(all(~Intersectp,2),:)=[];

%Find the number of groups of coordinates of intersected particles
count = size(Intersectp,1);
nu = 1;
for num = 1:count
        if Intersectp(num,1) < 0
            xx1 = Intersectp(num,1) + 2;
            xx2 = Intersectp(num,1);
            if Intersectp(num,2) < 0
```

```
        yy1 = Intersectp(num,2) + 2;
        yy2 = Intersectp(num,2);
        if Intersectp(num,3) < 0
            zz1 = Intersectp(num,3) + 2;
            zz2 = Intersectp(num,3);
        elseif Intersectp(num,3) > 2
            zz2 = Intersectp(num,3);
            zz1 = Intersectp(num,3) - 2;
        else
            zz1 = Intersectp(num,3);
            zz2 = zz1;
        end
    elseif Intersectp(num,2) > 2
        yy1 = Intersectp(num,2) - 2;
        yy2 = Intersectp(num,2);
            if Intersectp(num,3) < 0
                zz1 = Intersectp(num,3) + 2;
                zz2 = Intersectp(num,3);
            elseif Intersectp(num,3) > 2
                zz2 = Intersectp(num,3);
                zz1 = Intersectp(num,3) - 2;
            else
                zz1 = Intersectp(num,3);
                zz2 = zz1;
            end
    else
        yy1 = Intersectp(num,2);
        yy2 = yy1;
        if Intersectp(num,3) < 0
            zz1 = Intersectp(num,3) + 2;
            zz2 = Intersectp(num,3);
        elseif Intersectp(num,3) > 2
            zz2 = Intersectp(num,3);
            zz1 = Intersectp(num,3) - 2;
        else
            zz1 = Intersectp(num,3);
            zz2 = zz1;
        end
    end
elseif Intersectp(num,1) > 2
    xx1 = Intersectp(num,1) - 2;
    xx2 = Intersectp(num,1);
    if Intersectp(num,2) < 0
        yy1 = Intersectp(num,2) + 2;
        yy2 = Intersectp(num,2);
        if Intersectp(num,3) < 0
            zz1 = Intersectp(num,3) + 2;
            zz2 = Intersectp(num,3);
        elseif Intersectp(num,3) > 2
            zz2 = Intersectp(num,3);
            zz1 = Intersectp(num,3) - 2;
        else
            zz1 = Intersectp(num,3);
            zz2 = zz1;
        end
    elseif AA(num,2) > 2
```

```
            yy1 = AA(num,2) - 2;
            yy2 = AA(num,2);
            if Intersectp(num,3) < 0
                zz1 = Intersectp(num,3) + 2;
                zz2 = Intersectp(num,3);
            elseif Intersectp(num,3) > 2
                zz2 = Intersectp(num,3);
                zz1 = Intersectp(num,3) - 2;
            else
                zz1 = Intersectp(num,3);
                zz2 = zz1;
            end
        else
            yy1 = Intersectp(num,2);
            yy2 = yy1;
            if Intersectp(num,3) < 0
                zz1 = Intersectp(num,3) + 2;
                zz2 = Intersectp(num,3);
            elseif Intersectp(num,3) > 2
                zz2 = Intersectp(num,3);
                zz1 = Intersectp(num,3) - 2;
            else
                zz1 = Intersectp(num,3);
                zz2 = zz1;
            end
        end
    else
        xx1 = Intersectp(num,1);
        xx2 = xx1;
        if Intersectp(num,2) < 0
            yy1 = Intersectp(num,2) + 2;
            yy2 = Intersectp(num,2);
            if Intersectp(num,3) < 0
                zz1 = Intersectp(num,3) + 2;
                zz2 = Intersectp(num,3);
            elseif Intersectp(num,3) > 2
                zz2 = Intersectp(num,3);
                zz1 = Intersectp(num,3) - 2;
            else
                zz1 = Intersectp(num,3);
                zz2 = zz1;
            end
        elseif Intersectp(num,2) > 2
            yy1 = Intersectp(num,2) - 2;
            yy2 = Intersectp(num,2);
            if Intersectp(num,3) < 0
                zz1 = Intersectp(num,3) + 2;
                zz2 = Intersectp(num,3);
            elseif Intersectp(num,3) > 2
                zz2 = Intersectp(num,3);
                zz1 = Intersectp(num,3) - 2;
            else
                zz1 = Intersectp(num,3);
                zz2 = zz1;
            end
        else
```

```
                yy1 = Intersectp(num,2);
                yy2 = yy1;
                if Intersectp(num,3) < 0
                    zz1 = Intersectp(num,3) + 2;
                    zz2 = Intersectp(num,3);
                elseif Intersectp(num,3) > 2
                    zz2 = Intersectp(num,3);
                    zz1 = Intersectp(num,3) - 2;
                else
                    zz1 = Intersectp(num,3);
                    zz2 = zz1;
                end
            end
        end

        %All combinations of coordinates of intersected particles
        x = [xx1,xx2];
        y = [yy1,yy2];
        z = [zz1,zz2];
        for t = 1:2
            for d= 1:2
                for f = 1:2
                    matrix(nu,2) = x(t);
                    matrix(nu,3) = y(d);
                    matrix(nu,4) = z(f);
                    matrixsize = size(matrix,1);
                    matrix(nu,1) = nu;
                    nu = nu + 1;
                end
            end
        end
end

countmatrix = size(matrix,1);
p = zeros(countmatrix,3);
for p = 1:countmatrix
    particle(p,1) = matrix(p,2);
    particle(p,2) = matrix(p,3);
    particle(p,3) = matrix(p,4);
end
%Remove repeated rows
particle = unique(particle,'rows');
%Display the
disp('The coordinates of additional particles');
disp(particle);
%Combine orignal coordinates of particles and additional particles
Coordinates = combine(original,particle);
coordinatesize = size(Coordinates,1);
%Display the total number of particles
disp('The total number of partilces are');
disp(coordinatesize);
%Display all combinations of coordinates of intersected particles
disp('All groups of coordinates of particles are');
disp(Coordinates);
```

Appendix B – Experimental Apparatus

Band Saw

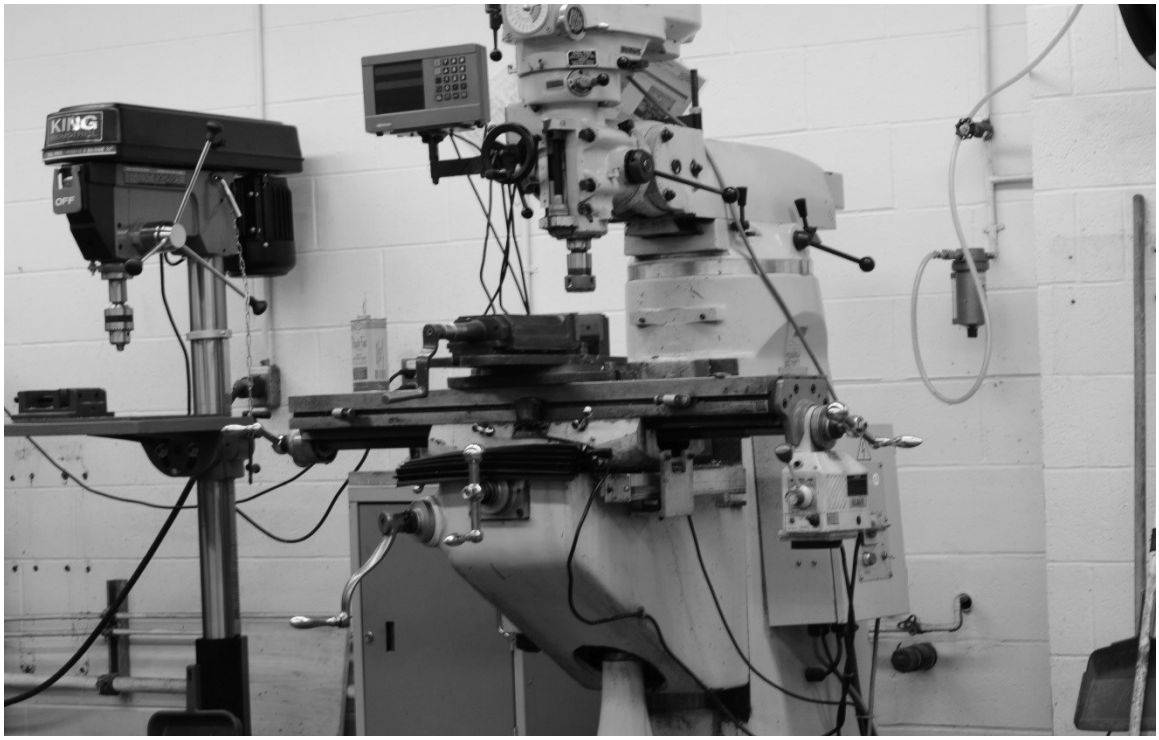

Milling Machine

Precision Cutting Machine

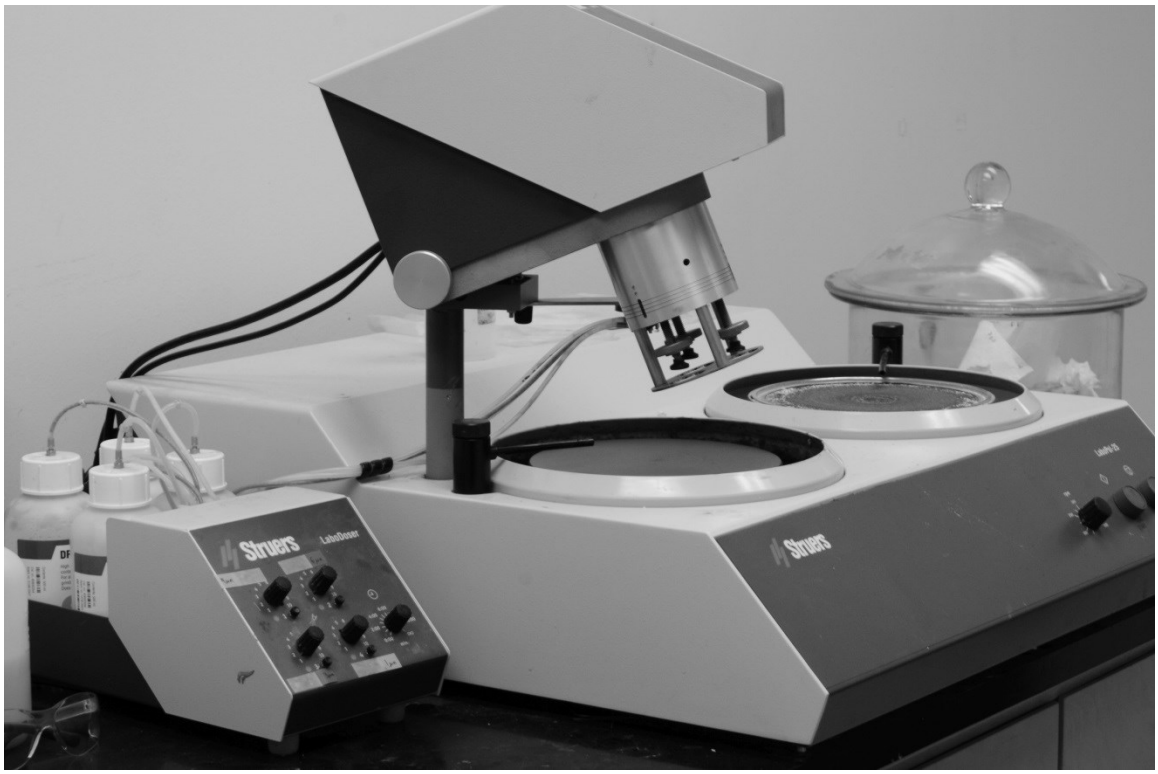

Sample Polisher